Giant Magnetocaloric effect and Magnetic Properties of selected Rare-Earth compounds

By

Student: Masevhe Hamisi Mbulunge

Supervisor: Prof Moise Bertin Tchoula Tchokonte

Department of Physics & Astronomy

Faculty of Natural Science

University of the Western Cape

Bellville, South Africa

February 2021

KEYWORDS

1. X-ray diffraction
2. Rare–earth compounds
3. Antiferromagnetism
4. Magnetic susceptibility
5. Magnetization
6. Heat capacity
7. Electrical resistivity
8. Magnetocaloric effect

NOMENCLATURE

AFM	Antiferromagnetism
BCC	Body–Centered Cubic
CAILS	Cell and Intensity Least Square
CEF	Crystalline electric field
DC	Direct current
EDS	Energy-dispersive X-ray spectroscopy
FC	Field–cooled
FCC	Face–Centered Cubic
FEGSEM	Field Emission Gun Scanning Electron Microscopy
FM	Ferromagnetism
HCP	Hexagonal Close–Packed
IUPAC	International Union of Pure and Applied Chemistry
LSQ	Least squares
MCE	Magnetocaloric Effect
MPMS	Magnetic Properties Measurement System
MR	Magnetic Refrigeration
QD PPMS	Quantum Design Physical Property Measurement System
RCP	Relative cooling power
RE	Rare-earth
RKKY	Ruderman – Kittel – Kasuya – Yosida
RRR	Room – Ratio – Resistivity
SQUID	Superconducting Quantum Interference Device
XRD	X-ray diffraction

LIST OF CONFERENCE PRESENTATIONS

1. 11th International Conference on Magnetic and Superconducting Materials (MSM 2019), August 17 – 24, 2019, Seoul National University, Seoul, Korea. Poster presentation: "*Giant magnetocaloric effect and low-temperature properties of $NdPd_2Al_2$ compound"*.
2. 63rd South African Institute of Physics (SAIP) Conference, June 25 – 29, 2018, University of Free State, Bloemfontein, Poster presentation: "*Magnetic properties and giant magnetocaloric effect of $NdPd_2Al_2$".*

PUBLICATIONS

1. *Magnetic and thermodynamic properties of the NdCuGa compound.* H. M. Masevhe, M. B. Tchoula Tchokonte, J. J. Mboukam, B. Sahu, A. M. Strydom and D. Kaczorowski. Submitted to Journal of Alloys and Compounds.
2. *Transport, magnetic and magnetocaloric properties of* $NdPd_2Al_2$ *compound.* H. M. Masevhe, M. B. Tchoula Tchokonte, J. J. Mboukam, B. Sahu, A. M. Strydom and D. Kaczorowski. Submitted to Journal of Physics and Chemistry of Solids.

ABSTRACT

Rare-earth (RE) compounds have been an attractive subject, based on the unique electronic structures of the rare-earth elements. In particular, the RETX (RE = rare-earth, T = 3d/4d/5d, transition metals, and X = p – block elements) series is a large family of intermetallic compounds which crystallizes in different crystal structure depending on the constituents. Most of these compounds crystalize in the hexagonal, orthorhombic, and tetragonal crystal structure. On the other hand, the family of compounds RET_2X_2 adopted the tetragonal crystal structure of the $ThCr_2Si_2$ or the $CaBe_2Be_2$ with different space groups. Owing to the different crystal structure, these compounds show versatile magnetic and electrical properties such as Kondo effect, complex magnetic behaviour, valence fluctuation, unconventional and conventional superconductivity, heavy fermion behaviour, Fermi and non – Fermi liquid behaviour, metamagnetism, spin – glass, memory effect, crystal electric field (CEF), magnetoresistance and magnetocaloric effect. The history of magnetism reveals that it is closely related to practical applications and magnetic materials from the most vital components in many applications. These are memory devices, permanent magnets, transformer cores, magneto-mechanical devices and magneto-electronic devices. Recent additions to this list include magnetic refrigeration through the studies of magnetocaloric effect as well as spintronics.

Magnetic refrigeration (MR) is an emerging technology and shows real potential to enter conventional markets and the principles of MR obeys the magnetocaloric effect (MCE), which is based on the effect caused by a magnetic field on the materials that accept the property of varying the magnetic entropy, as well as its temperature when varying the magnetic field. In this thesis, we report giant magnetocaloric effect and magnetic properties of $NdPd_2Al_2$ and RECuGa (RE = Nd, Dy, and Ho) compounds. These investigations were done through measurements of X – ray diffraction (XRD), magnetic susceptibility, ($\chi(T)$), magnetization, ($M(H)$), isothermal magnetization, ($M(H, T)$), heat capacity, ($C_p(T)$) and electrical resistivity, ($\rho(T)$). MCE has been studied from the isothermal magnetization and heat capacity measurements.

The first chapter of the thesis describes the theoretical background from which the experimental results have been analyzed and interpreted. This is followed by the chapter which presents experimental details and methodology carried out in this thesis.

Chapter three presents the results and discussion of the transport, magnetic and magnetocaloric properties of $NdPd_2Al_2$ compounds. XRD studies confirm the tetragonal $CaBe_2Ge_2$ – type structure with space group *P4/nmm* (No. 129). The results of $\rho(T)$, $\chi(T)$ and $C_p(T)$ indicate a putative antiferromagnetic (AFM) phase transition at low temperature at, T_N = 3 K. On the other hand, $\chi(T)$ data at high temperatures follow the Curie – Weiss relationship giving an effective magnetic moment close to that expected for the trivalent Nd^{3+} ion. The magnetization results indicate metamagnetic – like transition at a low field that bears a first-order character which corroborates with the Below – Arrott plots. Giant MCE was obtained for the $NdPd_2Al_2$ compound similar to those reported for potential magnetic refrigerant materials.

Chapter four discusses the magnetic and thermodynamic properties of the series of compounds RECuGa where RE = Nd, Dy, and Ho. XRD studies indicate the orthorhombic $CeCu_2$ – type crystal structure with space group *Imma* (No. 74) for all three compounds. Magnetic measurements indicate a putative AFM phase transition below T_N = 7.1, 8.5, and 3.7 K for Nd, Dy, and Ho compounds, respectively. The high-temperature $\chi(T)$ data for all three compounds follow the Curie – Weiss relationship giving an effective magnetic moment close to that expected for the trivalent rare-earth ion. Again, large MCE were obtained for all three compounds similar to those reported for materials that can be used as magnetic refrigerant materials.

MOTIVATION

Among the fields of sciences and technologies, sustainable development has become a large focus as climate changes and carbon emission become more pressing issues. As modern technologies improve, so does the need for sustainability, which is defined by the Environmental Protection Agency as creating and maintaining the conditions under which humans and the natural world can exist in productive harmony to support present and future generations [1]. Creating sustainable solutions is a challenge in modern sciences and technologies.

Ozone layer depletion continues despite measures to protect the ozonosphere in the atmosphere and the ecological environment. On the other hand, the traditional technology of steam compression refrigeration is close to reaching its technical boundaries in achieving further improvements in energy and energy efficiency, as well as its use of gases with ozone depletion and global warming protection [2]. As a result, scientists and engineers have begun in recent years to explore new technologies for cooling, such as thermoelectric cooling [3], thermoacoustic, absorption [4, 5], adsorption [6] and magnetic refrigeration.

The refrigeration system exploits a material's entropy change due to the variation of an external parameter as well as the pressure or magnetization to absorb and release energy. In refrigeration technologies based on magnetocaloric effect (MCE), the MCE can be defined as the absorption or emission of heat when a magnetocaloric material is subjected to a change of a magnetic field in a process where the pressure has no influence. Since the discovery of giant MCE at room temperature [7], the ways to improve the performance of magnetocaloric materials and new magnetic materials exhibiting large MCE have attracted increasing attention and magnetic refrigeration is becoming an active field of research in science. So far, several classes of first-order magnetostructural transformation (MST) systems [7 - 11], have been reported to exhibit giant MCE during the magnetic - field – induced MST. Given these, the search for new magnetic materials exhibiting giant MCE has been the motivation of this research project.

DECLARATION

This thesis is a presentation of my original research work. Wherever contributions of others are involved, every effort is made to indicate this clearly, with due reference to the literature, and acknowledgement of collaborative research and discussions.

The work was done under the guidance of Professor Moise Bertin Tchoula Tchokonte, at the Physics & Astronomy Department of the University of the Western Cape, Bellville, South Africa. It is being submitted for the degree of Master of Science, and it is the first time being submitted for this degree.

Masevhe Hamisi Mbulunge ……

Candidate's name Signature

ACKNOWLEDGEMENTS

Working on this Masters has been a delightful and often overwhelming experience. This journey has provided me with a real learning experience on the significance of multi-tasking whilst remaining focused. In any case, I'm grateful to many people for making the time working on my Masters a remarkable experience.

First and foremost, I give gratitude to the Lord Almighty for choosing me and granting me the opportunity, wisdom, and ability to accomplish this study despite the numerous constraints that I encountered.

I am sincerely appreciative to my supervisor Professor Moise Tchoula Tchokonte, for allowing me to embark on this Masters study in a wonderful group that has provided me with the perfect atmosphere while doing this work. I would like to appreciate Prof Moise for his inspirational knowledge and for being always willing to explain things that seem difficult to me in a simple and clear way. Your understanding of physics has inspired me. Regardless of any busy schedule you always found time, working with you has been a real pleasure.

To the founder and leader of the Strongly Correlated Electrons Systems laboratory of the Physics department of the University of Johannesburg, Prof. A.M. Strydom, I thank you for your patience, kindness and for allowing me into your laboratory to conduct my experiments. To Prof. D. Kaczorowski from the Institute of Low Temperature and Structure Research, Polish Academy of Sciences, Poland, thank you very much for the magnetic measurements done on my compounds on my behalf, thank you for your willingness at all times.

To my colleagues, Bashier and Jean, thank you for making time for me and your willingness to assist during my Masters studies. To Mercy Tukisho Banda thank you for your support, sacrifices, and encouragement. To close, I wish to reiterate my thanks to my family, my mom and dad, and my siblings, thank you very much for the continuous support you gave me through the time of my studies, thank you for not doubting me.

CONTENTS

LIST OF FIGURES

LIST OF TABLES

CHAPTER 1

THEORETICAL BACKGROUND

1.1. Introduction

In the modern science world, multidisciplinary research is a continually developing field. The combination of chemical and physical methods, so-called material science, is a new task for solid state chemists. To fulfill the needs for a variety of demands, new materials must be developed. Thus, not only structural determination but also electronic and magnetic properties of new materials should be investigated. This comes along with theoretical calculations and predictions for these compounds. Intermetallic compounds containing rare-earth elements are interesting because they exhibit a variety of ground state properties depending on the ratio exchange interactions to crystal field interaction.

In the present section, some general background information about the rare-earth (RE) elements and rare-earth intermetallic compounds with 3d transition metals are presented together with their physical properties.

1.2. Rare-earth elements and rare-earth intermetallic compounds with 3d transition metals

The term rare – earth (RE) has often been referred to the lanthanide elements in the periodic table, starting from lanthanum (^{57}La) to lutetium (^{71}Lu), together with scandium (^{21}Sc) and yttrium (^{39}Y) (see Figure 1.1)

The RE elements are divided into three groups, these are the light, the heavy, and the medium or middle RE elements [12]. The grouping of these categories is not consistent among different authors. The only acceptable argument or the grouping of the RE elements is given by Röhr [13], who distinguished two groups: the light RE elements, starting from cerium (Ce) to gadolinium (Gd) and the heavy RE elements starting from terbium (Tb) to lutetium (Lu) including yttrium (Y). The other reasonable argument is given in reference [14] and similar to that given by Röhr [13] with the exception that the element La is included in the light RE

elements. This grouping is based on the fact that the electron configuration is the basis for the distinction between the two groups.

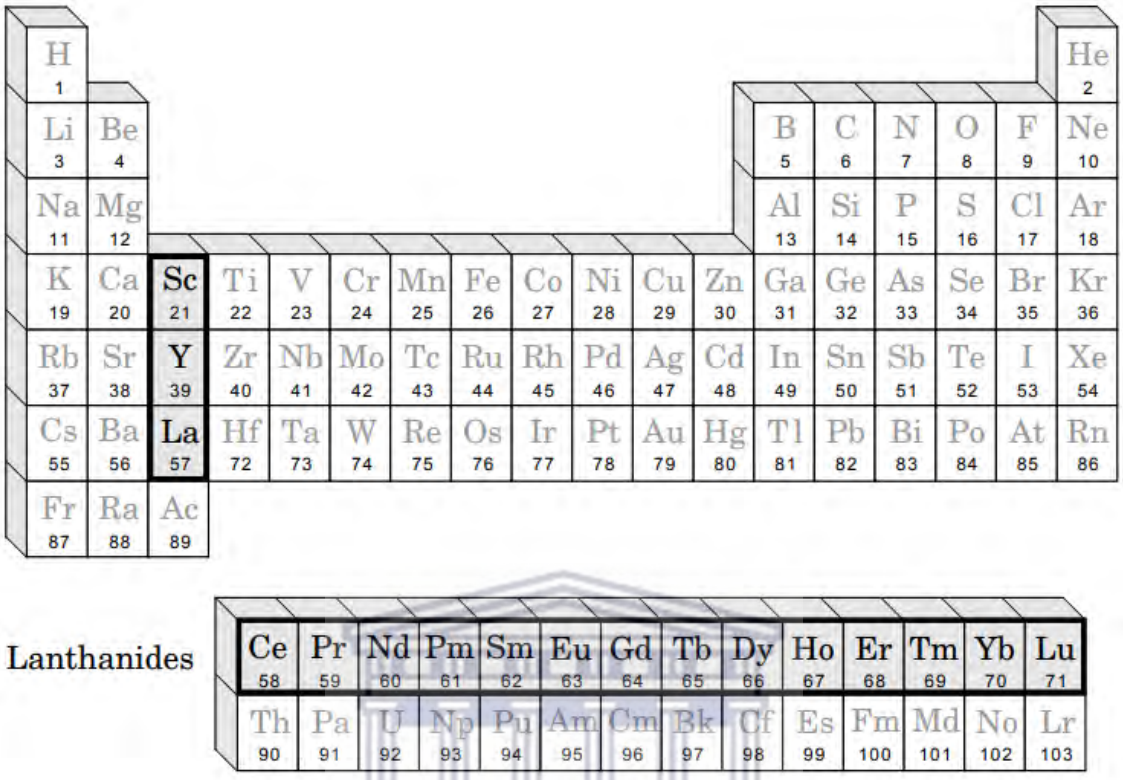

Figure 1.1: The periodic table of the elements, with RE elements highlighted [14].

It is reasonable to consider the lanthanides as a group separate from the rest of the periodic table of elements, only if the principal interest in these elements is those properties that depend on the occupancy of the 4f electron shell, from 0 (La) to 14 (Lu) [14]. The f - electron shell of the lanthanides is gradually filled when moving from La (f^0) with all f-instances unoccupied (no f-electron) through Gd (f^7) with half of the f-instances occupied to Lu (f^{14}) with all f-instances occupied (filled shell of 14 electrons). These more stable instances can act as borders for the groups such as the light RE elements (Ce – Gd) and heavy RE elements (Tb – Lu). The element La is not included in the group of light RE elements because it has no f – electron. The element Y is included in the group of heavy RE elements because the ionic radius of this element is nearly the same as that of dysprosium (Dy) or Holmium (Ho), and its chemical behaviour is similar to that of Ho [12].

The outer electron configuration determining the number and nature of the valence electrons is the same for the 15 elements (La – Lu). The same holds for their atomic or metallic radii which

differs mutually by only a few percent (excluding abnormal valance state) [15]. The chemical properties of the RE elements are fairly alike. As a consequence of that, firstly it presents enormous difficulties in separating these elements from each other since they are always found together in nature. Secondly, the chemical similarity leads to more or less uniform behaviour when RE elements are combined with other metals to form intermetallic compounds. In other words, one can say that if one member of the group forms an intermetallic compound of a given composition and crystal structure, all the other members will act in the same way. Opposing to the chemical properties the physical properties may vary remarkably within a series of isotropic compounds.

The class of compounds formed between RE and 3d transition metals is of particular interest in this study. There is a large number of these compounds. For instance, the combination of RE elements and one 3d element produces more than ten different intermetallic compounds. The exciting thing in these resulting compounds is that simultaneously one can benefit here from the intrinsic properties of both elements, that is, from the high magnetic moment per atom and the strong single – ion magnetocrystalline anisotropy of the RE partner and from the high magnetic coupling strength of the moment of the 3d transition metal partner [15].

In recent years, the investigation of intermetallic compounds between RE and transition metals have received additional impetus from the discovery that several of its members can be used as starting materials for permanent magnets of outstanding quality [15]. In general, the application of the RE element cover a huge field as all 17 elements have to be considered. Despite their chemical characteristic, they have diverging applications in various areas such as; energy efficiency, environmental protection, digital technology, medical applications, and others such as water treatment, magnetic refrigeration and superconductivity, etc.

1.2.1. Electronic Configurations

In general, the electronic configuration of an atom in the ground state is determined by its principal quantum number, n and angular momentum, l. According to the principle of lowest energy, there are two types of electronic configurations for the lanthanide elements: $[Xe]4f^{n}6s^{2}$ and $[Xe]4f^{n-1}5d^{1}6s^{2}$. Here [Xe] represents the electronic configuration of xenon which is $1s^{2}2s^{2}2p^{6}3s^{2}3p^{6}3d^{10}4s^{2}4p^{6}4d^{10}5s^{2}5p^{6}$, where n represents a number from 1 to 14. La, Ce, and Gd adopt the configuration $[Xe]4f^{n}6s^{2}$ type, while Pr, Nd, Pm, Sm, Eu, Tb, Dy, Ho, Er, Tm, Y,

and Lu adopt the configuration $[Xe]4f^{n-1}5d^16s^2$ type. Sc and Y do not have 4f electrons but do have similar chemical properties to lanthanide elements because their outermost electrons have the $(n-1)d^1ns^2$ configuration. For this reason, they are generally regarded as being lanthanide elements [16]. As an introduction to the properties of the RE metals, Table 1.1 lists their electronic configurations, crystal structures, and lattice constants.

As the electronic configurations of the elements in the RE series have a significant influence on their crystal structures, and hence their surface structures, it is important to consider the systematics of the filling of the outer electron subshells in the lanthanides. The outer electron configurations of the RE elements, Pr – Sm and Tb – Tm are different for the atomic and solid state – the divalent $4f^{n+1}\,6s^2$ atomic configurations become trivalent $4f^n\,(5d\,6s)^3$ in the solid state, where $n = 2 – 5$ and $8 – 12$, respectively [14]. Ce is a special case, as a precise value for the 4f occupancy and the resultant valency cannot be determined uniquely. For the other RE elements, the atomic valency is unchanged upon forming a solid.

The common electronic configuration used for the lanthanide elements that illustrate some physical properties of these elements can be described in terms of core shells equivalent to a Pd atom plus the following configuration: $4f^n5s^25p^65d^16d^2$. The complete electronic configuration is then given in the form:

$$[Pd]^{46}4f^n5s^25p^65d^16d^2 \quad (n = 0 – 14). \tag{1.1}$$

Thus, the 4f electrons are well shielded by the full $5s^25p^6$ shell. This is particularly the case for the so–called heavy RE from Gd through Tm. The well-screened 4f band plays an important role in some physical properties such as magnetism and specific heat [17]. The wave function of the 4f shell is a small radial extend giving a localized character to the 4f electron. As a result of that, a minimum direct exchange interaction between the RE magnetic moment in a solid is observed. On the other hand, the outer electrons shells, $5d^16s^2$, known as valence electrons, form the conduction band in the solid. Thus, the RE ions are trivalent. Some elements like Ce, Eu, and Yb present an exception in solid state.

Table 1.1: Structural and electronic properties of RE elements

Element		Z	A	Electron Config	Radius / pm Ionic	Metallic	Crystal Structure	Lattice Parameters a / pm	c / pm	c/a
Scandium	Sc	21	45	$(3d4s)^3$	78.5	164.1	hcp	330.9	526.8	1.592
Yttrium	Y	39	89	$(4d5s)^3$	88.0	180.1	hcp	364.8	573.2	1.571
Lanthanum	La	57	139	$4f^0\ (5d6s)^3$	106.1	187.9	dhcp	377.4	1217.1	3.225
Cerium	Ce	58	140	$4f^1\ (5d6s)^3$	103.4	182.5	fcc	516.1	—	—
Praseodymium	Pr	59	141	$4f^2\ (5d6s)^3$	101.3	182.8	dhcp	367.2	1183.3	3.222
Neodymium	Nd	60	144	$4f^3\ (5d6s)^3$	99.5	182.1	dhcp	365.8	1179.7	3.225
Promethium	Pm	61	145	$4f^4\ (5d6s)^3$	97.9	181.1	dhcp	365	1165	3.19
Samarium	Sm	62	150	$4f^5\ (5d6s)^3$	96.4	180.4	rhom	362.9	2620.7	7.222
Europium	Eu	63	152	$4f^7\ (5d6s)^2$	95.0	204.2	bcc	458.3	—	—
Gadolinium	Gd	64	157	$4f^7\ (5d6s)^3$	93.8	180.1	hcp	363.4	578.1	1.591
Terbium	Tb	65	159	$4f^8\ (5d6s)^3$	92.3	178.3	hcp	360.6	569.7	1.580
Dysprosium	Dy	66	163	$4f^9\ (5d6s)^3$	80.8	177.4	hcp	359.2	565.0	1.573
Holmium	Ho	67	165	$4f^{10}(5d6s)^3$	89.4	176.6	hcp	357.8	561.8	1.570
Erbium	Er	68	167	$4f^{11}(5d6s)^3$	88.1	175.7	hcp	355.9	558.5	1.569
Thulium	Tm	69	169	$4f^{12}(5d6s)^3$	86.9	174.6	hcp	353.8	555.4	1.570
Ytterbium	Yb	70	173	$4f^{14}(5d6s)^2$	85.8	193.9	fcc	548.5	—	—
Lutetium	Lu	71	175	$4f^{14}(5d6s)^3$	84.8	173.5	hcp	350.5	554.9	1.583

For RE elements, as the atomic number increases an electron is not added to the outermost shell but rather to the inner 4f shell. Due to their diffusive property, 4f electrons do not all distribute with the inner part of the 5s5p shell. An increase in 4f electrons only partly, shields the increase in nuclear charge. It is generally believed that the screening constant of the 4f electrons in trivalent RE ions is about 0.85. The 4f electron is larger but still less than one, therefore, as the atomic number increases the effective attraction between the nucleus and the outer electrons increases. This increased attraction causes shrinkage in the atomic or ionic radius. This phenomenon is referred to as “lanthanide contraction” [16].

One effect of lanthanide contraction is that the radius of trivalent yttrium ion (Y^{3+}) is measured to be between that of Ho^{3+} and Er^{3+}, and the atomic radius of Y is between Nd and Sm. This results in the chemical properties of Y being very similar to those of lanthanide elements. The chemical properties of Y may be similar to the lighter and the heavier RE elements in different systems and this depends on the level of covalent character of the chemical bonds in those systems [16]. Another effect of lanthanide contraction is that the third row of the d – block

elements on the periodic table have only marginally larger atomic radii than the second transition series.

1.2.2. Crystal Structures [14]

As can be seen from Table 1.1, the 17 RE metals exist in one of five crystal structures. At room temperature, nine exist in the hexagonal close–packed (hcp) structure, four in the double c-axis hcp (dhcp) structure, two in the face–centered cubic (fcc), and one in each of the body–centered cubic (bcc) and rhombic (Sm-type) structures. This distribution changes with temperature and pressure as many of the elements go through several structural phase transitions. All of the crystal structures, with the exception of bcc, are close–packed (that is, the number of nearest neighbours, or coordination number, has its maximum possible value of 12). The close–packed structures can be defined by the stacking sequence of the layers of close–packed atoms, as shown in Figure 1.2.

If the three atoms in equivalent sites on a two – dimensional hexagonal lattice are labelled A, B, and C, then the hcp structure is defined by a stacking sequence of ABAB..., dhcp is ABAC..., fcc is ABC... and the eponymous Sm-type is ABABCBCAC... Ideal close packing in the hcp structure is characterized by a lattice parameter ratio of $c/a = \sqrt{(8/3)} \approx 1.633$. As can be seen from Table 1.1, the ratios for the hcp RE metals fall into the range 1.57 – 1.59, indicating that the atoms in the basal (hexagonal) plane are dilated by ~ 3 % with respect to ideal close packing. The corresponding values for the dhcp and rhombic metals, taking into account the extra atoms in the unit cell, indicate a similar dilation. All the heavy RE metals adopt the hexagonal close–packed (hcp) crystal structure and all the light RE metals, with the exception of Sm, adopt the double c-axis hcp (dhcp) structure. The rhombic crystal structure of Sm (Sm–type) can be viewed as a rather exotic mixture of one part fcc and two parts hcp (just as the dhcp structure can be viewed as an equal mix of fcc and hcp).

In the case of intermetallic compounds between the RE elements and the 3d transition metals, a survey of the crystal structure of the various compounds is given in Table 1.1. The majority of the structure types mentioned in Table 1.1 are related and originate from the hexagonal lattice of the $CaCu_4$ – type structure, from which they arise through some simple substitution accompanied by layers shifts [15].

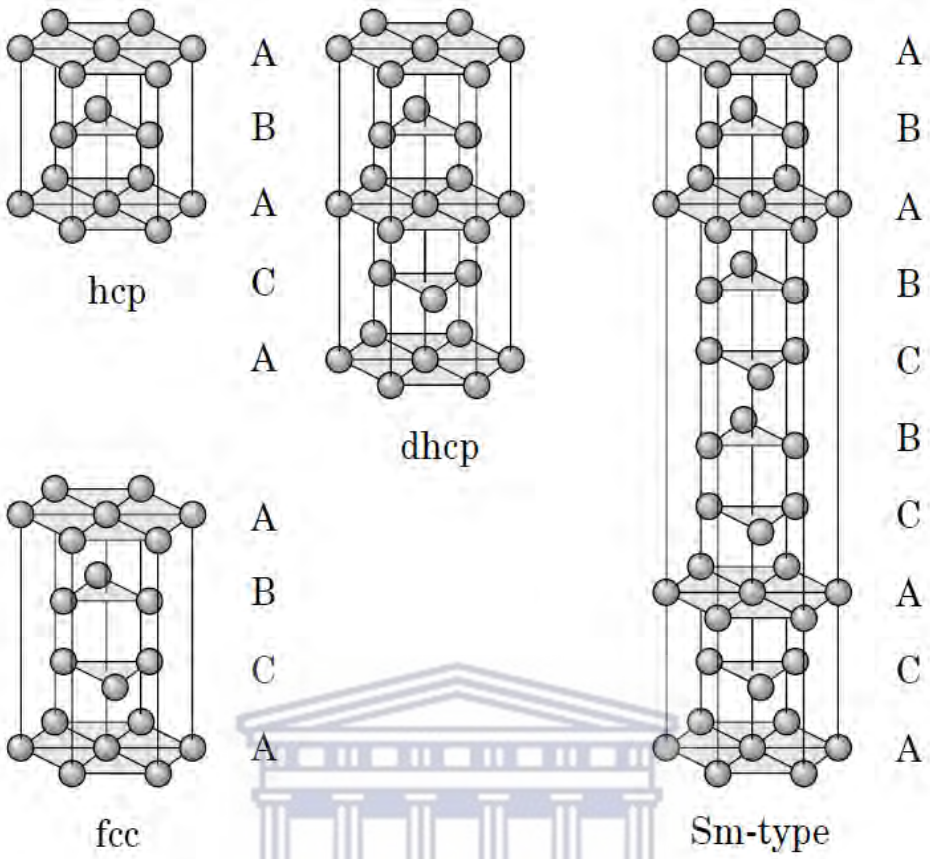

Figure 1.2: Conventional unit cells for the crystal structures based on the hexagonal lattice [14].

1.2.3. Magnetic Structure and Magnetic Properties

Some of the magnetic structures exhibited by the heavy RE metals are shown schematically as a function of temperature in Figure 1.3. Whilst not presenting the subtlety of the spin alignments in some of the more exotic magnetic structures, it does show some of the diversity of the magnetic phases displayed by some of the metals in the RE series. The magnetic moments of the RE metals are dominated by the spin contribution from the highly localized 4f electrons and are thus good examples of local – moment ferromagnets. As the 4f electron shell can accommodate a maximum of 14 electrons, a half–filled shell has seven electrons with parallel spins (according to Hunds' rule, the empirical rule in atomic physics that states that in general, parallel spins are a lower – energy configuration than antiparallel spins). Thus, the 4f electrons contribute 7 μ_B to the total magnetic moment of Gd (~ 7.6 μ_B), and similarly large contributions to the total moments for the other magnetic rare – earth metals.

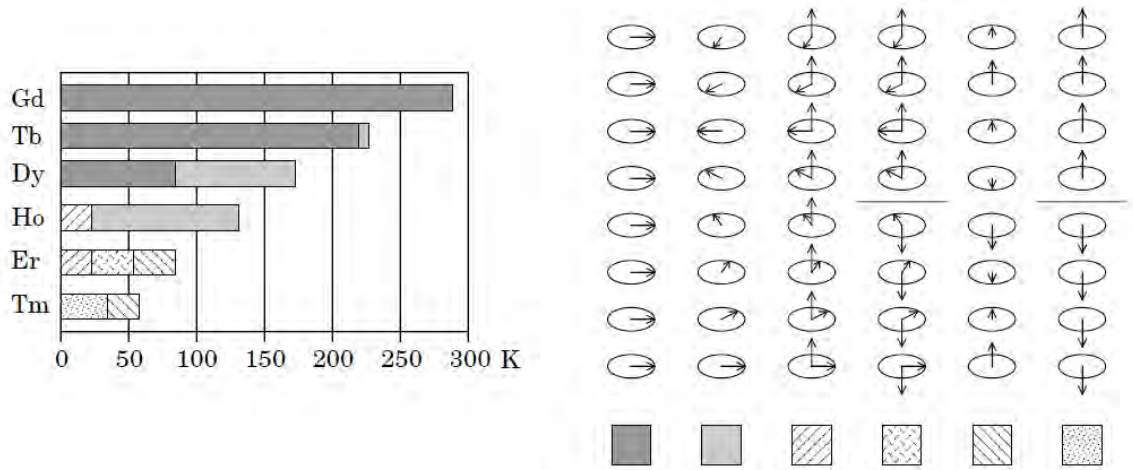

Figure 1.3: Some of the magnetic phases of the heavy RE metals. For each magnetic phase, the arrows represent the changing magnitudes and directions of the components of magnetic moments relative to the basal planes (circles) from one atomic plane to the next [14].

In contrast to the situation with itinerant ferromagnets (based on the magnetic transition metals), the valence electrons contribute a small fraction of the overall magnetic moment per atom – in the case of Gd, the 5d 6s valence electrons contribute 0.6 μ_B, less than 10 % of the total moment. The magnetic structures of the RE metals and many RE – based compounds are well understood as the result of many decades of experimental study and the development of the local spin – density approximation in calculations of the valence electronic structures of solids [14].

Magnetic properties of the RE elements are determined by the 4f electrons, which especially in the case of heavy RE elements (Gd − Tm) are largely unaffected by their environment. Therefore, the well-known quenching of the orbital angular momentum due to the inhomogeneous electric field and neighbouring ions in the crystal does not occur from most RE ions. The orbital angular momentum takes its full value in this case. The spin $\vec{S}$ and the orbital angular momentum $\vec{L}$ are then strongly coupled in the Russell – Saunders coupling scheme $\vec{J} = \vec{L} \pm \vec{S}$, depending upon whether the 4f shell is more than or less than half filled, $\vec{J}$ being the total angular momentum. The magnetic moment for the partially filled shell is given by:

$$\mu = \mu_B g_J J, \tag{1.2}$$

where g_J and μ_B are the Landé factor and the Bohr magneton, respectively, and expressed in the form:

$$g_J = 1 + \frac{[J(J+1) - L(L+1) + S(S+1)]}{2J(J+1)} \tag{1.3}$$

and

$$\mu_B = \frac{e\hbar}{2m}. \tag{1.4}$$

Amongst the RE elements, La, Lu, and Y have no magnetic moment and are often used as a non-magnetic substitute when the dilution of moment bearing RE ions in a compound is desired. The compounds formed with these non-magnetic RE elements have received much attention since they offer a good opportunity to study the origin and the nature of the 3d – electron magnetism.

A well-known property of the RE elements is their incomplete 4f shell which becomes progressively more filled ongoing from La to Lu. The unpaired electrons accommodated in this shell, determine the physical properties of the RE elements and intermetallic compounds. The chemical properties are largely determined by the $5d^1 6s^2$ valence electrons.

Spin, orbital and total angular momentum of the single RE ions are determined by Hund's rule. The corresponding quantum numbers are gathered in Table 1.2 together with the spectroscopic splitting or the Landé factor g_J, values of $g_J[J(J+1)]^{1/2}$ also known as the effective magnetic moment and values of $g_J.J$ [15]. The two latter quantities largely determine the magnetic behaviour in the paramagnetic and magnetically ordered regime, respectively. In most models, the magnetic coupling energy between two localized moments is proportional to $\mathbf{S}_i$. $\mathbf{S}_j$. If the spin coupling remains unchanged within a class of isostructural RE intermetallic compounds the ordering temperatures are expected to scale as $(g_J - 1)^2 J(J+1)$. This number normalized to the value of Gd is also listed in Table 1.2.

Owing to the highly localized character of the 4f wave functions on different RE atoms, they do not overlap [18], therefore, the direct 4f – 4f exchange interaction is negligible. However,

the indirect interaction, which couples the total angular momentum vectors $\overrightarrow{J_m}$ and $\overrightarrow{J_n}$ of nearby RE ions take place via the conduction electrons although their wave functions do not overlap. This interaction is known as the Ruderman – Kittel – Kusaya – Yodisa (RKKY) interaction and is long–ranged and oscillatory. It leads inter alia to the well-known helically and sinusoidally ordered spin structure of the heavy RE elements (See Figure 1.3). As a result of magnetic interaction, the Curie law expression $\chi(T) = C/T$ for the magnetic susceptibility of a non-interacting system of magnetic dipoles is in general changed to the Curie – Weiss expression:

$$\chi(T) = \frac{C}{(T - \theta_p)}, \tag{1.5}$$

where θ_p is the Weiss temperature and C is the Curie constant given by:

$$C = \frac{g_J^2 \mu_B^2 J(J+1)}{3k_B}. \tag{1.6}$$

For the RKKY indirect interaction case under consideration, θ_p is proportional to $\Gamma^2(g_J - 1)^2 J(J+1)$ as well as related to parameters describing the electron band structure, with Γ the exchange coupling integral between the 4f electrons and the conduction band.

1.3. Magnetism

Studies in the field of magnetism and magnetic materials are still developing and evolving, with a good impact on the industry and our daily lives. The study of the magnetic properties of RE metals originated in the 1930s when the ferromagnetism of Gd was discovered, and the paramagnetism of the other heavy elements was investigated. However, the detailed exploration of these properties, and the concurrent development in our understanding of RE magnetism, occurred as a result of two decisive advances in experimental technique during the 1950s. Magnetic materials form the most vital components in many applications. Recent discoveries include magnetic refrigeration and spintronics. In the next section, the basics of magnetism and the different classes of magnetic materials are discussed.

Table 1.2: Ionic properties of RE elements with their splitting factors and their theoretical magnetic moments

RE-ion	Ground term	S	L	J	g_J	$g_J[J(J+1)]^{1/2}$	$g_J J$
La^{3+}	$4f^0\ {}^1S_0$	0	0	–	0	0	0
Ce^{3+}	$4f^1\ {}^2F_{5/2}$	1/2	3	5/2	6/7	2.54	2.14
Pr^{3+}	$4f^2\ {}^3H_4$	1	5	4	5/4	3.58	3.20
Nd^{3+}	$4f^3\ {}^4I_{9/2}$	3/2	6	9/2	8/11	3.62	3.28
Pm^{3+}	$4f^4\ {}^5I_4$	2	6	4	3/5	2.68	2.40
Sm^{3+}	$4f^5\ {}^6H_{5/2}$	5/2	5	5/2	2/7	0.84	0.72
Eu^{3+}	$4f^6\ {}^7F_0$	3	3	0	0	0	0
Gd^{3+}	$4f^7\ {}^8S_{7/2}$	7/2	0	7/2	2	7.94	7
Tb^{3+}	$4f^8\ {}^7F_6$	3	3	6	3/2	9.72	9
Dy^{3+}	$4f^9\ {}^6H_{15/2}$	5/2	5	15/2	4/3	10.63	10
Ho^{3+}	$4f^{10}\ {}^5I_8$	2	6	8	5/4	10.60	10
Er^{3+}	$4f^{11}\ {}^4I_{15/2}$	3/2	6	15/2	6/5	9.59	9
Tm^{3+}	$4f^{12}\ {}^3H_6$	1	5	6	7/6	7.57	7
Yb^{3+}	$4f^{13}\ {}^2F_{7/2}$	½	3	7/2	8/7	4.54	4
Lu^{3+}	$4f^{14}\ {}^1S_0$	0	0	0	–	0	0

1.3.1. Atomic origin of magnetism and magnetic interaction [19, 20]

When describing the atomic origin of magnetism, one has to consider orbital and spin motions of the electrons and the interaction between them. The total orbital angular momentum of a given atom is defined as

$$\vec{L} = \sum_i \vec{l}_i, \tag{1.7}$$

where the summation extends over all electrons. Here, one has to bear in mind that the summation over a complete shell is zero, the only contributions coming from incomplete shells. The same arguments apply to the total spin angular momentum, defined as;

$$\vec{S} = \sum_i \vec{s}_i \ . \tag{1.8}$$

The resultants $\vec{S}$ and $\vec{L}$ thus formed, are rather loosely coupled through the spin–orbit interaction to form the resultant total angular momentum $\vec{J}$:

$$\vec{J} = \vec{L} + \vec{S}. \tag{1.9}$$

This type of coupling is referred to as Russell – Saunders coupling and it has been proved to be applicable to most magnetic atoms, J can assume values ranging from $J = (L - S)$, $(L - S + 1)$, to $(L + S - 1)$, $(L + S)$. Such a group of levels is called a multiplet. The level lowest in energy is called the ground-state multiplet level. A magnetic moment experiences a torque in a magnetic field **B**. The energy of the interaction can be expressed as,

$$\Delta \mathrm{E} = -\vec{\mu} \cdot \vec{\mathrm{B}} \ . \tag{1.10}$$

Both the orbital and spin angular momenta contribute to the magnetic moment of an atomic electron.

Orbital:
$$\mu_{\mathrm{orbital}} = -\frac{\mathrm{e}}{2\mathrm{m}}\vec{\mathrm{L}} \tag{1.11}$$

Spin:
$$\mu_{\mathrm{spin}} = -\mathrm{g}\frac{\mathrm{e}}{2\mathrm{m}}\vec{\mathrm{S}} \tag{1.12}$$

where g is the spin g-factor and has a value of about 2, implying that the spin angular momentum is twice as effective in producing a magnetic moment. The interaction energy of an atomic electron can then be written as

$$\Delta \mathrm{E} = \frac{\mathrm{e}}{2\mathrm{m}}\left(\vec{\mathrm{L}} + 2\vec{\mathrm{S}}\right) \cdot \vec{\mathrm{B}}, \tag{1.13}$$

which when evaluated in terms of the relevant quantum numbers takes the form

$$\Delta \mathrm{E} = \mathrm{g_J}\mu_{\mathrm{B}}\mathrm{m_J B} \tag{1.14}$$

where m_J is the azimuthal quantum number, taken the values, J, J–1, …., –J. For a single spin with no orbital moment we have $m_J = \pm 1$ and $g_J = 2$, hence $U = \pm\mu_B B$.

1.3.2. Classification of magnetic materials

The origin of magnetism lies in the orbital and spin motions of electron and how the electrons interact with one another. The best way to introduce different types of magnetism is to describe how materials differ in their response to magnetism. The main distinction is that in some materials there is no collective interaction of atomic magnetic moments, whereas in other materials there is a very strong interaction between atomic moments.

The magnetic behaviour of materials can be classified into the following five major groups, These are:

- Diamagnetism (DM)
- Paramagnetism (PM)
- Ferromagnetism (FM)
- Antiferromagnetism (AFM)
- Ferrimagnetism (FRI).

Other groups not discussed in this section, are the exotic spin structures mostly observed in RE elements. Which are:

- The helical magnets, e.g. Dy, Ho, Tb and
- The sinusoidal structures, e.g. Re, Tm.

Materials in the first two major groups (DM, PM) are those that exhibit no collective magnetic interactions and are not magnetically ordered. Materials in the last three major groups (FM, AFM, and FRI) exhibit ion – range magnetic order below critical temperature. Ferromagnetic and ferrimagnetic ordering are usually what we consider as being magnetic.

1.3.2.1. Diamagnetism

Diamagnetism is a fundamental property of all matter, although it is usually very weak. It is due to the non – cooperative behaviour of orbiting electrons when exposed to an applied

magnetic field. Experimentally it is characterized by the repulsion of the material from an external magnetism. Diamagnetic substances are composed of atoms that have no net magnetic moments (that is, all orbital subshells are filled and all spins are paired). However, when diamagnetic materials are exposed to a magnetic field, a negative magnetization is produced and thus the susceptibility is negative. Diamagnetism can only be detected by sensitive laboratory instruments. The classical theory of diamagnetism is given by Paul Langevin [21]. The other characteristic behaviour of diamagnetic materials is that the magnetization decrease with increase magnetic field (Figure 1.4a) and the susceptibility is temperature independent (see Figure 1.4b).

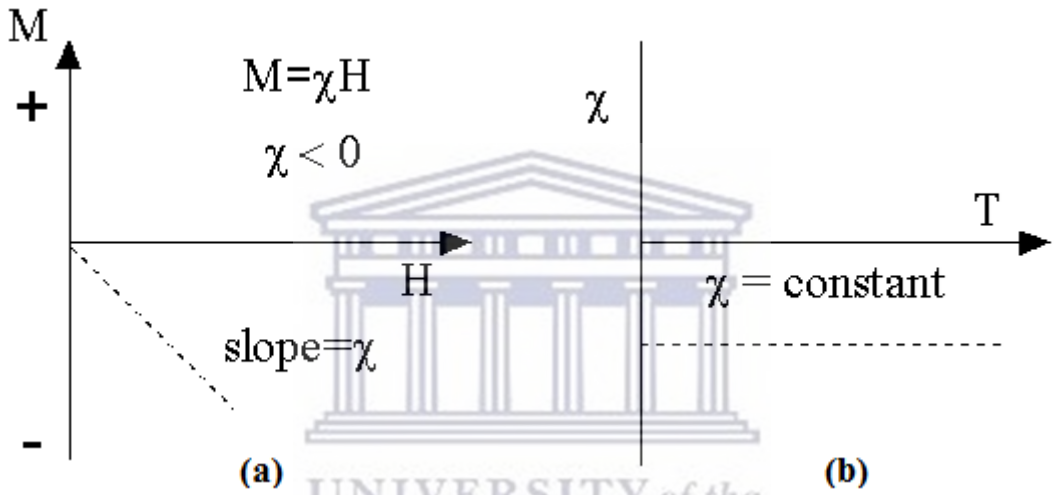

Figure 1.4: (a). Magnetization as a function of magnetic field, (b). Magnetic susceptibility as a function of temperature [22].

1.3.2.2. Paramagnetism

In this class of materials, some of the atoms or ions in the material have a net magnetic moment due to unpaired electrons in partially filled orbitals. Paramagnetism corresponds to a positive susceptibility so that an applied magnetic field induces magnetization which aligns parallel with the applied magnetic field which caused it [23]. Thus, in the presence of a field there is now a potential alignment of the atomic magnetic moments in the direction of the applied field resulting in a net positive magnetization and positive susceptibility. Once the applied field is removed, the materials lose their magnetism as thermal motion randomizes the electron spin orientations.

The efficiency of the field in aligning the moments is opposed by the randomizing effects of temperature. This results in a temperature-dependent susceptibility, known as the Curie law ($\chi(T) = C/T$) (see Figure 1.5). In an applied field, paramagnetic materials behave in the opposite way to diamagnetic materials and tend to be attracted to regions of a strong field. The magnetic moment has two sources that give paramagnetic contributions to the magnetization which are the spin of electrons and their orbital angular momentum about the nucleus [24]. The dipoles of paramagnetic materials do not affect the surrounding dipoles within the material.

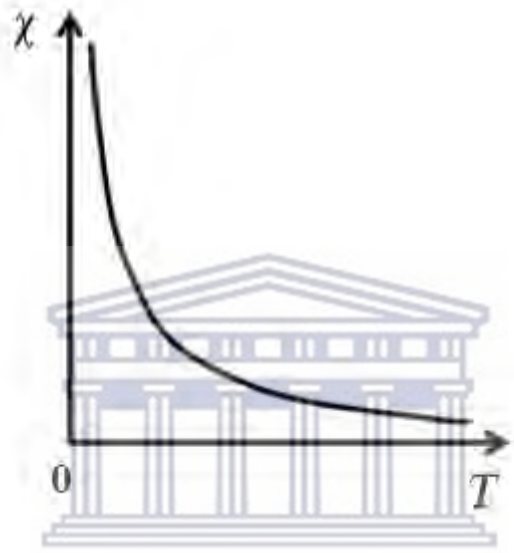

Figure 1.5: Magnetic susceptibility as a function of temperature (Curie law).

1.3.2.3. Ferromagnetism

A ferromagnet has a spontaneous magnetization even in the absence of an applied magnetic field. All moments are aligned parallel to each other (see Figure 1.6). Ferromagnetic substances are those substances that when placed in an external magnetic field, get strongly magnetized. Also, they tend to move from a region of weak to the region of a strong magnetic field and get strongly attracted towards a magnet. In a ferromagnetic material, the individual atoms possess a dipole moment, similar to a paramagnetic material. When placed in a magnetic field, the atoms interact with one another and get spontaneously aligned in a common direction. The direction is common over a macroscopic volume which is termed as a domain (see the section below). The domain has a net magnetization and each domain aligns itself in the direction of the external field, which results in its strong magnetization.

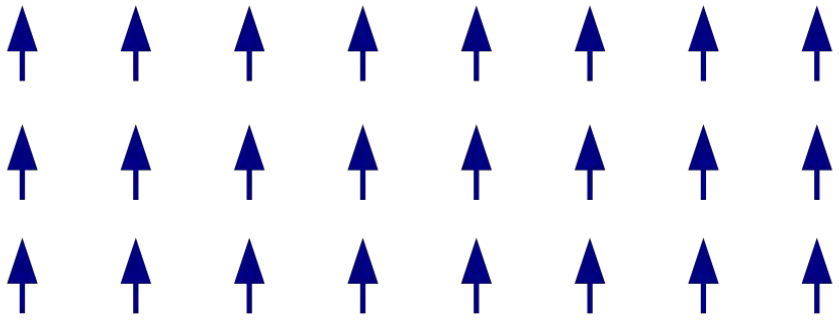

Figure 1.6: Magnetic moments arranged in an ordered manner along a single unique direction parallel to each other.

Two distinct characteristics of ferromagnetic materials is their (a) spontaneous magnetization and the existence of (b) magnetic ordering temperature.

(a) Spontaneous magnetization is the net magnetization that exists inside a uniformly magnetized microscopic volume in the absence of a field. The magnitude of this magnetization, at 0 K, is dependent on the spin magnetic moments of electrons. A related term to spontaneous magnetization is the saturation magnetization which one can measure in the laboratory. The saturation magnetization is the maximum induced magnetic moment that can be obtained in a magnetic field. Beyond this field, no further increase in magnetization occurs (Figure 1.7). The difference between saturation magnetization and spontaneous magnetization has to do with domains (see the section below). Saturation magnetization is an intrinsic property, independent of particle size but dependent on temperature [22].

(b) Magnetic ordering temperature (Curie temperature). Even though the electronic exchange force in ferromagnets is very strong, thermal energy eventually overcomes the exchange and produces a randomizing effect on the moments. This occurs at a particular temperature called the FM transition temperature or simply the Curie temperature (T_C). This temperature depends on the substance, but its order of magnitude is about 1000 K [25]. The Curie temperature is also an intrinsic property and is a diagnostic parameter that can be used for mineral identification [22]. Below T_C, the ferromagnet is ordered and above it, the moments are oriented randomly, resulting in a zero-net magnetization. In this region the substance is paramagnetic, and its susceptibility is given by:

$$\chi(T) = \frac{C}{(T - T_C)}, \tag{1.15}$$

which is known as the Curie – Weiss law. And C is the Curie constant. The Curie – Weiss law is of the same form as the Curie law, except that the origin of temperature is shifted from 0 to T_C (Figure. 1.8).

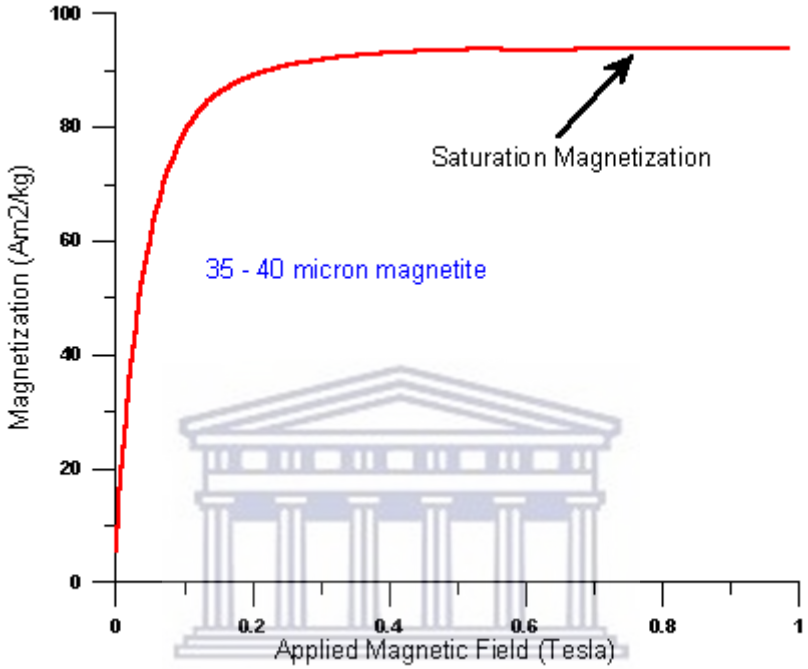

Figure 1.7: Saturation magnetization plot showing the maximum induced magnetic moment that can be obtained in a magnetic field (H_{met}); the red line shows the field where no further increase in magnetization occurs [22].

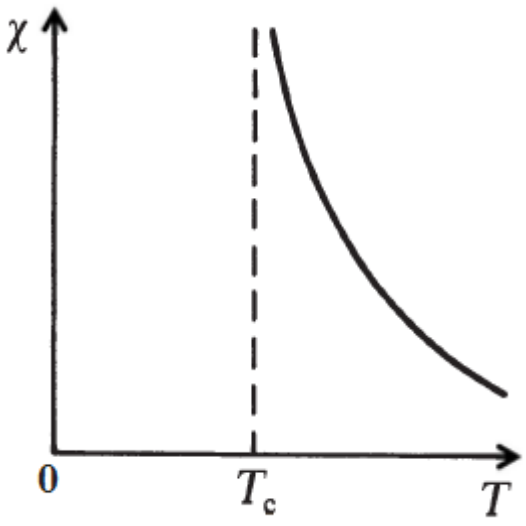

Figure 1.8: Magnetic susceptibility as a function of temperature for FM materials

(c). Ferromagnetic domain

Ferromagnetic materials in their natural state are often found to be not magnetized even below the Curie temperature. To explain this, Weiss suggested that the substance is divided into a large number of small domains in which each domain is magnetized, but the direction of magnetization in the various domains are such that they tend to cancel each other, leading to a zero magnetization (see Figure 1.9). This theoretical postulate of Weiss was confirmed experimentally. The domain structure can be observed by carefully polishing the surface of the ferromagnetic substance and spreading a fine powder of ferromagnetic particles over it.

Magnetic domain structure is responsible for the magnetic behaviour of ferromagnetic material like iron, nickel, cobalt, and their alloys and ferrimagnetic materials like ferrite. This includes the formation of permanent magnets and the attraction of ferromagnetic materials to a magnetic field. The regions separating magnetic domains are called domain walls, where the magnetization rotates coherently from the direction in one domain to that in the next domain (Figure 1.10). The study of the magnetic domain is called micromagnetics, whilst the walls are called Bloch walls.

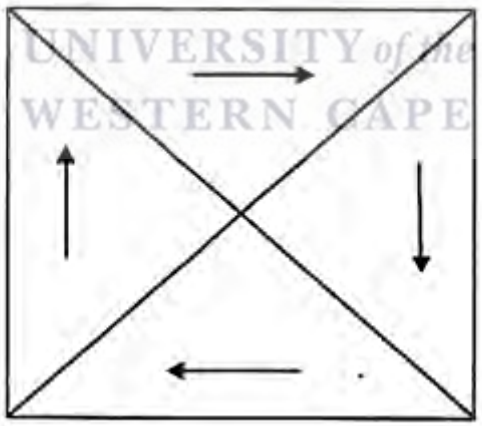

Figure 1.9: Domain configuration according to Weiss hypothesis giving zero resultant magnetization (unmagnetized crystal).

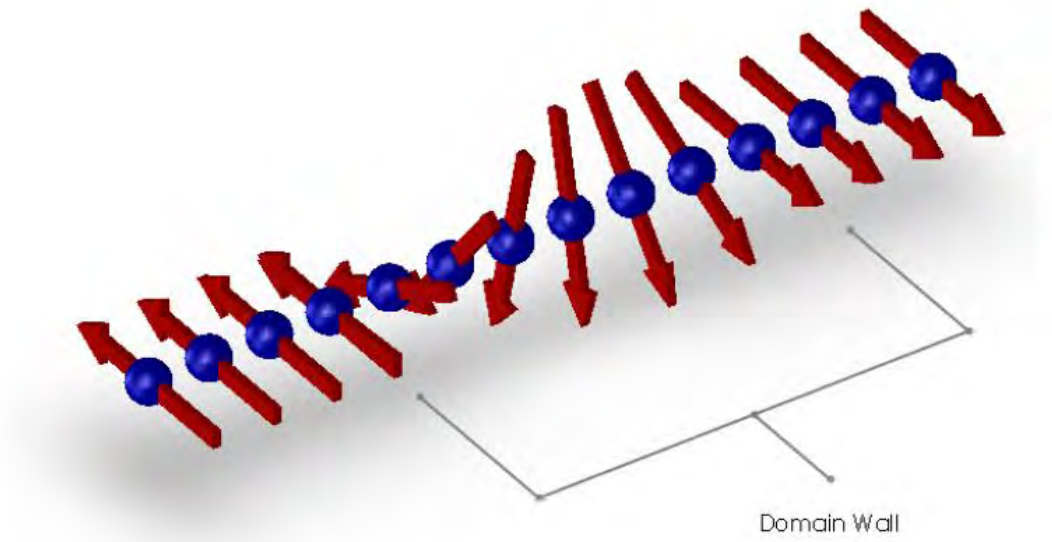

Figure 1.10: Structure of 180° domain wall between two domains in opposite alignment.

Its thickness is not infinitely small, but has a finite value, that is, the spin orientation change gradually in the transition region (Figure 1.11a). In this manner, the spin reversal is accomplished over a number of steps, and hence the spin orientation between two neighbouring moments is rather small, this leads to a reduction of the exchange energy associates with the wall. Another possible description of the wall is the Néel wall (Figure 1.11b). In this description, the spin rotates in a plane perpendicular to the plane of the wall.

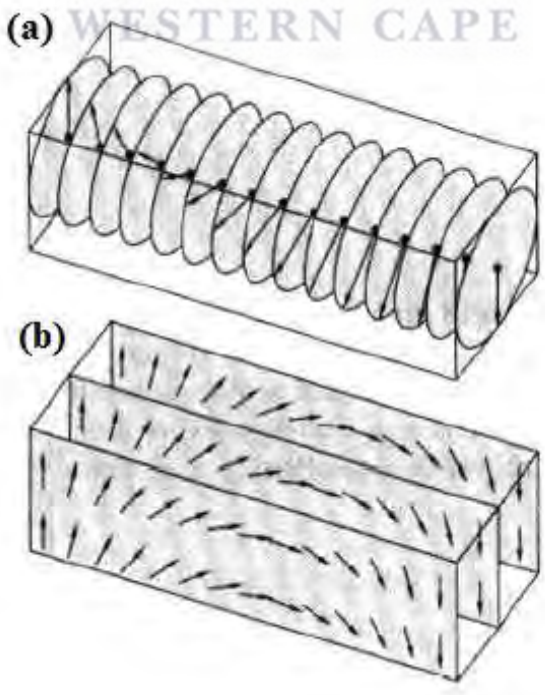

Figure 1.11: (a). Bloch wall, (b). A Néel wall [23].

1.3.2.4. Antiferromagetism

In materials that exhibit antiferromagnetism, the magnetic moments of atoms or molecules, usually related to the spins of an electron, align in a regular pattern with neighbouring spins (on different sublattices) pointing in opposite directions (Figure 1.12). Generally, antiferromagnetic order may exist at sufficiently low temperatures but vanishes at and above a critical temperature called the Néel temperature (T_N) – named after the French Physicist Louis Néel, who had first identified this type of magnetic ordering. Above the Néel temperature, the material is typically paramagnetic and the susceptibility is well represented by the formula:

$$\chi(T) = \frac{C}{(T + T_N)}, \tag{1.16}$$

where C and T_N are constants depending on the substance. This behaviour is shown in Figure 1.13. Thus, the magnetic susceptibility of an antiferromagnetic material typically shows a maximum at the Néel temperature. In contrast, at the transition between the ferromagnetic to the paramagnetic phases, the susceptibility will diverge.

When no external field is applied, the antiferromagnetic structure corresponds to a vanishing total magnetization. In an external magnetic field, a kind of ferrimagnetic behaviour (see section 1.3.2.5) may be displayed in the antiferromagnetic phase, with the absolute value of one of the sublattice magnetizations differing from that of the other sublattice, resulting in a nonzero net magnetization. Although the net magnetization should be zero at a temperature of absolute zero, the effect of spin canting often causes a small net magnetization to develop, as seen for example in hematite [27].

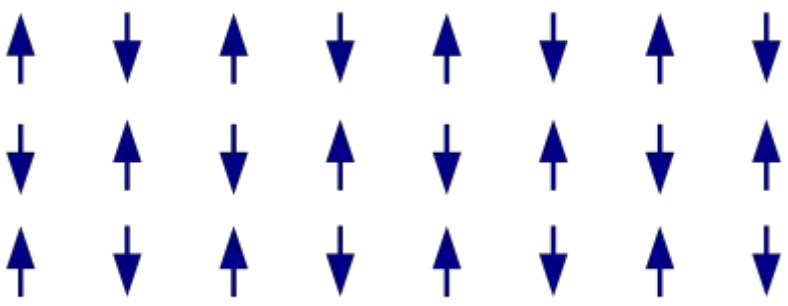

Figure 1.12: Equal magnetic moments of antiferromagnetism lying antiparallel to one another.

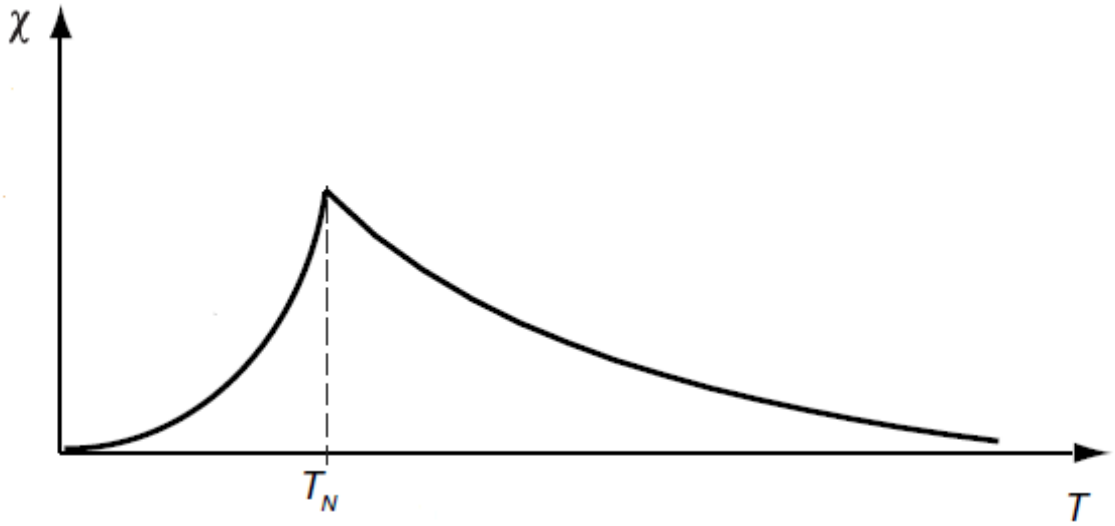

Figure 1.13: Magnetic susceptibility as a function of temperature for AFM materials.

1.3.2.5. Ferrimagnetism

A ferrimagnetic material is one that has populations of atoms with opposing magnetic moments, as in antiferromagnetism; however, in ferrimagnetic materials, the opposing moments are unequal and a spontaneous magnetization remains (see Figure 1.14) [27]. This happens when the populations consist of different materials or ions (such as Fe^{2+} and Fe^{3+}). Ferrimagnetism is exhibited by ferrites and magnetic garnets. The oldest known magnetic substance (iron (II, III) oxide; Fe_3O_4), is a ferrimagnet; it was originally classified as a ferromagnet before Néel discovered ferrimagnetism and antiferromagnetism in 1948 [28]. Ferrimagnetic materials are like ferromagnets in that they hold a spontaneous magnetization below the Curie temperature and show no magnetic order above this temperature (paramagnetic). However, there is sometimes a temperature below the Curie temperature, at which the two opposing moments are equal, resulting in a net magnetic moment of zero; this is called the magnetization compensation point. This compensation point is observed easily in garnets and rare-earth-transition-metal compounds. Furthermore, ferrimagnets may also have an angular-momentum compensation point, at which the net angular momentum vanishes. This compensation point is a crucial point for achieving high-speed magnetization reversal in magnetic memory devices [29].

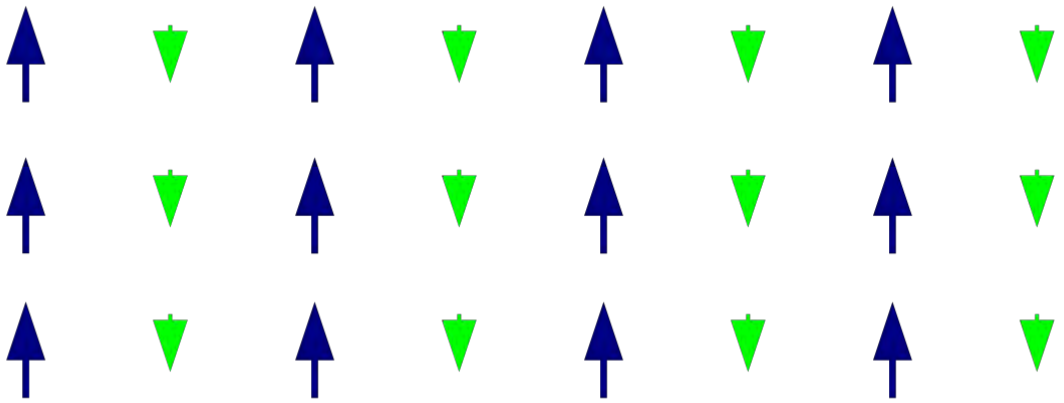

Figure 1.14: Unequal magnetic moments of ferrimagnet lying antiparallel to one another.

1.4. Physical properties

The physical properties investigated in this project include the electrical resistivity, magnetic susceptibility and magnetization, heat capacity and magnetocaloric effect. This section presents in detail the theoretical description of these physical properties.

1.4.1. Electrical Resistivity

The free charge carrier is responsible for electrical transport. The free charge carriers considered here are the free electrons in metals, which are treated as localized wave – packets obeying the exclusion principle, consequently the Fermi–Dirac statistic rather than Boltzmann's statistic. The free electrons involved in the transport properties of a given material are those near the Fermi surface. The states well below the Fermi surfaces are completely full and those well above are completely empty. Thus, electrons near the Fermi surface are able to respond to applied fields [30]. The flow of electron in metal arises from different scattering processes. These scatterings of conduction electrons are due to:

- The imperfection in materials such as dislocations, stacking faults, grain boundaries, or the presence of impurities in the sample. This scattering process gives rise to a residual resistivity.

- The vibrations of ions (phonons) from their equilibrium positions. This scattering process gives rise to the phonon resistivity and increase largely with increasing temperature.
- Deviation from perfect magnetic order in FM or AFM materials as the temperature is increased toward their Curie or Néel temperature. This scattering process gives rise to magnetic contribution and attains its maximum value in the paramagnetic region.
- The electrons also scattering from each other, but for normal metals, this effect is very small. At elevated temperatures, the contribution due to electron–electron interaction for normal metals is negligible due to the dominant electron–phonon scattering [24].

These effects are independent of each other and are expressed by Matthiessen's rule:

$$\frac{1}{\tau} = \sum_i \frac{1}{\tau_i} \quad , \tag{1.17}$$

where τ is the relaxation and *i* denotes the different scattering process. In magnetic materials, the total resistivity originates from three contributions viz. the temperature-independent residual resistivity, the temperature-dependent of both the electron–phonon (ρ_{ph}) contribution, and the scattering of electrons from the ordered magnetic moments (ρ_{mag}). Assuming the validity of the Matthiessen's rule, the temperature dependence of the electrical resistivity of a magnetic material can be written as:

$$\rho(T) = \rho_0 + \rho_{ph}(T) + \rho_{mag}(T), \tag{1.18}$$

where ρ_0 is the temperature-independent residual resistivity, which originates from defects, imperfections, and impurities in the sample. This contribution exhibits a constant value when the temperature is lowered toward absolute zero. The ρ_0 is such a sensitive measure of the perfection of a sample that it is current practice to specify the overall purity and perfection of a metal crystal by quoting the ratio of its resistivity at room temperature to the near-zero temperature as the room – ratio – resistivity (RRR): $RRR = \rho_{300K} / \rho_{2K}$. ρ_{ph} is the temperature-dependent phonon contribution due to the scattering of conduction electrons by the thermal vibration of ions around their equilibrium position. The highest phonon frequency in the Brillouin zone ω_{max} can be estimated roughly from the relation $\hbar\omega_{max} = k\theta_D$, where k

is the radius of the Debye sphere and θ_D is the Debye temperature. Figure 1.15 displays the schematic temperature dependence of the electrical resistivity of RE intermetallic compounds without a d – electron contribution. The temperature variation of the phonon contribution is given by Bloch – Grüneissen law [31]:

$$\rho_{ph}(T) = \frac{4\kappa}{\theta_R}\left(\frac{T}{\theta_R}\right)^5 \int_0^{\theta_R/T} \frac{x^5 dx}{(e^x - 1)(1 - e^{-x})} dx, \qquad (1.19)$$

where κ is the electron–phonon coupling constant. The term θ_R is the characteristic temperature for the lattice resistivity and takes on a numerical value, which differs not much from the Debye temperature θ_D as obtained from specific heat studies [32].

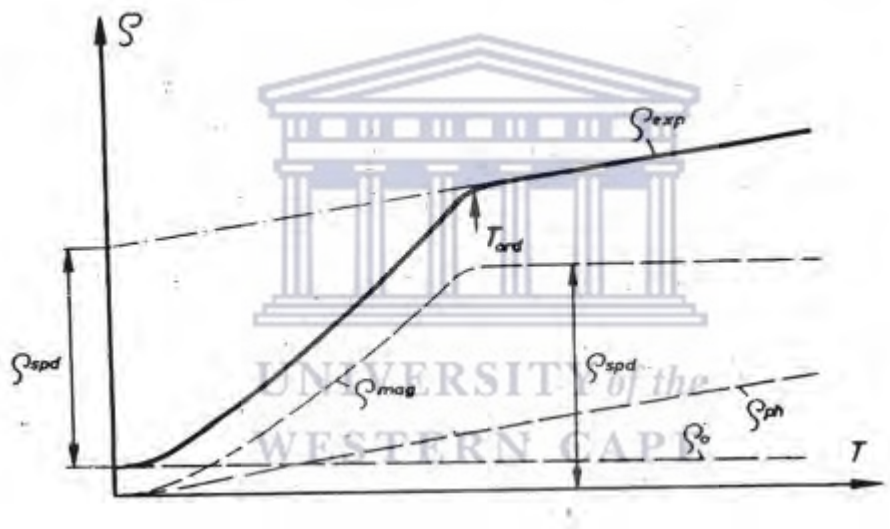

Figure 1.15: Schematic temperature dependence of the electrical resistivity of RE intermetallic compounds without d – electron contribution [35].

The variable *x* is defined as $x = \frac{\hbar\omega}{k_b T}$. At high temperature ($T \geq \theta_R/2$), the integral in Eq. 1.19 reduces to an expression $(\theta_R/T)^4$ and hence $\rho_{ph}(T) \sim T$. In some cases mainly for alloys of d – transition metals, ρ_{ph} deviates from linearity at high temperature, which is due to the *s – d* interband scattering into unfilled *d* – band. This scattering is responsible for an additional term called the Mott's term: $-KT^3$ [33, 34]. At low temperature ($T \geq \theta_R/4$), the ideal or thermal component of the resistivity ($\rho_{ph}(T)$) decreases faster than linearly-roughly as T^3 in many metals and as T^5 in several others, particularly the monovalent ones. The T^5 dependence arises from the fact that the integral in Eq. 1.19 reduces to a constant value of 124.4 [35].

The magnetic contribution arises from the order of the 4f electrons magnetic moments. We may have ordered magnetism, that is, FM, AFM, or helical ordering as in the heavy RE metals. Perfect magnetic order well below the ordering temperature ($T_{ord} = T_C$ or T_N) as T tends to zero leads to the reduction of the scattering of the conduction electrons. With an increase in temperature above the ordering temperature, an increasing spin – disorder scattering occurs and it reaches its maximum value in the paramagnetic region. The $\rho_{mag}(T)$ is characterized by the following traits [35]:

- A temperature-independent behaviour above T_{ord},
- A pronounced kink at $T = T_{ord}$ and
- A strong decrease below T_{ord} with decrease temperature.

The magnitude of the spin – disorder resistivity in the paramagnetic region, $\rho_{mag}(T > T_{ord}) \equiv \rho_{spd}$ obtained by several authors is then given by [36 - 38]:

$$\rho_{mag}(T > T_{ord}) = \rho_{spd} = \frac{3\pi N m^*}{2\hbar e^2 E_F} \lfloor \Gamma \rfloor^2 (g_J - 1)^2 J(J+1). \qquad (1.20)$$

In this equation, N is the number of atoms per unit volume, m^* is the effective electron mass, $\hbar$ is the Planck constant, e is the electron charge and E_F is the Fermi energy. Below T_{ord}, magnetic ordering is described in terms of the concept magnon excitations. For FM materials, several authors were able to obtain an expression $\rho_{mag} \sim T^2$ using the spin-wave treatment [36, 37, 39]. Later on Kasuya [40] used a spin-wave description of the s – f interaction to derive an expression of $\rho_{mag}(T)$ below T_C. He assumed a spin wave dispersion relation of the form $\omega(q) \sim q^2$ and obtained:

$$\rho_{mag}(T) = \frac{\pi^2}{8} \frac{V m^*}{n e^2} \Gamma^2(0) (g_J - 1)^2 J \left(\frac{k_B T}{k_F \Gamma(0)} \right)^2. \qquad (1.21)$$

In this equation, $\Gamma(0)$ is a parameter which describes the strength of the s – f interaction, V is the volume of the crystal and n is the number of atoms in the crystal. Similar results were obtained by Mannari [41] using a different method. In the case when a gap, Δ, in the spin-wave spectrum occurs due to magnetic anisotropy, Mackintosh [42] derives an expression of the magnetic contribution to the total resistivity given in the form:

$$\rho_{mag}(T) = AT^2 exp\left[-\frac{\Delta}{k_B T}\right]. \tag{1.22}$$

On the other hand, considering the magnon dispersion relation of the anisotropic FM materials given in the limit of all vector: $\varepsilon_q = \sqrt{\Delta^2 + Dq^2}$, where ε_q is the energy of excitation, Δ is the anisotropy gap and D is the spin-wave stiffness. Larrea et al [43] suggested an expression of the temperature-dependent electrical resistivity for a condition $k_B T \ll \Delta$ in the form:

$$\rho_{mag}(T) = bT\Delta e^{-\Delta/k_B T}\left[1 + 2\frac{k_B T}{\Delta}\right], \tag{1.23}$$

where b is a constant for a given material which is dependent on the spin-wave stiffness D. The relationship of D with b is such that $D \sim \frac{1}{\sqrt{b}}$, hence the softer the magnons the larger is its contribution to the resistivity [44].

In the case of AFM materials, the assumption of the spin-wave spectrum of $\omega(q) \sim q$ gives a T^4 temperature dependence of the resistivity [45 - 47]. Using the variational approach to the Boltzmann equation, Yamada and Takada [48] propose the calculation of the magnetic contribution of the total resistivity, ρ_{mag}, of AFM materials due to electron – magnon scattering on the s – f model. The resulting temperature dependence of $\rho_{mag}(T)$ is given by [49]:

$$\rho_{mag}(T) \sim \begin{cases} T^5 & for\ \Delta \ll T \ll T_N \\ T exp\left[-\frac{\sqrt{\Delta T_N}}{T}\right] & for\ T \ll T_N, \Delta \end{cases} \tag{1.24}$$

Another description of $\rho_{mag}(T)$ for AFM materials is given by the spin-wave dispersion relation with energy gap Δ in the form:

$$\rho_{mag}(T) = \rho_0 + A_{AFM}\sqrt{\Delta^3 T} exp\left(-\frac{\Delta}{T}\right)\left[1 + \frac{2}{3}\frac{T}{\Delta} + \frac{2}{15}\left(\frac{T}{\Delta}\right)^2\right], \tag{1.25}$$

where the coefficient A_{AFM} is proportional to $D^{-3/2}$ (D being the spin-wave stiffness) and ρ_0 is the temperature-independent residual resistivity.

1.4.2. Magnetization and magnetic susceptibility

The magnetization M of a material is defined as the magnetic moment per unit volume. A magnetic field can be described by either of two vectors: the magnetic induction $\vec{B}$ or the magnetic field intensity $\vec{H}$ which are related in a vacuum by $\vec{B} = \mu_0\vec{H}$, where $\mu_0 = 4\pi \times 10^{-7}$Hz/m is the permeability of free space. When a material medium is placed in a magnetic field, the medium is magnetized. This magnetization is described by the magnetization vector $\vec{M}$, the dipole moment per unit volume. The magnetic moment of an atom or ion in free space is given by;

$$\vec{\mu} = -\mathrm{g}_J\mu_B\vec{J} \tag{1.26}$$

where g_J is the Landé g – factor given in Eq. 1.3. For electron spin, $g_J = 2.0023$, usually taken as 2 [24], $\vec{J}$ is the total angular momentum.
The energy levels of a system in a magnetic field are:

$$U = -\vec{\mu}.\vec{B} = m_J\mathrm{g}_J\mu_B B \tag{1.27}$$

where m_J is the azimuthal quantum number, taken the values, J, J–1, …. , –J. For a single spin with no orbital moment, we have $m_J = \pm 1$ and $\mathrm{g}_J = 2$, hence $U = \pm\mu_B B$. The energy is split into two energy levels. In a magnetic field, an atom with total angular momentum J has 2J+1 equally spaced energy levels. In this case, the magnetization is given by [24]:

$$M(B) = N\frac{\sum_{m_J=-J}^{+J} m_J\mathrm{g}_J\mu_B exp\left[-\frac{m_J\mathrm{g}_J\mu_B}{k_BT}\right]}{\sum_{m_J=-J}^{+J} exp\left[-\frac{m_J\mathrm{g}_J\mu_B}{k_BT}\right]}, \tag{1.28}$$

where N is the number of atoms per unit volume. Eq. 1.28 can also be expressed in terms of the Brillouin function, $B_J(x)$ in the form:

$$M(B) = NJg_J\mu_B B_J(x); x \equiv \frac{Jg_J\mu_B B}{k_B T}, \tag{1.29}$$

where $B_J(x)$ is defined by:

$$B_J(x) = \frac{2J+1}{2J} coth\left[\frac{(2J+1)x}{2J}\right] - \frac{1}{2J} coth\left[\frac{x}{2J}\right]. \tag{1.30}$$

The behaviour of the magnetization is similar to that of the Brillouin function which increases rapidly at low field and tends to saturation at high field (see Figure 1.16).

In the low field limit, $x << 1$, the trigonometric function can be approximated as follows:

$$\coth(x) \approx \frac{1}{x} + \frac{x}{3} - \frac{x^3}{45} + \cdots \tag{1.31}$$

and the magnetization is given by

$$M(B) = N\frac{g_J^2\mu_B^2 J(J+1)}{3k_B T}B. \tag{1.32}$$

Since the magnetization is induced by the field, we may assume that M is proportional to B, that is, $M = \chi B$, the proportionality constant χ being the magnetic susceptibility of the medium, which is the measure of the ease with which a material acquires the magnetization. Therefore, one obtains:

$$\chi(T) = \frac{M}{B} = \frac{Ng_J^2 J(J+1)\mu_B^2}{3k_B T} = \frac{N\mu_{eff}^2\mu_B^2}{3k_B T} = \frac{C}{T}. \tag{1.33}$$

In this equation C is the Curie constant and μ_{eff} is the effective magnetic moment, both defined as;

$$C = \frac{Ng_J^2 J(J+1)\mu_B^2}{3k_B T};\ \mu_{eff} = g_J\sqrt{J(J+1)}. \tag{1.34}$$

Eq. 1.33 is known as the Curie law and shown schematically in Figure 1.17a.

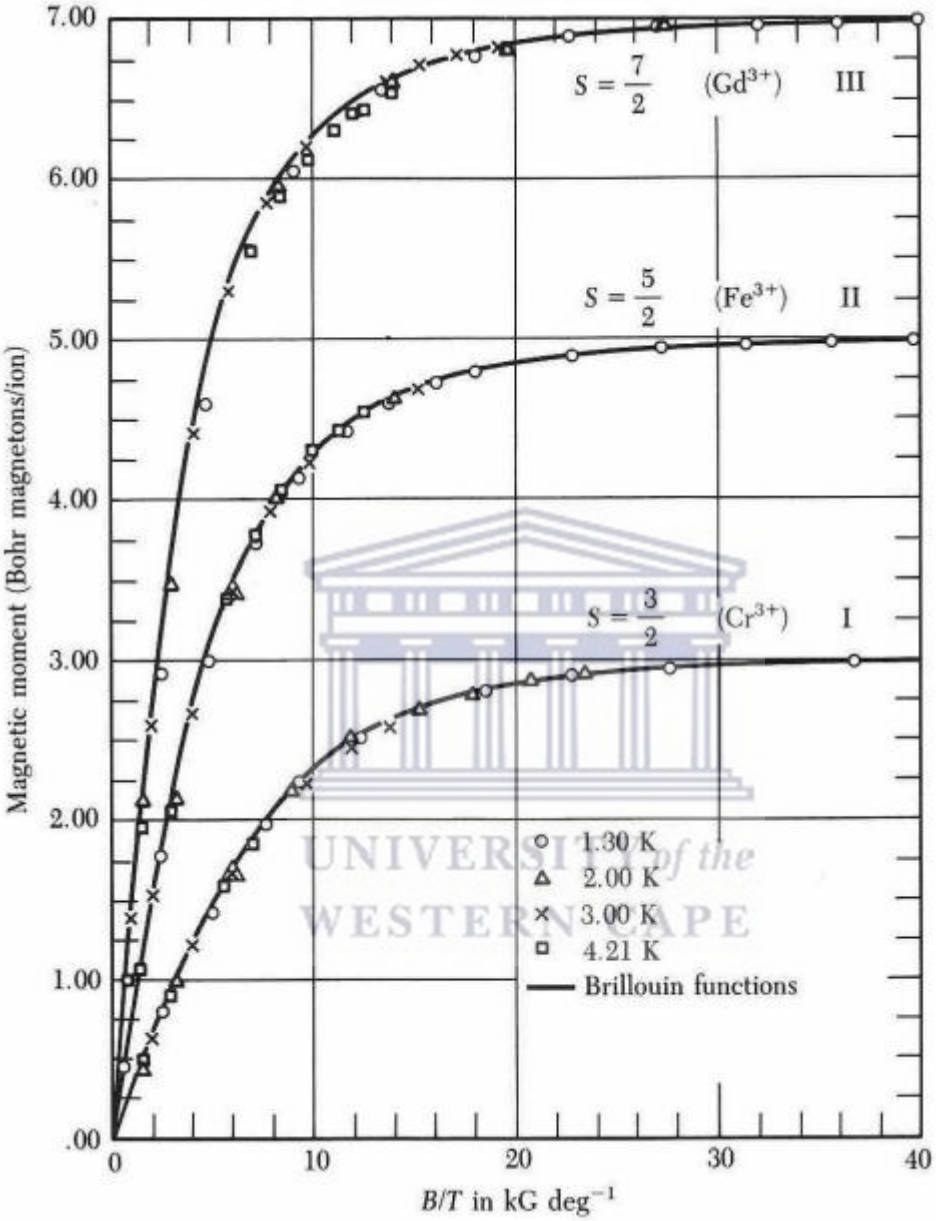

Figure 1.16: Magnetic moment versus B/T for samples of (I) potassium chromium alum, (II) ferric ammonium alum, and (III) gadolinium sulfate octahydrate. Over 99.5% of magnetic saturation is achieved at 1.3 K and about 5 T [24].

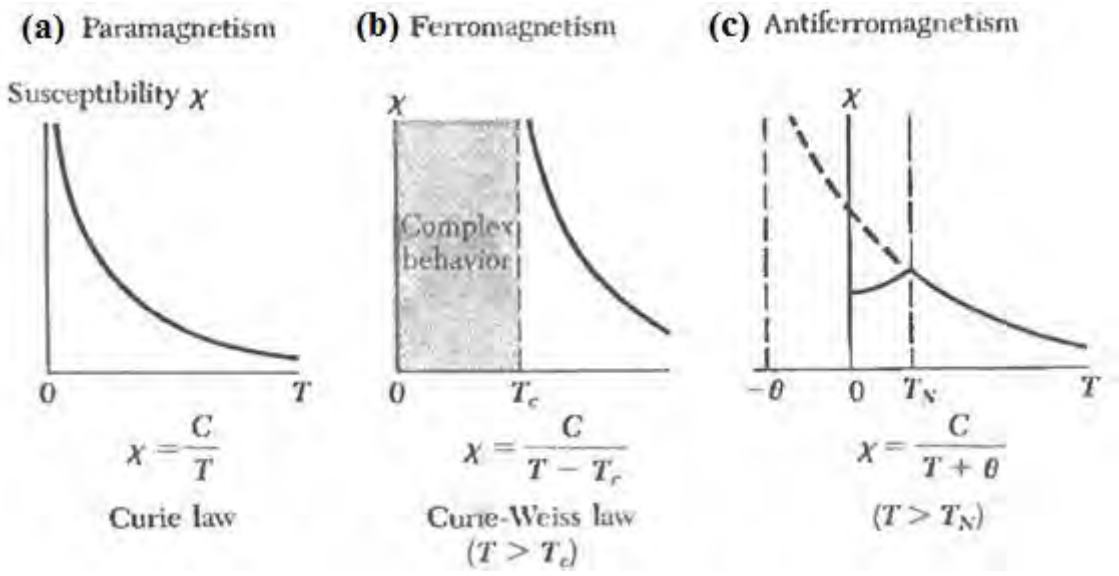

Figure 1.17: Temperature dependence of the magnetic susceptibility (a) paramagnets, (b) ferromagnets and (c) antiferromagnets. Below the Néel temperature of an antiferromagnet the spins have antiparallel orientations, the susceptibility attains its maximum value at T_N where there is a well-defined kink in the curve of χ – versus T. The transition is also marked by peaks in the heat capacity and the thermal expansion coefficient [24].

Deviation of the Curie law occurs for magnetically ordered materials as mentioned above. In the case of ferromagnetic materials, the Curie temperature, T_C is the temperature above which the spontaneous magnetization vanishes. T_C separates the disordered paramagnetic phase at $T > T_C$ from the ordered ferromagnetic phase at $T > T_C$. In the mean field approximation, we assume each magnetic atom experiences a field proportional to the magnetization:

$$B_E = \lambda M, \tag{1.35}$$

where λ is a constant, independent of temperature. T_C can be obtained from λ as follows; considering the paramagnetic region $(T > T_C)$, an applied magnetic field, B_a will cause a finite magnetization and this, in turn, will cause a finite exchange field B_E. Therefore, the paramagnetic susceptibility, χ_P is given by:

$$\chi_P = \frac{M}{(B_a + B_E)}. \tag{1.36}$$

Indeed the paramagnetic susceptibility is given by the Curie law (Eq. 1.34). Substitution of Eqs. 1.34 and 1.35 into Eq. 1.36, gives:

$$\chi = \frac{C}{(T - C\lambda)} = \frac{C}{(T - T_C)}. \tag{1.37}$$

The susceptibility has a singularity (infinite) at $T_C = \lambda C$ and below this temperature there exit a spontaneous magnetization. Eq. 1.37 is known as the Curie − Weiss law. The temperature dependence of FM material is shown in Figure 1.17b. In the case of antiferromagnetic materials in which the spins are ordered antiparallel arrangement, there is a zero-net moment at temperatures below the Néel temperature T_N.

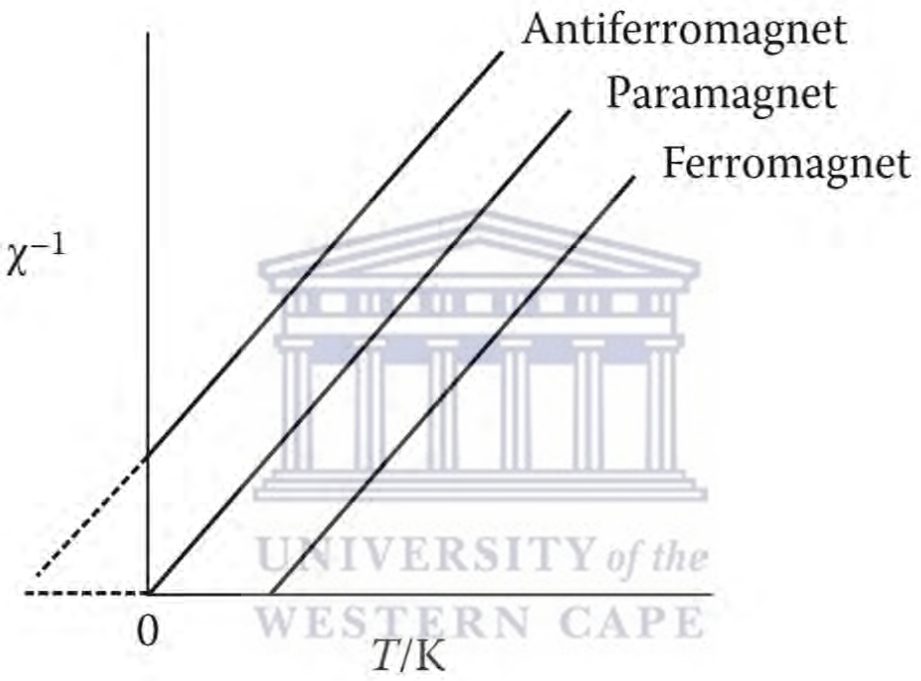

Figure 1.18: Variation of χ^{-1}as a function of temperature (extrapolated from high temperature) for a paramagnet, ferromagnet, and an antiferromagnet. In each case the $\chi^{-1} = 0$ intercept value allows the calculation of the Weiss constant,Θ [26].

The susceptibility of an antiferromagnet is not infinite at T_N, but has a weak cusp as shown in Figure 1.17c. The susceptibility in the paramagnetic region $T > T_N$ is given by:

$$\chi = \frac{2C}{(T - T_N)}. \tag{1.38}$$

The experiment results at $T > T_N$ are usually given in the form:

$$\chi = \frac{2C}{(T+\theta)}, \tag{1.39}$$

where θ is the Weiss temperature. The temperature dependence of the inverse magnetic susceptibility, $\chi^{-1}(T)$ of the paramagnet, ferromagnet and antiferromagnet is shown in Figure 1.18.

1.4.3. Heat capacity

The specific heat per mole is defined as:

$$C = \frac{\Delta Q}{\Delta T}, \tag{1.40}$$

where ΔQ is the heat required to raise the temperature of one mole by an amount equal to ΔT. If the process is carried out at constant volume, then $\Delta Q = \Delta U$, where ΔU is the increase in the internal energy of the system. Therefore, the specific heat at constant volume C_v is given by:

$$C_v = \left(\frac{\partial U}{\partial T}\right)_v. \tag{1.41}$$

The specific heat of a given material originates from various contributions. These are the lattice or phonon, C_L, the electronic contribution C_e which is one of the most important quantities used to distinguish normal metal and heavy – fermion material; the magnetic contribution C_{mag} and the Schottky term, C_{Sch}. The resulting total specific heat capacity is given by:

$$C_v(T) = C_L(T) + C_e(T) + C_{mag}(T) + C_{Sch}(T). \tag{1.42}$$

1.4.3.1. Lattice or phonon specific heat

Lattice specific heat depends on the temperature in the manner shown in Figure 1.19 [25]. At high temperatures C_L tends to a constant value $3R$ (R is the universal gas constant) regardless of the substance. This description is called the Dulong – Petit law. At low-temperatures exact solution of C_L is given by the Debye expression in the form [24]:

$$C_L(T) = 9Nk_B\left(\frac{T}{\theta_D}\right)^3 \int_0^{\theta_D/T} \frac{x^3 e^x}{(e^x-1)^2}\,dx, \tag{1.43}$$

with $x = \frac{\hbar\omega}{k_B T}$, ω is the frequency of the Debye oscillator, *N* the number of atoms per formula unit and θ_D, the characteristic Debye temperature of the compound. For $T << \theta_D$, in the long wavelength limit, C_L can be approximated as:

$$C_L(T) = \frac{12\pi^4}{5} Nk_B\left(\frac{T}{\theta_D}\right)^3. \tag{1.44}$$

Experimentally the lattice heat capacity of RE based compounds are obtained from their non – magnetic La, Y or Lu based compounds.

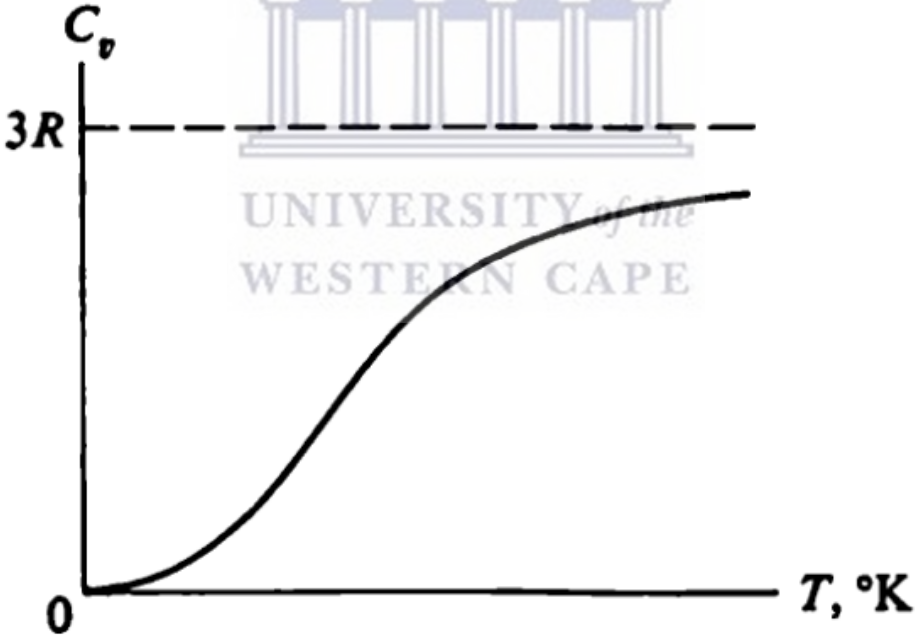

Figure 1.19: Dependence of specific heat of solids on temperature [25].

1.4.3.2. Electron specific heat

From the Drude – Lorentz model, it is well known from the kinetic theory of gases that a free particle in equilibrium at temperature T has an average of $\frac{3}{2}k_BT$ according to the equipartition theorem. Therefore, the average energy per mole is;

$$U = N_A\left(\frac{3}{2}k_BT\right) = \frac{3}{2}RT, \tag{1.45}$$

where N_A is the Avogadro's number. The electrons' heat capacity is then given by;

$$C_e = \frac{\partial U}{\partial T} = \frac{3}{2}N_Ak_B = \frac{3}{2}R. \tag{1.46}$$

Although the Drude model was fairly successful in describing the electron motion within metals, it has some erroneous aspects: for instance, the assumed additional electronic heat capacity to the lattice heat capacity, namely $\frac{3}{2}k_B$ per electron at elevated temperatures is also inconsistent with experimental values since measurements of metals show no deviation from the Dulong–Petit law. The observed electronic contribution of electrons to heat capacity is usually small than the classical value given by Eq. 1.46 by a factor of 10^{-2}. This paradox was solved by Arnold Sommerfeld after the discovery of the Pauli Exclusion Principle, who recognized that the replacement of the Boltzmann distribution with the Fermi–Dirac distribution was required, and incorporated it in the free electron model [50]. The solution of the electronic specific heat was derived within the free electron model in the form [24]:

$$C_e(T) = \frac{\pi^2}{2}\frac{Nk_B^2T}{E_F} = \frac{\pi^2}{2}k_B\left(\frac{T}{T_F}\right), \tag{1.47}$$

where E_F and T_F are the Fermi energy and the Fermi temperature, respectively. Compared to the classical result (Eq. 1.46), it can be concluded that this result is depressed by a factor of $\frac{\pi^2}{3}\frac{k_B^2T}{E_F}$ which is at room temperature of the order of magnitude 10^{-2}. This explains the absence of an electronic contribution to the heat capacity as measured experimentally.

1.4.3.3. Magnetic specific heat and magnetic entropy

In the case of magnetic materials, the localized magnetic moment gives rise to magnetic heat capacity. This contribution results from thermal excitation of spin waves. The spin-wave is quantized in much the same way as lattice waves. The unit of quantization (or magnetic excitation) is called the magnons. Depending on the type of order, there is two principal types of magnons: the FM and AFM magnons. The difference between these two types arises from the dispersion relation. A magnon of wave vector $\vec{q}$ carries an energy $E = \hbar\omega(\vec{q})$, where $\omega(\vec{q})$ is the dispersion relation. In the long-wavelength limit, $\omega \cong Aq^2$. The number of magnon in the mode $\vec{q}$ at thermal equilibrium is given by the Bose–Einstein function;

$$\bar{n}(q) = \frac{1}{e^{\hbar\omega(q)/k_BT} - 1}, \tag{1.48}$$

thus, the energy is given by:

$$\bar{E} = \int_0^{\omega_{max}} \hbar\omega\bar{n}\,\mathrm{g}(\omega)d\omega, \tag{1.49}$$

where $\mathrm{g}(\omega)$ is the magnon density of state and can be calculated from the dispersion relation. In the long-wavelength approximation, the energy is found to be $\bar{E}{\sim}T^{5/2}$ and hence the ferromagnetic heat capacity takes the form:

$$C_{mag}(T) = S_F R\left(\frac{k_BT}{2Js}\right)^{3/2}, \tag{1.50}$$

where S_F is a constant that depends on the crystal structure that has been calculated for several lattices, J is the exchange term and S is the spin angular momentum. In the presence of the energy gap in the spin-wave dispersion, the magnon specific heat is then approximated by:

$$C_{mag}(T){\sim}T^{3/2}exp\left(-\frac{E_\mathrm{g}}{k_BT}\right), \tag{1.51}$$

where E_g is the energy gap.

The heat capacity of a ferromagnet can be expressed in the form:

$$C_v(T) = \gamma T + \beta T^3 + \delta T^{3/2}, \tag{1.52}$$

for gapless ferromagnet, and

$$C_v(T) = \gamma T + \beta T^3 + \delta T^{3/2} exp\left(-\frac{E_g}{k_B T}\right), \tag{1.53}$$

for ferromagnet with energy gap.

In the case of AFM materials, in the long-wavelength limit, the dispersion relation is $\omega \sim q$, and gives a corresponding density of magnons, $\bar{n} \propto \omega^2$. The low-temperatures specific heat of antiferromagnet is given by;

$$C_{mag}(T) = S_{AF} R \left(\frac{k_B T}{2J's}\right)^3, \tag{1.54}$$

where S_{AF} is the term which depends both on the crystal and magnetic structure of the material and J' is the exchange term. Similar to the ferromagnet, in the presence of energy gap, E_g, in the spin-wave dispersion, the magnon specific heat is then approximated by;

$$C_{mag}(T) \sim T^3 exp\left(-\frac{E_g}{k_B T}\right). \tag{1.55}$$

Thus, the total low-temperature heat capacity of an antiferromagnet can then be written as:

$$C_v(T) = \gamma T + \beta T^3 + \delta T^3, \tag{1.56}$$

for a gapless antiferromagnet, and

$$C_v(T) = \gamma T + \beta T^3 + \delta T^3 exp\left(-\frac{E_g}{k_B T}\right), \tag{1.57}$$

for antiferromagnet with energy gap. The T^3 dependence of C_{mag} of a gapless AFM material is of the same form as the lattice heat capacity at low temperatures and makes an experimental separation of spin-wave and lattice specific heat very difficult for antiferromagnets. In case of AFM Kondo lattice compound (Kondo lattice compounds are characterized by a $-lnT$ increase resistivity with decreasing temperature), $C_{mag}(T)$ in the ordered state is often modelled by the formula:

$$C_{mag}(T) = \gamma_{AFM}T + cE_g^{7/2}\sqrt{T}\exp\left(-\frac{E_g}{T}\right) \times \left[1 + \frac{39}{20}\frac{T}{E_g} + \frac{51}{32}\left(\frac{T}{E_g}\right)^2\right]. \quad (1.58)$$

In this equation the first term signifies the contribution from heavy quasiparticles and the second term represents AFM magnons contribution. The approach assumes a spin-wave dispersion relation of the form $\omega^2 = E_g^2 + Dq^2$, where D is the spin-wave stiffness. The coefficient c in Eq. 1.58 is related to D as $c \sim D^{-3}$.

Another interesting quantity associated with the magnetic heat capacity is the magnetic entropy, defined as follows:

$$S_{mag}(T) = \int_0^T \frac{C_{mag}(T')}{T'}dT' \quad or \quad S(T) = \int_0^T \frac{C_p(T')}{T'}dT' . \quad (1.59)$$

For a magnetic system with weak interacting local moments as in RE atoms, such particles possess an intrinsic total angular momentum J and the ground state is populated and the magnetic entropy saturates to a constant value:

$$S_{mag} = Rln(2J + 1). \quad (1.60)$$

The temperature at which the entropy saturates provides information about the crystalline electric field (CEF) effects. CEF effect lead to the splitting of the ground state into different discrete energy levels. The occupation of these energy levels gives rise to an additional contribution to the magnetic heat capacity, $C_{mag}(T)$ known as the Schottky term C_{Sch}. The standard formula for the Schottky contribution to the magnetic specific heat is given by [51]:

$$C_{Sch}(T) = \frac{R}{T^2}\left[\frac{\sum_i g_i \Delta_i^2 e^{-\frac{\Delta_i}{k_B T}} - \left(\sum_i g_i \Delta_i e^{-\frac{\Delta_i}{k_B T}}\right)^2}{\left(\sum_i g_i g^{-\frac{\Delta_i}{k_B T}}\right)^2}\right], \quad (1.61)$$

where Δ_i is the energy in units of temperature and g_i is the degeneracy of the CEF split energy level. Experimentally, the Schottky anomaly is characterized by a board maximum in the $C_{mag}(T)$ curve at high temperatures.

1.4.4. Magnetocaloric effect (MCE)

Magnetocaloric properties are a central point of investigation in the present thesis and will be presented in more details. Moreover, MCE is a topic of current interest because of its possible application in magnetic refrigeration (MR) near room temperature [52, 53].

1.4.4.1. Introduction

MR based on the MCE of refrigerant is taken as a technique that is more environmentally friendly, it has attracted more increasing interests of international research communities for its high-efficiency, and energy saving capabilities as compared to traditional vapor compression refrigerators used at room temperature. Furthermore, it is an environment-friendly cooling technology with a better cooling efficiency as well as compactness [54 - 58]. The MCE is an intrinsic magneto – thermal response for the application or removal of a magnetic field, which can be characterized by the coupled variations of two quantities: the adiabatic temperature change (ΔT_{ad}) and/or the isothermal magnetic entropy change (ΔS_M). To satisfy practical application, the current intensive research in literature aims in probing new magnetic materials exhibiting a large/giant MCE as magnetic refrigerants with a small change in the magnetic field near room temperature or at their magnetic transition temperature.

For instance, the RE Gd element has been intensively investigated for its use as an active magnetic refrigerant near room temperature [7]. Later investigations show that $Gd_5Gi_2Ge_2$ alloys exhibit giant MCE with a typical value of 18.5 J/kg.K [7]. Similar large values of MCE were observed in some Heusler [59 - 62] and perovskites alloys [63, 64]. However, most of these materials undergo a first–order magnetic phase transition. The magnetic entropy change

is large in these materials, but they show large thermal and field hysteresis on a variation of magnetization with temperature and magnetic field, respectively, which act as a drawback for their usage in practical application. Henceforth, more interest was focused on the search of new advanced magnetic materials with second–order magnetic phase transition, showing a large reversible magnetic entropy change, ΔS_M at low applied magnetic fields. Recently, the RE based compounds and oxides, which exhibits the large reversible MCEs and refrigerant capacity with small or zero hysteresis have been of great interest [65 – 71].

1.4.4.2. Thermodynamic approach to MCE [72]

In this section, a brief description of thermodynamic relations on how to define the magnetocaloric response of material is presented. Also, the different figures of merit that permit us to compare materials' performance have to be defined as they will be used throughout the thesis.

a) Basis thermodynamic relations

The magnetic effect is introduced in the thermodynamic system via the performed magnetic work, using the principles of energy conservation:

$$dU = dQ - dW, \tag{1.62}$$

where U, Q and W are the internal energy, the heat flux and the performance work, respectively. In a quasistatic process of magnetic material involved in this thesis, the different work terms are the mechanical work expressed as $dW_{mec} = pdV$ (where p is the pressure and V is the volume) and the magnetic work expressed as $dW_{mag} = -\mu_0 Hdm$ (where H is the magnetic field, μ_0 is the permeability of the free space and m is the magnetic moment). Considering a quasistatic heat flux ($dQ = TdS$, where T is temperature and S is entropy), in a close system the energy conservation can be expressed as:

$$dU = TdS - pdV + \mu_0 Hdm. \tag{1.63}$$

In this equation, the internal energy is a function of entropy, volume and magnetic moment: $U(S,V,m)$. Legendre transformation can be used to obtain different thermodynamic potentials as a function of other parameters. An example is the Gibbs free energy as the useful potential:

$$G(T,p,H) = U - TS + pV - m\mu_0 H. \tag{1.64}$$

From this equation the derivative of G with respect to T at constant pressure and magnetic field and with respect to H at constant pressure and temperature gives the entropy and the magnetic moment, respectively:

$$S = -\left(\frac{\partial G}{\partial T}\right)_{p,H}; m = -\frac{1}{\mu_0}\left(\frac{\partial G}{\partial H}\right)_{p,T}. \tag{1.65}$$

The derivative of S with respect to H at constant p and T and the derivative of m with respect to T at constant p and H, yields the Maxwell thermodynamic relation:

$$\left(\frac{\partial S}{\partial H}\right)_{p,T} = \mu_0\left(\frac{\partial m}{\partial T}\right)_{p,H}. \tag{1.66}$$

These thermodynamic relations can be further extended to obtain an analytical expression for MCE, which is defined as the reversible temperature change produced upon a magnetic field change in an adiabatic process. This gives an expression of the entropy as a function of H and T:

$$dS = \left(\frac{\partial s}{\partial T}\right)_{p,H} dT + \left(\frac{\partial S}{\partial H}\right)_{p,T}, \tag{1.67}$$

and considering $dS = 0$, one obtained:

$$dT = -\mu_0\left[\left(\frac{\partial s}{\partial T}\right)_{p,H}\right]^{-1}\left(\frac{\partial S}{\partial H}\right)_{p,T} dH. \tag{1.68}$$

Taking the definition of the heat capacity at constant p, H, one obtained:

$$C_{p,H} = \left(\frac{dQ}{dT}\right)_{p,H} = T\left(\frac{dS}{dT}\right)_{p,H}. \tag{1.69}$$

Combining Eq. 1.66 and 1.69, one obtained:

$$dT = -\mu_0 \frac{T}{C_{p,H}}\left(\frac{\partial m}{\partial T}\right)_{p,H}. \tag{1.70}$$

Eq. 1.70 gives the total temperature change due to a magnetic field as:

$$\Delta T_{ad} = -\mu_0 \int_{H_1}^{H_2} \frac{T}{C_{p,H}}\left(\frac{\partial m}{\partial T}\right)_{p,H} dH, \tag{1.71}$$

where H_1 and H_2 are the initial and final magnetic fields, respectively. In addition, MCE is also commonly characterized as the magnetic entropy change due to magnetic field change in an isothermal process ($dT = 0$). Therefore Eq. 1.67 takes the form:

$$dS = \left(\frac{\partial S}{\partial H}\right)_{p,T} dH = \mu_0 \left(\frac{\partial m}{\partial T}\right)_{p,H} dH, \tag{1.72}$$

and the total magnetic entropy change due to a magnetic field is expressed as:

$$\Delta S_M = \mu_0 \int_{H_1}^{H_2} \left(\frac{\partial m}{\partial T}\right)_{p,H} dH, \tag{1.73}$$

where the sign of the derivative determines the sign of ΔS_M. Note that all these thermodynamic equations can also be expressed in terms of the magnetization which is $M = \mu_0 m$. The negative ΔS_M is also known as direct MCE while the positive value is known as inverse MCE. Furthermore, the entropy of a solid can be calculated from the heat capacity using Eq. 1.68 by expressing the total entropy at zero and constant magnetic field as:

$$S(T)_{H=0} = \int_0^T \frac{C(T)_{p.H=0}}{T} dT + S_0 \; ; \; S(T)_{H\neq 0} = \int_0^T \frac{C(T)_{p.H}}{T} dT + S_{0,H}, \tag{1.74}$$

where S_0 and $S_{0,H}$ are the zero-temperature entropy term. It follows that the magnetocaloric magnitude is obtained as [73, 74]:

$$\Delta S_M(T,\Delta H) = \left[S_{H_2}(T) - S_{H_1}(T)\right]_T ;\ \Delta T_{ad}(T,\Delta H) = \left[T_{H_2}(S) - T_{H_1}(S)\right]_S. \qquad (1.75)$$

b) Figure of merit of the magnetocaloric effect

In order to find the best magnetic refrigerant materials with the best optimal properties, we need to define the figures of merit used for the comparison. As observed above, all three magnetocaloric quantities, ΔS_M, ΔT_{ad} and C_{pH} are significant for the performance of a given material. Several criteria have been suggested in the literature for a single number to quantify a material's potential as a refrigerant material. Wood and Potter [75] introduced a concept called refrigerant capacity (*RC*), which should be maximized in a magnetic refrigeration cycle:

$$RC = \Delta S_{cold}(T_{hot} - T_{cold}). \qquad (1.76)$$

Defined for a refrigeration cycle between a cold side (temperature T_{cold}) and a hot side (temperature T_{hot}); ΔT_{cold} is the entropy absorbed at the cold side per cycle which is then identified with the magnitude of the material's isothermal entropy change at temperature T_{cold}. However, in the magnetic refrigeration research community another quantity often called refrigerant capacity, RC' is defined as the area below ΔS curve [76]:

$$RC' = \int_{T_{cold}}^{T_{hot}} |\Delta S_M(T,H)| dT. \qquad (1.77)$$

This equation has no obvious interpretation in terms of cycle performance; in particular, it is not related to the amount of entropy a given regenerator can transport from cold to the hot side. It also has the somewhat troubling property of monotonously increasing for increasing temperature span $T_{hot} - T_{cold}$, giving a misleading impression that materials may be used in devices with arbitrary large temperature span [77].

Another quantity usually found in literature is the relative cooling power *RCP*, which is defined by:

$$RCP = |\Delta S_M^{max}|.\,\delta T_{FWHM}, \tag{1.78}$$

where δT_{FWHM} is the temperature taken at the full width at half maximum. This equation is equivalent to Eq. 1.76 (multiply by two) and its interpretation is subject to the same limitations. Further, Gschneider and Pecharsky [78], defined two relative cooling power corresponding to both the ΔS and ΔT_{ad} curves, respectively:

$$RCP_S = |\Delta S_M^{max}|.\,\delta T_{FWHM,S}\,;\; RCP_T = \Delta T_{ad}^{max}.\,\delta T_{FWHM,T}. \tag{1.79}$$

Note that δT_{FWHM} of the two curves, in general, can differ and the units of RCP_S and RC are the same (J/kg) while the units of RCP_T is K^2. Eq 1.79 recognizes the need to consider both ΔS_M and ΔT_{ad} when assessing the suitability of materials. The most state in the literature is RCP_S. However, it is unclear what combination of RCP_S and RCP_T would characterize a high-performance material. Engelbrecht and Bahl [79] showed explicitly that the *RCP* alone is not necessarily a good indicator of performance since different model materials with the same refrigerant capacity or (entropic) relative cooling power may perform very differently in device simulation.

Ongoing a step further Wood and Potter [75] suggested a more universal measure of refrigerant optimization that also takes into account the overall effort, not just the network required to produce the refrigeration. One such measure is the ratio of refrigerant capacity to the positive work done on the refrigerant during one cycle. This ratio is called the coefficient of refrigerant performance, *CRP*:

$$CRP = \frac{\Delta S.\,\Delta T}{\int_0^{\mu_0} M(T_{ord}.\,\mu_0 H')\,d(\mu_0 H')}\,, \tag{1.80}$$

where T_{ord} is the temperature of the magnetic phase transition, T_C or T_N. Guillou et al. [80] suggest the use of $\Delta T = \Delta T_{ad}$ criterion for MCE materials based on a continuous transition since the maximization approach $\Delta T = \delta T_{FWHM}$ criterion proposed by Wood and Potter [75] will also lead to an overestimation of material performance similar to *RC* and *RCP*. As suggested by Guillou et al. [80], the advantage of using $\Delta S_M^{max}.\,\Delta T_{ad}^{max}$ at the numerator of Eq. 1.80 is that it takes into account both the entropy change and adiabatic temperature change.

CHAPTER 2

RESEARCH TECHNIQUES

2.1. Sample Preparation

Polycrystalline samples of all investigated compounds were synthesized by arc – melting stoichiometric amounts of the constituent elements on a water–cooled copper hearth in a titanium–gettered high purity argon atmosphere (50 kPa below atmospheric pressure) see Figure 2.1. The polycrystalline samples studied in this thesis are $NdPd_2Al_2$ and RECuGa (RE = Nd, Dy and Ho). The constituent elements were weighed to a relative accuracy of ± 0.1 mg using a microbalance. All the constituent elements were bought from Alfa Aesar Company with purity in wt % as shown in Table 2.1. The ingots were turned over and remelted three to four times to ensure their good homogeneity. Weight losses after final melting were always less than 1% for all prepared compounds. The annealing process was not carried out since the prepared compounds were found to be single phase. Therefore, all the physical properties measurements were performed on as–cast samples.

The samples for electrical resistivity, magnetic susceptibility, magnetization and heat capacity were cut from the as–cast buttons using a Micracut 125 low speed precision cutter with a diamond blade of thickness 0.81 mm (Figure 2.3). The samples for magnetic susceptibility, magnetization and heat capacity were cut in cubical shape with typical dimensions $1\times1\times1$ mm^3, with an approximate weight of 10 to 30 mg. The samples for resistivity were cut in the form of a parallelepiped shape with typical dimensions $1\times1\times6$ mm^3. These parts of the samples were cut out of the center of the button to avoid the button surface and the top layer where the stress in the materials as evidenced by hairline cracks was sometimes found in some ingots. Pieces of the ingot were used for X-ray diffraction experiment and the flat part of the ingot was used for energy dispersive spectroscopy (EDS) experiment.

Table 2.1: Purity of the starting elements given in wt %.

Elements	Purity (wt %)
Nd	99.99
Dy	99.99
Ho	99.99
Pd	99.95
Al	99.999
Cu	99.995
Ga	99.9999

Figure 2.1: Arc melting chamber at the University of the Western Cape, Physics and Astrophysics Department where (a) A copper tray with 3 designated locations, (b) Arc furnace and generator.

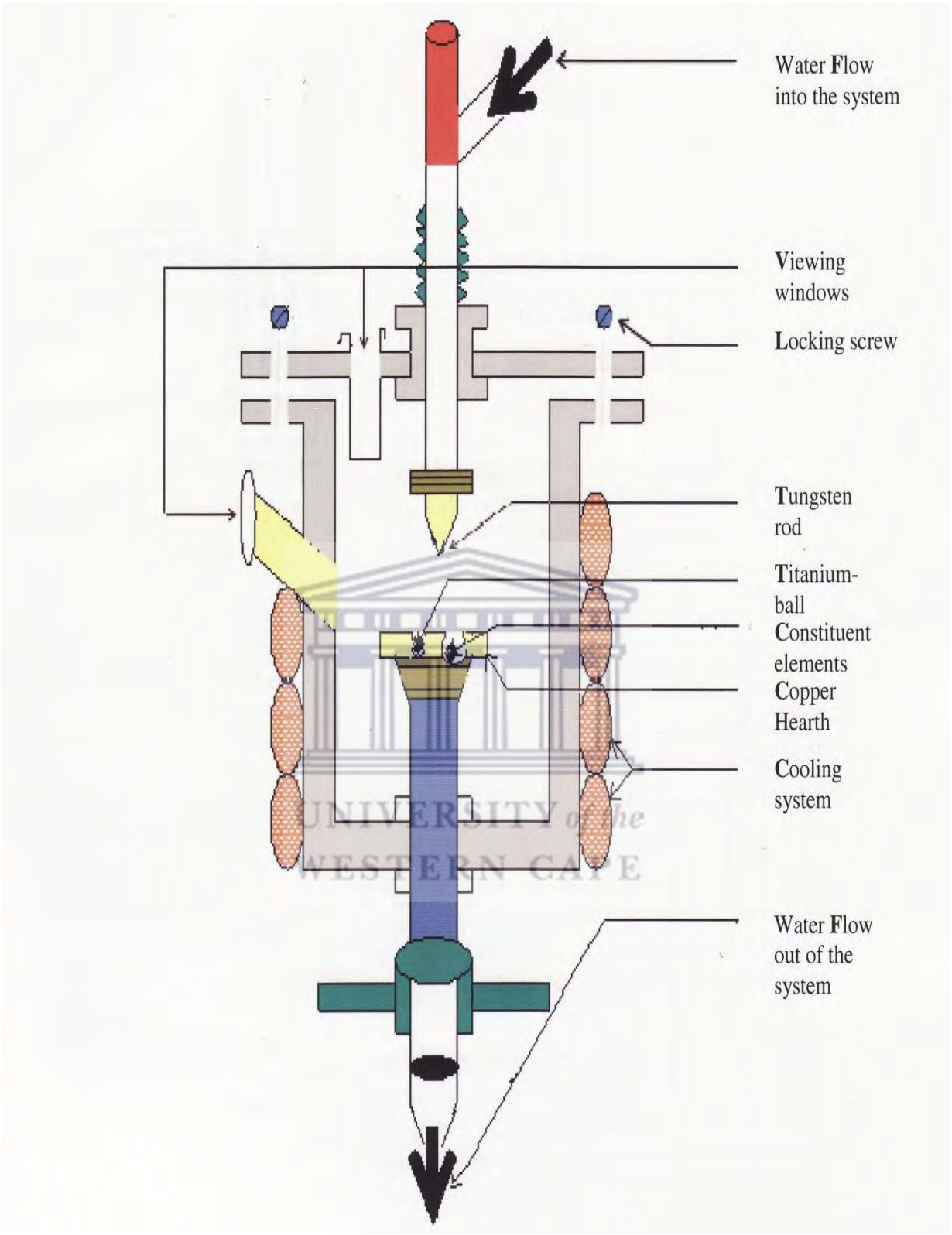

Figure 2.2: Schematic diagram of arc-furnace melting chamber.

Figure 2.3: Micracut 125 low speed cutter at the University of the Western Cape, Physics and Astrophysics Department.

2.1.1. Arc Melting

Arc melting is an effective method of preparing alloys by melting the constituent elements together. The elemental components are arc melted in a water-cooled copper tray evacuated in an arc melting chamber (Figure 2.1(b)). The schematic diagram of the arc – melting chamber is shown in Figure 2.2. These furnaces typically use a water-cooled copper crucible or hearth plate to limit contamination from refractory materials. The copper tray in the arc melting furnace has 3 designated locations (Figure 2.1(a)).

One location was filled with the accurately weighed stoichiometric amounts of the constituent elements, weighed to 3 g. The second location was filled with the ingot of titanium. With the constituents and the titanium all in place, the arc melting chamber was subjected to a vacuum for an hour and then flushed 7 times with high – purity argon gas. During the process of melting,

the titanium was first melted in order to eliminate all trace of impurities in the chamber such as oxygen. The mass losses after final melting were estimated from the initial total mass of the constituent elements and the final mass of the ingot and this was always less than 1% as mentioned above.

2.2. Sample characterization

Sample characterization generally involves the crystal structure analysis using a BRUCKER D8 – Advance Diffractometer as well as the elemental composition of each compounds using EDS.

2.2.1. X-ray Diffraction

In this study, we have XRD to investigate the crystal structures of all the prepared samples using a Bruker D8 Advance diffractometer with a Cu K_α radiation (λ= 1.540598 Å) (Figure 2.4(a)). Part of the prepared ingot was finely ground in an agate mortar and deposited on a sample holder (a rectangular glass slide). The sample holder was then placed at the center of the Diffractometer stage as shown in Figure 2.4(b).

(a) (b)

Figure 2.4: (a) Bruker D8 advance powder diffractometer, (b) Diffractometer stage, at iThemba LABS.

A vacuum atmosphere was initiated in order to hold the sample in place. This was done by tightly closing the doors of the Diffractometer and then turning on a vacuum pump. The XRD measurements were completed at room temperature. The data set was collected by means of a computer with software from Bruker called EVA. The voltage was set to 40 kV, the current set to 30 mA and the diffraction patterns were measured in the range of $12^o \leq 2\theta \leq 90^o$ in steps of 0.034^o. The obtained diffraction patterns were qualitatively analyzed using the Pawley Cell and Intensity Least Square (CAILS) fit, while the quantitative analysis was performed with a full – profile Reitveld refinement method, both from TOPAS ACADEMIC programme. The analysis of the diffraction pattern reveals no evidence of parasitic phases or unreacted elements of all prepared samples.

2.3.1.1. XRD analysis: CAILS and Reitveld refinement methods

The information about the lattice parameters of the crystal structure is provided by the CAILS-Pawley refinement method. In this method of refinement, only the peak width parameters, cell parameters, and integrated intensities are refined. CAILS refinement is independent of the atomic position parameters (or structural model) and only depends on the space group symmetry. Moreover, in the CAILS method, the intensities of all diffraction peaks vary independently.

The Rietveld refinement method similarly depends on the space group symmetry, however, is different from the CAILS method in the sense that not only the peaks parameters, cell parameters and integrated intensities are refined, but atomic coordinates, the site occupancy, the isotropic displacement parameters as well as the interatomic distances are also refined.

2.3.1.2. Criteria of fit

The quality of fit is defined by the refined agreement indices of the analysis. These are the residuals: the profile R-factor (R_p an indication of the goodness of fit: GOF), weighted profile R - factor (R_{wp}, a measure of the GOF calculated point by point and weighted by the standard deviation of the data), expected R-factor (R_{exp}, an expected value of R_{wp}), intensity R-factor (or Bragg - factor) (R_B), The GOF or χ^2 based on statistic and the Durbin-Watson factor (DW, a

measure of the quality of the fits model). These agreement indices are defined as follows [81 - 83]:

$$R_p = \sqrt{\frac{\sum|Y_{o,m} - Y_{c,m}|}{\sum Y_{o,m}}}\ ; \tag{2.1}$$

$$R_{wp} = \sqrt{\frac{\sum w_m\left(Y_{o,m} - Y_{c,m}\right)^2}{\sum w_m {Y_{o,m}}^2}}; \tag{2.2}$$

$$R_{exp} = \sqrt{\frac{\sum M - P}{\sum w_m {Y_{o,m}}^2}}; \tag{2.3}$$

$$GOF = \chi^2 = \frac{R_{wp}}{R_{exp}} = \sqrt{\frac{\sum w_m\left(Y_{o,m} - Y_{c,m}\right)^2}{\sum M - P}}; \tag{2.4}$$

$$R_B = \frac{\sum|I_{\text{"o"},k} - I_{c,k}|}{\sum I_{\text{"o"},k}}\ ; \tag{2.5}$$

$$DW = \frac{\sum_{m=2}^{M}(\Delta Y_m - \Delta Y_{m-1})}{\sum_{m=1}^{M}(\Delta Y_m)^2}; \qquad \Delta Y_m = Y_{o,m} - Y_{c,m}. \tag{2.6}$$

$Y_{o,m}$ and $Y_{c,m}$ are the observed and calculated data, respectively at data point m, M is the number of data points, P the number of parameters, w_m the weighting given to data point m which for counting statistics is given by $w_m = 1/\sigma\left(Y_{o,m}\right)^2$, where $\sigma\left(Y_{o,m}\right)$ is the error in $Y_{o,m}$, and $I_{\text{"o"},k}$ and $I_{c,k}$ the "observed" and calculated intensities of the k^{th} reflection.

2.2.2. Scanning electron microscopy

The elemental composition of all prepared samples was performed using the Energy Dispersive Spectroscopy (EDS). This analysis was conducted using a Field-Emission Scanning Electron Microscopy (FESEM) (Figure 2.5). The procedure followed involved mounting the samples on an aluminium sample holder, which had a sticky-tape on top to enable the sample to remain stable; the sample was then inserted into the FESEM in order to initiate the analysis.

The X-ray emission was acquired at each point, thus providing a chemical map that delivered chemical information in a single output. This procedure gave the results of the elemental composition in each sample together with their relative proportions and their atomic percentages.

Figure 2.5: Photograph of Field-Emission Scanning Electron Microscope (FESEM), Electron Microscope Unit (EMU), Department of Physics & Astronomy, UWC.

2.3. Physical properties measurements

All physical properties (electrical resistivity, magnetic susceptibility, magnetization and heat capacity) studied and reported in this thesis were measured using Physical Properties Measurement System (PPMS) and the Magnetic Properties Measurement System (MPMS) equipped with a vibrating sample magnetometer (VSM) both from Quantum Design, San Diego (USA) (Figures 2.6, 2.10).

2.3.1. Electrical resistivity measurements procedure

Electrical resistivity measurements were performed by a standard four point probe method in the temperature range 1.9 − 300 K in step size of 0.5 K. The standard resistivity puck is shown in Figure 2.7 and Figure 2.8. The resistivity option performs a 4-point resistance measurement on up to 3 channels at a time. The standard resistivity puck includes pre-mapped pads for + and – current and voltage for channels 1 – 3. The base is conducting, so an insulating layer of Kapton tape was inserted since it is necessary for samples with conductive backsides.

Figure 2.6: A commercial device Physical Property Measurement System (PPMS) by Quantum Design at the University of Johannesburg Physics Department.

The sample was attached to the taped surface using a general electric (GE) varnish glue. This glue was chosen because of its excellent adhesive properties below helium temperature and it has great electrical insulating and thermal conductivity properties. The sample was positioned close to the center of the puck, then the standard four-Gold wires of thickness 0.05 mm were used for contact with the sample using an electrically conductive silver paste and attached to the bridge channels by a method of soldering. After each connection, the contacts were verified using a multimeter to see if each sample had made good contacts. Each sample was associated with just a single user bridge channel.

The sample puck was loaded into the PPMS. The typical excitation current of 4500 μA was used for Helium-4 (^{4}He) direct current resistivity measurements under the frequency of 17 Hz. The potential difference between the gold wires fixed on the sample was used to automatically

measure the resistance and consequently the resistivity ($\rho(T)$) of the sample. All $\rho(T)$ measurements were done in the temperature range of 300 K down to 100 K at the cooling rate of 1.5 K/min, from 99 K to 11 K at the rate of 1 K/min in 90 steps and from 10 K to 1.8 K at 0.5 K/min in 41 steps.

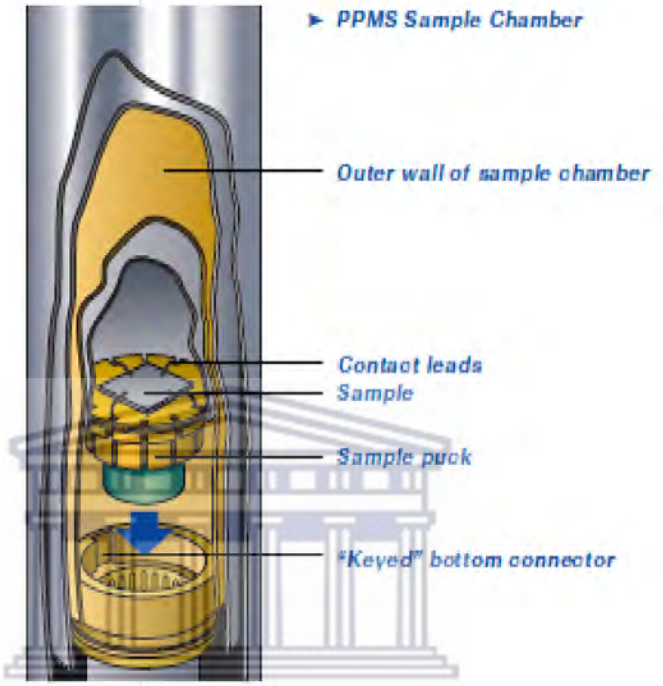

Figure 2.7: Cross-section of the sample puck inside the PPMS sample chamber (PPMS user manual, Quantum design, San Diego).

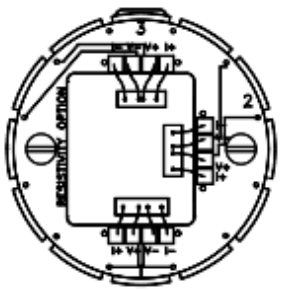

Figure 2.8: Schematic diagram of the dc resistivity sample puck with three samples mounted for four-wire resistance measurements.

2.3.2. Specific heat

Specific heat measurements were carried out using a PPMS. This instrument measures the heat capacity at constant pressure C_p using a relaxation method. The measurements were conducted in the temperature range of 1.8 K - 400 K and changes in sample volume were negligible according to the change rate of the measured temperature. For specific heat measurements, a platform heater and platform thermometer are attached to the bottom side of the sample platform (See Figure 2.9) where the wires provide the electrical connection to the platform heater and platform thermometer and also provide the thermal connection and structural support for the platform. The sample platform has certain limits of sample weight of approximately 100 mg or less that it can accommodate. For compounds with large specific heat at low temperatures, e.g. materials with magnetic phase transitions, smaller samples of approximately 1 mg were used to reduce the measurement time. Good thermal contacts were accomplished by finely polishing the sample and shaping it according to the dimensions of the platform.

The sample is mounted to the platform by using a thin layer of Apizeon grease, which provides the required thermal contact to the platform even at low temperatures. Calorimeter puck is placed into a high vacuum PPMS cryostat, surrounded with magnets for application of an external magnetic field. The contribution that the platform and grease make to the total heat capacity was determined in an independently conducted experiment before the sample was mounted, then subtracted from total specific heat obtained when the sample was mounted, this was done to obtain the sample specific heat. A heater was used to provide a known amount of heat for a fixed time *t* at constant power, followed by the process of cooling for the same period. The data acquired after every measurement cycle fits the whole temperature reaction of the sample platform to the two τ model from Quantum design to determine the heat capacity. This model accounts for both the thermal relaxation of the sample platform and the sample itself [84]. The PPMS picks the result of the model from a better fit. Lastly, the software of PPMS computes the heat capacity in the unit of m**J**/mole.K by taking the specific heat of the sample then multiply it by the molar mass of the sample then divide by the mass of the sample.

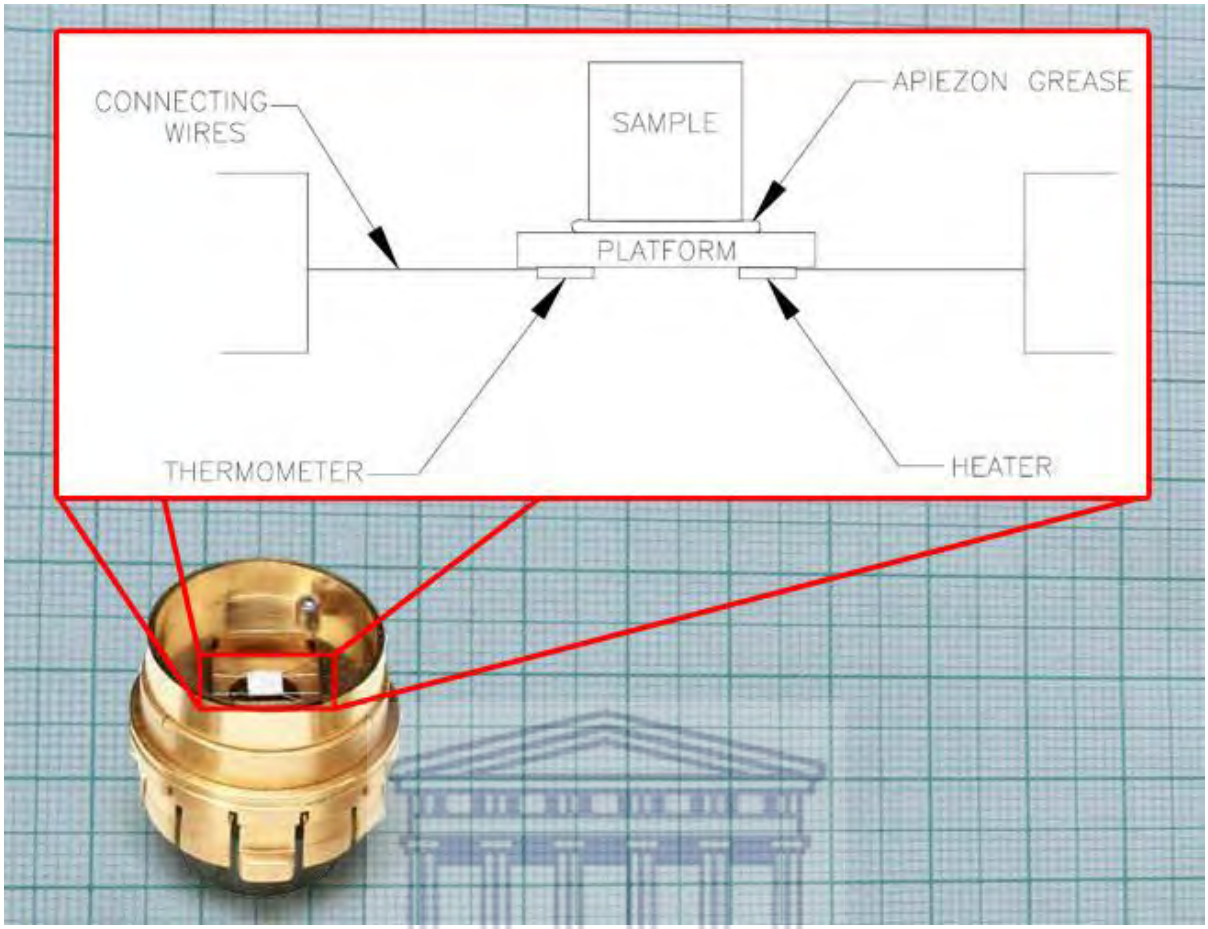

Figure 2.9: Calorimeter puck with schematic thermal connections to sample and sample platform in PPMS heat option.

2.4. Measurements of magnetic properties

Magnetic susceptibility and magnetization measurements were performed by means of a Superconducting Quantum Interference Device (SQUID) magnetometer in a Magnetic Property Measurement System (MPMS) (see Figure 2.10). This equipment has three main modes of measurements, namely the reciprocating sample option (RSO), directive current (DC) and alternative current (AC) measurements methods. The magnetic properties studies in this thesis were performed using the DC measurement method. In DC option, the magnetometer is very accurate and can easily detect a high magnetic moment of paramagnetic, diamagnetic, ferromagnetic and antiferromagnetic magnetic materials.

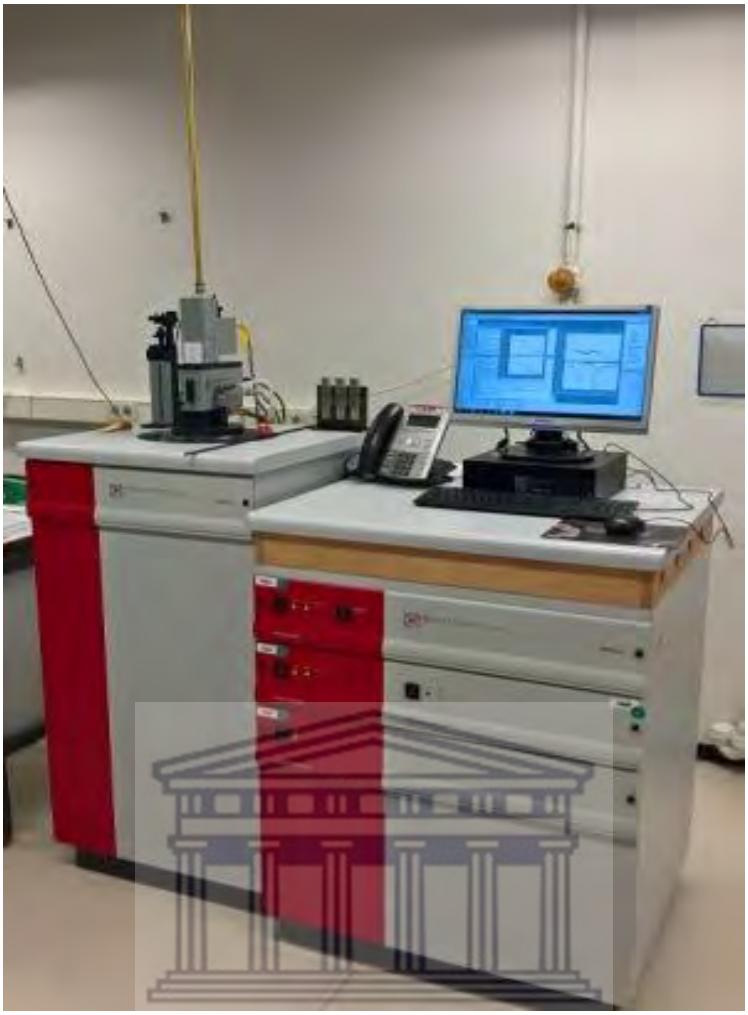

Figure 2.10: A commercial device Magnetic Property Measurement System (MPMS).

2.4.1. Magnetic susceptibility and magnetization measurements

The measurements were conducted on a single piece of a sample with dimensions 1 × 1 × 1 mm^3 (~15 mg mass) in the temperature range of 1.7 − 400 K in fields up to 7 T. An elongated piece of each polycrystalline sample was cut and used for this experiment. The choice of an elongated shape was to minimize the demagnetizing fields. The sample was inserted into a little plastic pack, which was at that point embedded into a sample holder. The sample holder used was a plastic straw (Figure 2.11), since it has less mass and less diamagnetic background signal. For each measurement, the plastic bag signal was subtracted using the known mass in order to determine the correct results. The overall measurements were performed using a stepper motor, which was used to move the sample through the pick-up coils. The superconducting quantum interference device (SQUID) pick-up coil produces a current corresponding to the gradient of

the external field, instead of the field itself. The magnetic moment of the sample couples inductively with the coils during the sample movement, and produces a current variation in the superconducting circuit, which is proportional to the sum of the fluxes across the coils. The same current is then coupled to the SQUID loop, and the final voltage output produced is recorded using a lock-in technique. The output voltage, as opposed to the position curve, was measured as an average of different scans of the sample position to reduce the noise and to extract the value of the magnetic moment.

Measurements of the magnetic moment were carried out as a function of temperature (magnetic susceptibility) under field-cooled (FC) conditions on a direct current (DC) option with a static magnetic field (≤ 1000 Oe). Magnetization isotherm measurements (that is, measuring the magnetic moment as a function of the magnetic field) were performed by fixing the sample temperatures and scanning the applied field from 0 up to 7 T.

2.4.2. THE SQUID magnetometry

Figure 2.11 shows a schematic diagram of a SQUID which is the most sensitive device available for measuring magnetic fields. Although the SQUID in the MPMS is the source of the instrument's remarkable sensitivity, it does not directly detect the magnetic field from the sample. Instead, the sample moves through a system of superconducting detection coils, which are connected to the SQUID with superconducting wires, allowing the current from the detection coils to couple inductively to the SQUID sensor. When properly configured, the SQUID electronics produce an output voltage that is strictly proportional to the current flowing in the SQUID input coil. Hence, the thin-film SQUID device, which is located approximately 11 cm below the magnet inside a superconducting shield, essentially functions as an extremely sensitive current-to-voltage convertor.

Measurements performed in the MPMS are obtained by moving a sample through the superconducting detection coils, which are located outside the sample chamber and at the center of the magnet. As the sample moves through the coils, the magnetic moment of the sample induces an electric current in the detection coils. Because the detection coils, the connecting wires, and the SQUID input coil form a closed superconducting loop, any change of magnetic flux in the detection coils produces a change in the persistent current in the detection circuit, which is proportional to the change in the magnetic flux. Since the SQUID

functions as a highly linear current-to-voltage convertor, the variations in the current in the detection coils produce corresponding variations in the SQUID output voltage that are proportional to the magnetic moment of the sample. In a fully calibrated system, measurements of the voltage variations from the SQUID, detects as a sample is moved through the detection coils provide a highly accurate measurement of the sample's magnetic moment. The system can be accurately calibrated using a small piece of material having a known mass and magnetic susceptibility.

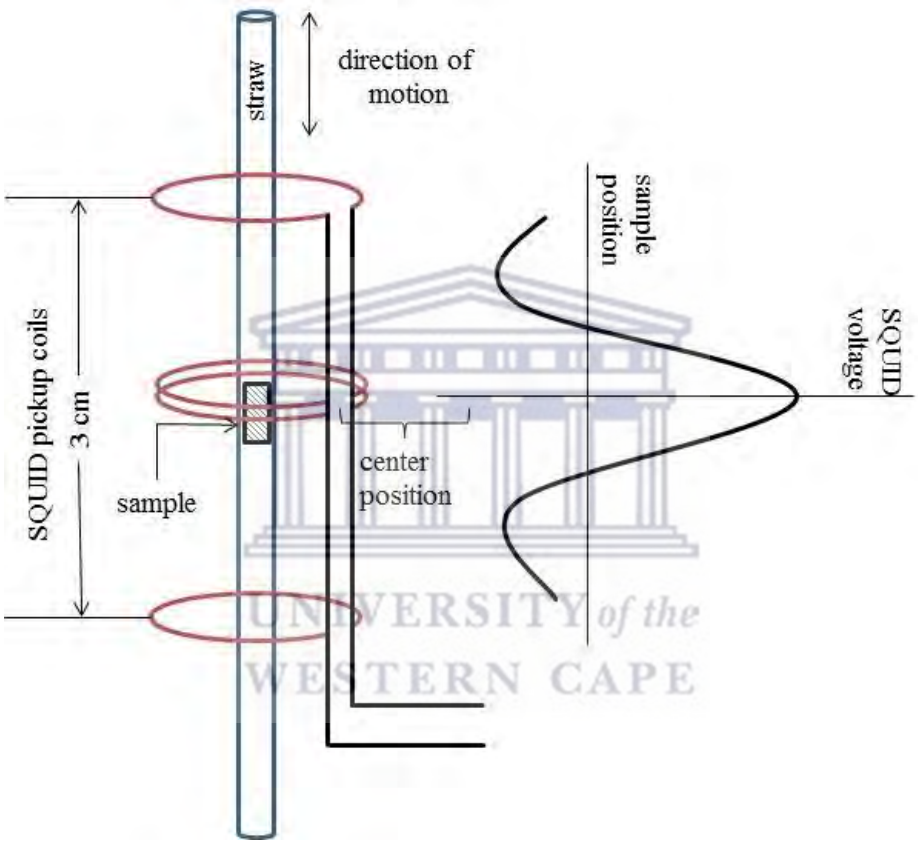

Figure 2.11: Schematic representation of a SQUID which is found in the MPMS with a plastic straw.

CHAPTER 3

TRANSPORT, MAGNETIC AND MAGNETOCALORIC PROPERTIES OF $NdPd_2Al_2$ COMPOUND

3.1. Introduction

Renewed interest has been devoted to the study of physical properties of the ternary intermetallic compounds RET_2X_2 with RE = rare-earth metals, T = 3d/4d/5d electron transition metals and X = p - block elements. The crystal structure of this family of compounds has been reviewed by Rogl [85]. Most of these compounds crystallize in the ordered $ThCr_2Si_2$ - type structure with space group *I4/mmm*. However, $CePd_2Al_2$, which is a homologue compound of $NdPd_2Al_2$ in this study is an exception. Several authors [86 - 88] report that $CePd_2Al_2$ crystallizes in the tetragonal $CaBe_2Ge_2$ - type structure with space group *P4/nmm*. On the other hand, it was also reported that $REPd_2X_2$ (RE = Ce or La, X = Al or Ga) compounds crystallize in the $CaBe_2Ge_2$ type noncentrosymmetric tetragonal structure, and undergo a structural distortion to orthorhombic (X = Al) [89, 90] or triclinic (X = Ga) [89, 91] structures at low temperatures. Some controversy exists on the structure type. Compounds with the $ThCr_2Si_2$-type structure are abundant due to their robust structure and the interesting physical properties that result from the ability of this structure to adopt different elements with various atomic sizes [92]. Compounds with the $ThCr_2Si_2$ - and $CaBe_2Ge_2$ - types of structures share similar structural features. Both structures are described by tetragonal unit cells with comparable lattice parameters (~4 Å x 10 Å) [93]. The structure type in RET_2X_2 compounds is influenced by the atomic radii and the synthesis conditions of the compounds. The $CaBe_2Ge_2$ - type is more prone to form when a sample is quenched at high temperatures [94]. The $CaBe_2Ge_2$ - type consists of layers of edge-sharing $BeGe_4$ and $GeBe_4$ tetrahedra with alternating layers of isolated Ca atoms in a 1:1:1 ratio. In contrast, the $ThCr_2Si_2$ - type structure consists of $CrSi_4$ edge-sharing tetrahedra with alternating layers of isolated Th atoms in a 1:1 ratio. Band structure calculations have shown that the $ThCr_2Si_2$ - type is more stable at room temperature due to its less dispersed filled band and its lower Fermi level [95]. A Monte Carlo simulation study showed that at high temperatures, entropic contributions become more important and thus can favour the $CaBe_2Ge_2$ - type [95].

The intense research on RET_2X_2 compounds during the past few decades is due to the rich variety of different ground state properties. This includes Kondo lattice behaviour, heavy fermion with magnetic or superconducting ground states, non - Fermi liquid ground states, mixed-valence ground states as well as various kinds of magnetic structures [96 − 103].

The study of magnetic and transport properties of $CePd_2Al_2$ single crystal indicates an antiferromagnetic (AFM) phase transition at the Néel temperature T_N = 2.7 K [86] or 2.5 K [92] as well as first-order structural phase transition from tetragonal to orthorhombic structure around 13 K [90]. Klicpera *et al.* [91] reported the superconductivity in $CePd_2Al_{2-x}Ga_x$ alloys through measurements of electrical resistivity and heat capacity. Their results reveal unconventional superconductivity in these alloys. Furthermore, the results of the electronic heat capacity below the superconducting transition temperature indicate an axial state with line nodes in the superconducting gap structure. Inelastic neutron scattering experiments disclosed three non-dispersive magnetic excitations in the paramagnetic state of $CePd_2Al_2$, while only two crystal field excitations are expected from the splitting of ground state J = 5/2 of the Ce^{3+} ion in a tetragonal/orthorhombic point symmetry [89]. In the case of $CePd_2Ga_2$, inelastic neutron scattering experiments, reveal the magnetic structure composed of two components [89]. On the other hand, the specific heat studies on the heavy–fermion compound $CePd_2Si_2$ single crystal in magnetic field up to 16 T and in the temperature range 1.4 – 16 K, indicates an AFM transition at $T_N \sim 9.3$ K in zero fields [104]. This transition is found to shift to lower temperatures when a magnetic field is applied along the a – axis, while a field applied parallel to the c – axis does not affect the transition. Superconductivity in $LaPd_2Al_{2-x}Ga_x$ compounds was reported by means of electrical resistivity and specific heat measurements [87]. This study reveals a concentration development of the superconducting properties and the data deviate considerably from the Barden – Cooper – Schrieffer theory and corroborates with the unconventional superconductivity [87]. Specific heat study on $CeNi_2Sn_2$ compound reveals an AFM magnetic phase transition at T_N = 2 K [105]. Furthermore, a magnetic contribution of the specific heat for $CeNi_2Sn_2$ was observed at a temperature slightly above T_N. This was attributed as a short-range order due to the magnetic frustration inferred from the particular magnetic structure with the propagation vector $(½, ½, 0)$. Electrical resistivity and specific heat show a clear Kondo behaviour above T_N [105]. In the case of $CePd_2Sn_2$, specific heat result indicates AFM phase transition at 0.5 K.

Beside intense investigations of the physical properties of the RET_2X_2 compounds, to the best of our knowledge, no effort was devoted to the studies of magnetocaloric properties of this family of compounds. Research for new magnetic materials displaying larger MCE, which then can be operated in lower fields of about 2 T that can be generated by permanent magnets, is very significant. Refrigeration of this nature is of particular interest because of the potential impact on energy savings and environmental concerns. This magnetic refrigeration is at present almost exclusively conducted on superparamagnetic materials and rare-earth compounds. In general, a good magnetic refrigerant material requires large magnetocaloric effect (MCE), high relative cooling power *RCP*, a high refrigerant capacity (*RC*), a low heat capacity $C_p(T)$, since a high $C_p(T)$ increases the thermal load and more energy is required to heat the sample itself and causes a loss in entropy, that is, for a given $-\Delta S_M$ and ΔT_{ad} will be lower, low cost and harmless materials, etc. The search for new materials from rare-earth intermetallic compounds for the application in magnetic refrigeration is one of the crucial topics in most modern material science research [106, 107]. In the present work, the magnetocaloric effect (MCE) in $NdPd_2Al_2$ was studied by means of isothermal magnetization and heat capacity measurements. Electrical resistivity and magnetic susceptibility results are also reported for this compound.

3.2. Results and Discussion

3.2.1. X-ray diffraction

The X-ray diffraction pattern recorded for the $NdPd_2Al_2$ compound is displayed in Figure 3.1, together with the results of the CAILS – Pawley refinement. In the refinement process, the assumed space group was *P4/nmm* (No. 129) of the $CaBe_2Ge_2$ - type structure. Negligible impurity peaks (≤ 10% of the major peak intensity) were detected in the XRD pattern as indicated by the arrows in Figure 3.1. The obtained lattice parameters (*a* and *c*) and the unit cell volume (*V*) are shown in Table 3.1. The obtained unit cell volume of $NdPd_2Al_2$ compound is smaller than the value of 190.88(10) $Å^3$ obtained for $CePd_2Al_2$ compound [88] which confirms the lanthanide contraction between Ce and Nd. The resulting refined agreement indices for the $NdPd_2Al_2$ are shown in Table 3.2. It should be noted, that although the quality of CAILS refinement fits for $NdPd_2Al_2$ is reasonably good (Figure 3.1), the observed values of GOF and the *R* – factors are relatively high. On the other hand, the value of *DW* is less than the ideal value of 2 [82], which indicates that the quality of the fit is correct.

Table 3.1: Room temperature lattice parameters and the unit cell volume of $NdPd_2Al_2$ in the CAILS – Pawley refinement method.

Compound	Parameters	CAILS - Pawley
$NdPd_2Al_2$	a [Å]	4.3836(2)
	c [Å]	9.8391(2)
	V [Å^3]	189.07(2)

Table 3.2: Values of the residual factors (all the symbols have their usual meaning) in the CAILS – Pawley refinement method performed for $NdPd_2Al_2$

Compound	Parameters	CAILS - Pawley
$NdPd_2Al_2$	R_{wp}[%]	24.713
	R_{exp}[%]	4.066
	R_p[%]	18.634
	χ^2	6.078
	DW	0.524

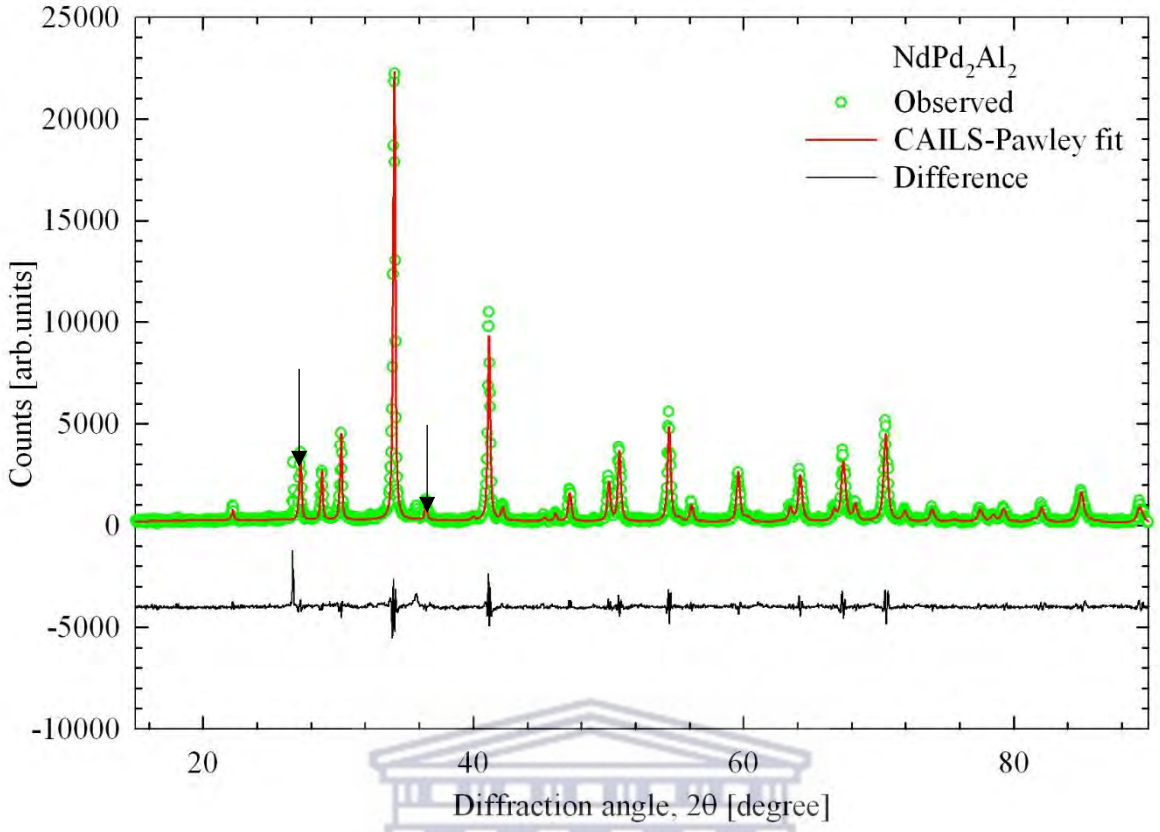

Figure 3.1: CAILS - Pawley (cell and intensity least squares) analyzed diffraction pattern for $NdPd_2Al_2$ compound. The observed data are shown by green symbols and the solid red line through the data represents the result of the CAILS - Pawley refinement. The lower black curve is the difference curve for the experimental data and the calculated curve. The arrows indicate the impurities peaks.

3.2.2. Electrical resistivity

The temperature variation of the electrical resistivity, $\rho(T)$ is shown in Figure 3.2. $\rho(T)$ shows a sudden drop at low temperature around the magnetic phase temperature at T_N = 3 K as indicated by the arrow in the inset of Figure 3.2. This drop results from the decrease of the scattering of the conduction electrons in the ordering region. At high temperatures, $\rho(T)$ increases with temperature and exhibits a downward curvature that originates from the crystal - electric field (CEF) or the $s - d$ interband scattering of the conduction electrons. Therefore, the behaviour of $\rho(T)$ at high temperatures originate from the electron-phonon scattering described by the Bloch Grüneissen relation (Eq. 1.19), the interband scattering described by the Mott's term $(-KT^3)$ and the CEF. No attempt was made to fit $\rho(T)$ taking an account of the three scattering processes.

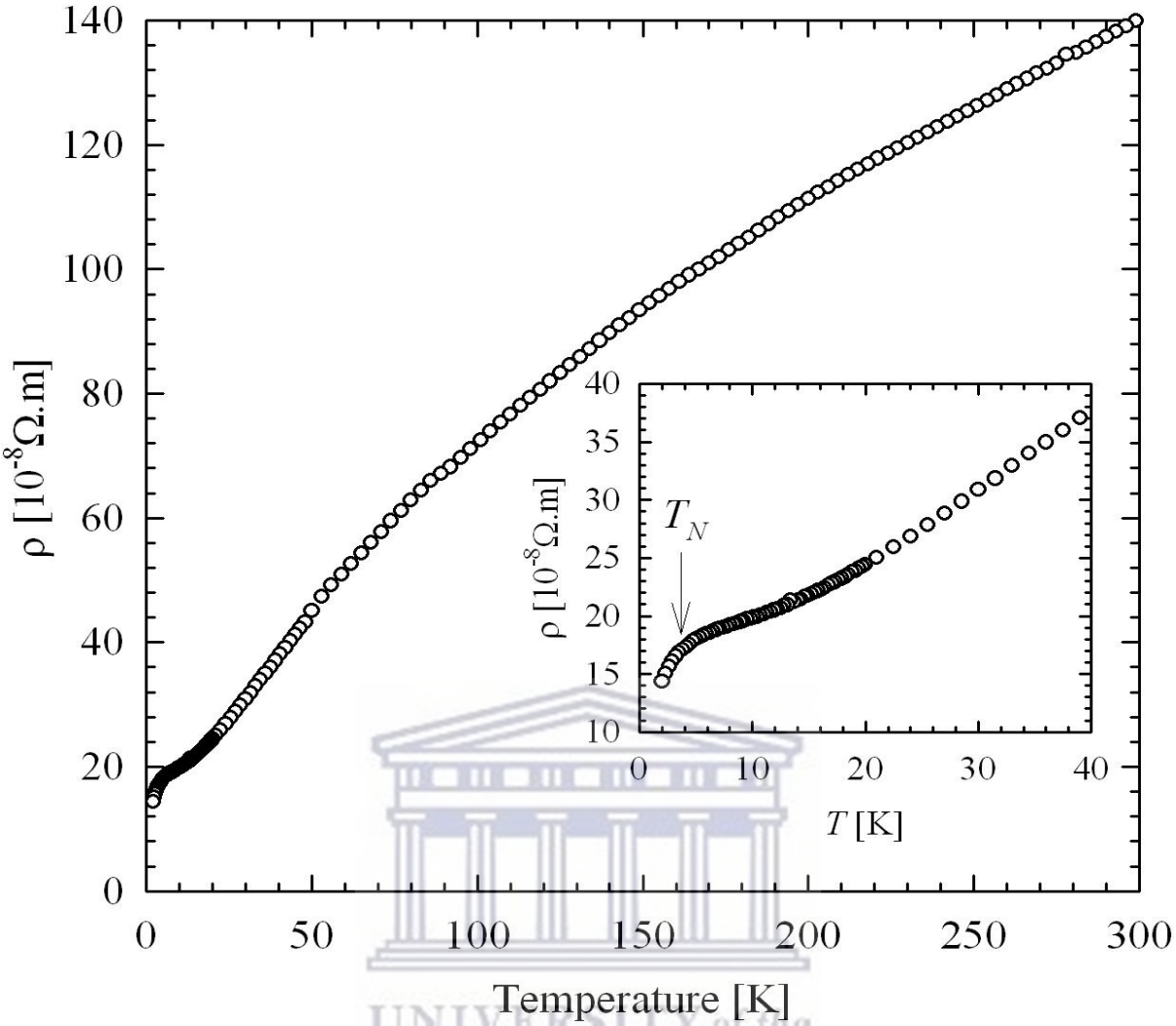

Figure 3.2: Temperature variation of the electrical resistivity, $\rho(T)$, of the $NdPd_2Al_2$ compound. The insert illustrated the low-temperature, $\rho(T)$ data, with the arrow indicating the sudden drop at the magnetic phase transition temperature, T_N.

3.3. Magnetic Properties

3.3.1. Magnetic susceptibility and Magnetization

The temperature variation of the magnetic susceptibility,$\chi(T)$, measured for $NdPd_2Al_2$ in an applied magnetic field of 0.1 T and the temperature range 1.71 - 400 K is shown in Figure 3.3. Above 10 K, the$\chi(T)$data follows the modified Curie - Weiss (MCW) relationship:

$$\chi(T) = \chi_0 + \frac{N_A \mu_{eff}^2}{3k_B(T - \theta_p)}, \tag{3.1}$$

where μ_{eff} is the effective magnetic moment, θ_p is the Weiss temperature and the other symbols have their usual meaning. The LSQ fits of the MCW relationship to the experimental data yielded μ_{eff} = 3.65(2) μ_B and θ_p = 0.52(7) K. The observed μ_{eff} value is close to that expected for a free Nd^{3+} - ion ($g\sqrt{J(J+1)} = 3.62\,\mu_B$). Deviation of the MCW at low temperatures originates from magnetocrystalline anisotropy. As can be inferred to the top inset of Figure 3.3, the low temperatures of $\chi(T)$ exhibits a maximum at T_N = 3.2 K (as indicated by an arrow), which is associated with a putative AFM phase transition. This result corroborates the sudden drop observed in the low temperature of $\rho(T)$ as well as the maximum observed in the low temperatures $C_p(T)$ data (see section 3.3.2). To further examine the nature of the magnetic phase transition, it is worthwhile noting that the magnetic susceptibility decreases only slightly in the ordering region and gives the ratio $\epsilon = \chi(1.72K)/\chi(T_N)$ that is about 0.85 for $NdPd_2Al_2$ compound. This feature contrasts with the behaviour expected for collinear AFM orderings (ϵ = 2/3) [108, 109], and might give rise to speculation about a possible noncollinear AFM spin arrangement in this compound, as reported recently for the binary compound $GdPd_3$ [110]. Further measurements, such as neutron diffraction experiments, are required to verify such conjecture and determine the actual magnetic structure in this compound.

The bottom inset of Figure 3.3 shows the field variations of the magnetization, $M(H)$ of the $NdPd_2Al_2$ compound measured at 1.72 K. $M(H)$ exhibits three metamagnetic - like transitions at H_{met} = 0.04, 0.4 and 1.8 T as indicated by arrows in the bottom inset of Figure 3.3. These values of H_{met} were estimated at the maximum of the derivative of $M(H)$, dM/dH curve (right axis). Above the field of 1.8 T, $M(H)$ deviates from linearity and becomes strongly curvilinear, showing a tendency toward saturation in the strongest field applied. At the highest measured field of 7 T, the magnetization of this compound attains a value of 1.90 μ_B. This value is smaller than the theoretical value for the ordered magnetic moment of the trivalent Nd - ion of gJ = 2.72 μ_B. This reduction of the moment value results mostly from CEF and magnetic anisotropy.

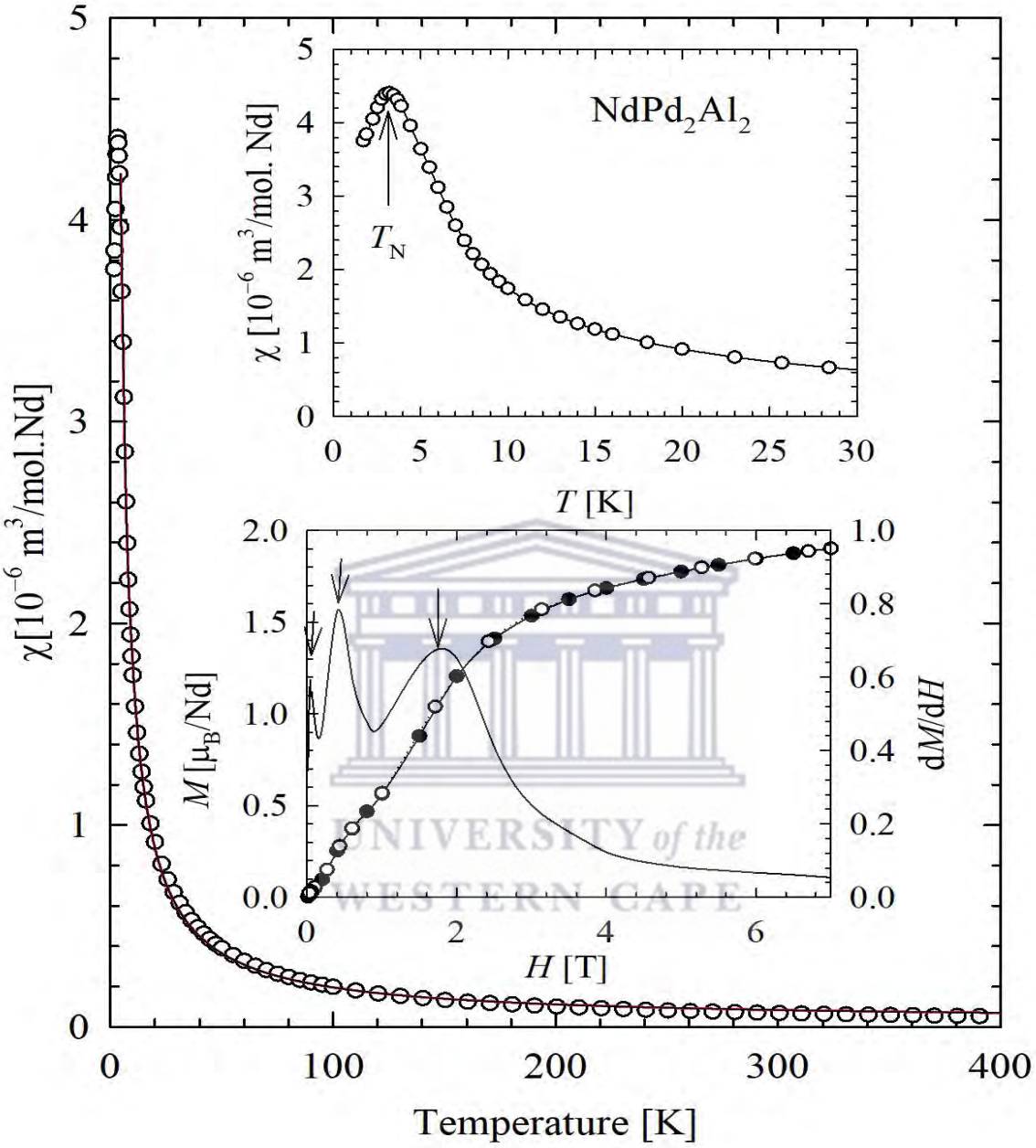

Figure 3.3: Temperature variation of the inverse magnetic susceptibility, $\chi(T)$of $NdPd_2Al_2$ compound measured in the temperature range of 1.71 - 400 K in a field of 0.1 T. The solid red line represents the LSQ fits of the modified Curie - Weiss relationship (Eq. 3.1) to the measured data above 10 K. The top inset illustrated the low temperature, $\chi(T)$ data with the arrow indicating the magnetic phase transition temperature, T_N. The bottom inset displays the field dependence of magnetization, $M(H)$, measured at a temperature of 1.7 K in increasing (close symbols) and decreasing (open symbols) fields. The arrows indicated the metamagnetic phase transitions at H_{met} = 0.04, 0.4 and 1.8 T.

3.3.2. Heat capacity, $C_p(T)$

Figure 3.4 shows the low-temperature variations of the heat capacity, $C_p(T)$ of the $NdPd_2Al_2$ compound. As can be inferred from this figure, $C_p(T)$ data exhibits a peak at T_N = 3.1 K, associated with a putative AFM phase transition that is also observed in $\rho(T)$ and $\chi(T)$ results. Below T_N, $C_p(T)$ decreases almost linearly with decrease temperature. This behaviour hints to the absence of an energy gap in the spin-wave dispersion.

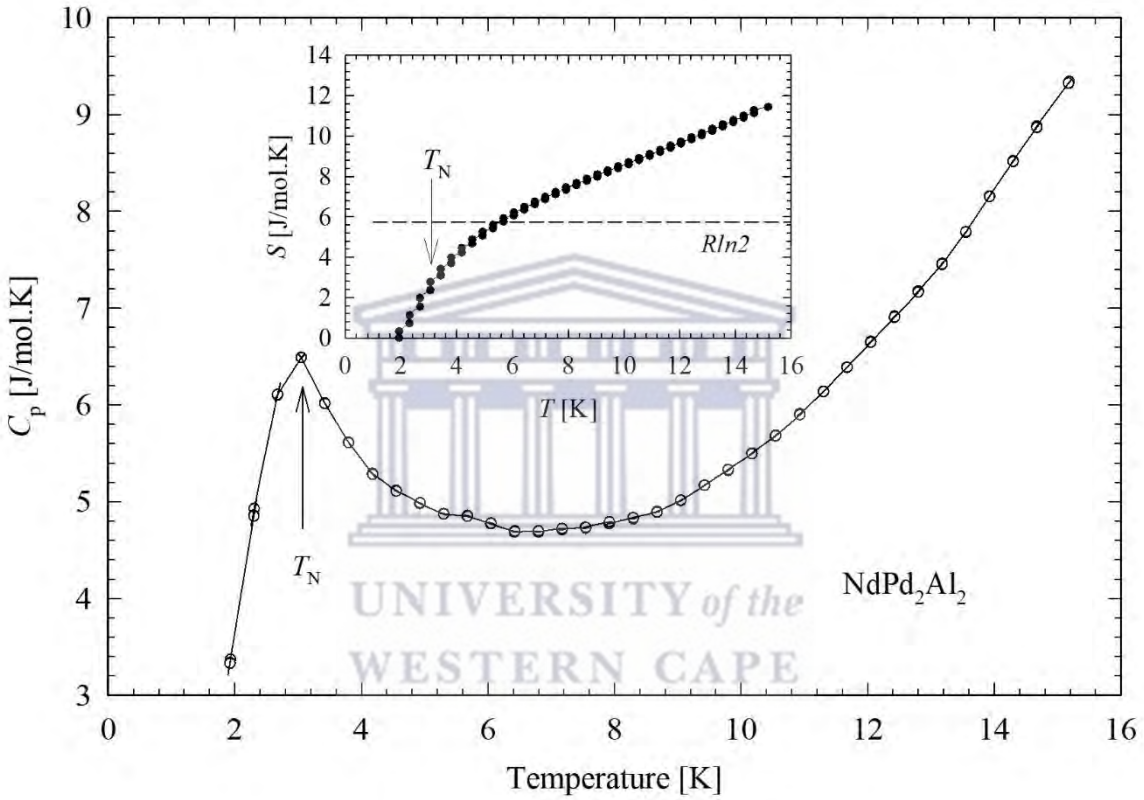

Figure 3.4: The low-temperature variation of the heat capacity, $C_p(T)$ of $NdPd_2Al_2$ compound measured in the temperature range of 1.9 - 15 K in a zero fields. The arrow indicates the magnetic phase transition temperature, T_N. The inset displays the plot of the magnetic entropy, $S(T)$ with the arrow indicating the position of the magnetic phase transition temperature, T_N. The horizontal dashed line represents *R.ln2* appropriate for a well-isolated doublet.

The magnetic entropy, $S(T)$ of $NdPd_2Al_2$, was calculated by integrating $C_p\ (T)/T$ and the results are presented in the inset of Figure 3.4. It is noted that, the entropy release at T_N amount to 2.77 J/mol.K, which corresponds to ca. 48% of the value of *R.ln2* expected for a well-isolated doublet ground state of Nd^{3+} ions. This value of *R.ln2* is reached at 5.67 K well above T_N. A

similar reduction of the magnetic entropy was observed for the ternaries $CePd_2Al_2$, $CePd_3Al_3$ and the $CePd_4Al_4$ compounds and this was attributed to the competition between the Ruderman – Kittle – Kasuya – Yosida (RKKY) interaction and the Kondo effect which means that the Kondo effect suppresses the part of the magnetic entropy above the ordering temperature [86, 88]. It was also speculated that this shortfall of magnetic entropy may result from short – range correlations above T_N. In the case of the $NdPd_2Al_2$ compound, one can speculate that, the reduction of magnetic entropy may be attributed to short-range correlations of the Nd magnetic moments above T_N or the observed metamagnetism in this compound.

3.3.3. Isothermal magnetization and Belov Arrot plots

The field variations of the isothermal magnetization, $M(H,T)$ in the $NdPd_2Al_2$ compound, measured in an applied magnetic field up to 6.7 T and in the temperature range 2 - 30 K in steps of 2 K are depicted in Figure 3.5(a). A clear metamagnetic transition is observed at low fields for most of the isotherms. The high-temperature isotherms exhibit a linear behaviour in stronger fields, while the low-temperature isotherms show a downward curvature with a tendency toward saturation above 6.7 T. The magnitude of the magnetization at 6.7 T decreases from 1.75 μ_B to 0.50 μ_B with increasing temperature, probably due to the high – field FM state.

Figure 3.5(b) displays the Belov - Arrott plots, M^2 vs. H/M [111, 112], constructed from the $M(H,T)$ data. The inset of Figure 3.5(b) illustrates the negative and positive slopes of the Belov - Arrott plots, just below and above T_N, respectively. Based on Banerjee criterion [113] the observed negative slope of the curve taken below T_N signals a first-order metamagnetic transition from the AFM phase to a field-induced FM phase. In turn, the positive slopes appearing above T_N indicate a second–order nature of the paramagnetic to AFM state.

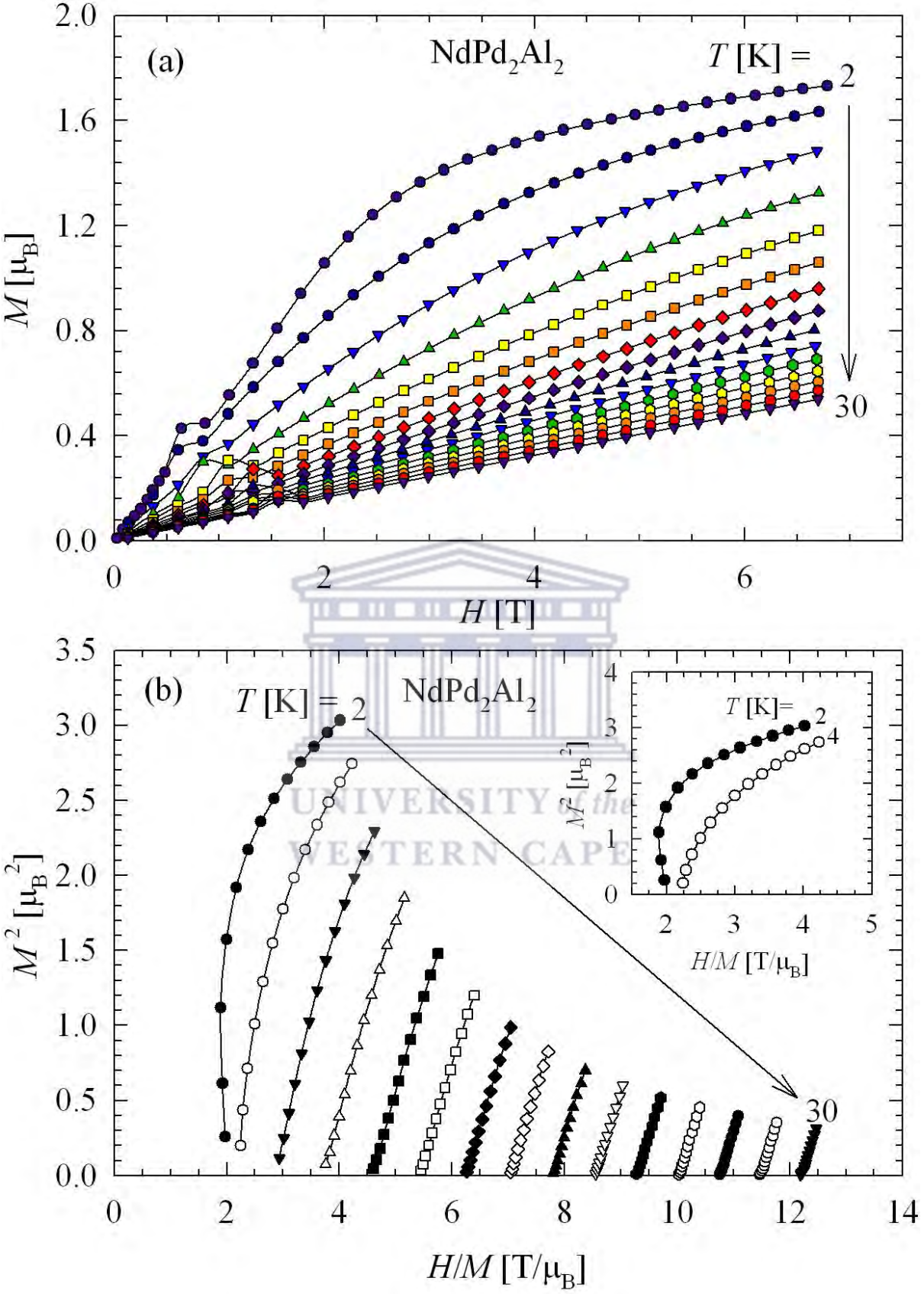

Figure 3.5: (a). The field variation of the isothermal magnetization, $M(H,T)$ of $NdPd_2Al_2$ compound measured at several temperatures in the range 2 - 30 K in steps of 2 K in magnetic field up to 6.7 T. (b) The standard Belov - Arrott plots for the mean-field model, M^2 vs. H/M.

3.3.4. Magnetocaloric effect

Magnetocaloric effect (MCE) refers to the change in magnetic entropy, ΔS_M or the adiabatic temperature change, ΔT_{ad}. Both ΔS_M and ΔT_{ad} have been estimated from the isothermal magnetization, $M(H,T)$ data as well as from heat capacity data measured in zero magnetic fields, based on the Maxwell thermodynamic relationship [114, 115]:

$$\Delta S_M(H,T) = \int_0^H \left(\frac{\partial M(H,T)}{\partial T}\right)_H dH', \tag{3.3}$$

$$\Delta T_{ad} = -\frac{T\Delta S_M}{C_p(T,H)}. \tag{3.4}$$

The resulting temperature variations of $-\Delta S_M$ and ΔT_{ad} are plotted in Figures 3.6(a) and 3.6 (b) respectively for different magnetic field changes up to 6.7 T. It is observed that this compound shows positive MCE in the entire measured temperature range, regardless of the magnetic field change, ΔH. Generally, it has been observed that conventional ferromagnets exhibit positive MCE, while antiferromagnets may exhibit negative MCE. In some cases, rare–earth based AFM materials display the effect of changing the sign of the MCE from negative to positive that occurs close to first-order metamagnetic transition from AFM to field-induced FM state [116 − 119]. As can be inferred from Figures 3.6(a) and 3.6(b), both $-\Delta S_M$ and ΔT_{ad} exhibits a peak around T_N with a magnitude that increases systematically with rising ΔH. The maximum $-\Delta S_M^{max}$: ΔT_{ad}^{max} amounts to: 16.53 J/kg.K : 9.41 K, 12.14 J /kg.K : 6.31 K and 3.16 J/kg.K : 1.63 K for a magnetic field changes of ΔH = 7, 5 and 2 T, respectively. It should be noted that the values of $-\Delta S_M^{max}$ and ΔT_{ad}^{max} obtained for the magnetic field change of 5 and 7 T are comparable and even larger to those reported in the literature for various potential magnetic refrigerant materials (see Table 3.3).

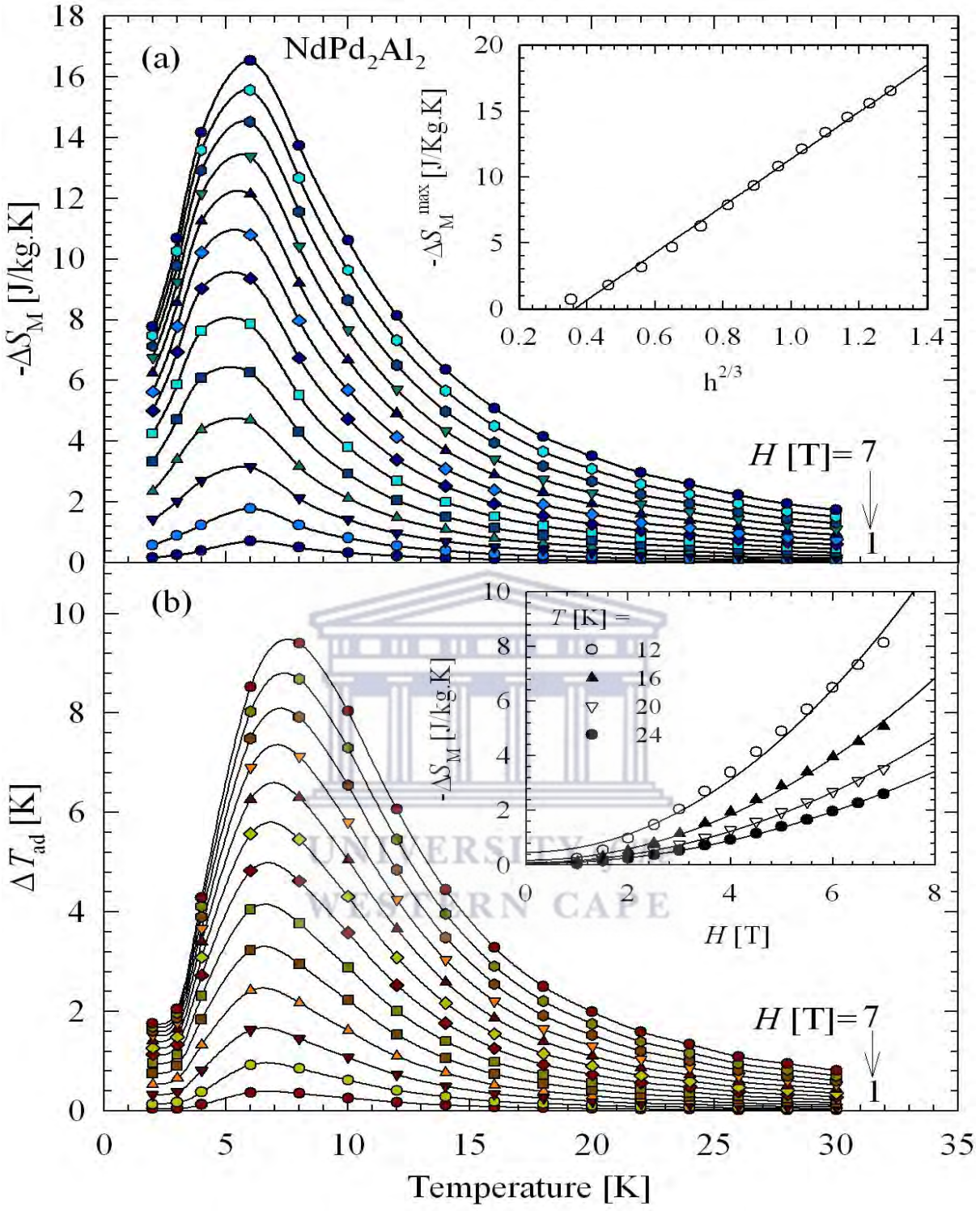

Figure 3.6: The field variations (a) of the isothermal magnetic entropy changes, $-\Delta S_M(T)$ and (b) the adiabatic temperature changes, $\Delta T_{ad}(T)$ in $NdPd_2Al_2$ compound measured in different field change in steps of 0.5 T. The inset of (a) displayed the maximum isothermal magnetic entropy change, $-\Delta S_M^{max}$ as a function of the reduced field $h^{2/3}$ (see text for the definition). The solid line is the LSQ fit of Eq. 3.5 to the experimental data. The inset of (b) displayed the magnetic field dependence of the magnetic entropy change, $-\Delta S_M$ at different temperatures above T_N. The solid curves are the quadratic fit of $-\Delta S_M$ data to (H^2) of $NdPd_2Al_2$ compound.

In order to probe the magnetic properties related with magnetic entropy changes for $NdPd_2Al_2$, the maximum values of $-\Delta S_M^{max}$ were plotted in the inset of Figure 3.6(a) as a function of $h^{2/3}$, where h is the reduced magnetic field ($h = H.\ \mu_B / k_B.T_N$), and the magnetic field dependence of $-\Delta S_M$ was taken at various temperatures in the paramagnetic region, and plotted in the inset of Figure 3.6(b). It should be noted that, for magnetic materials with second-order phase transition, $-\Delta S_M^{max}$ generally follows the relation [120]

$$-\Delta S_M^{max} = S(0,1)h^{2/3} + S(0,0), \tag{3.5}$$

where $S(0,1) = kM_s(0)$ is a parameter connected to the spontaneous magnetization $M_s(0)$ at $T = 0$ K (k being a constant) and $S(0,0)$ is a non - zero reference parameter [120]. The high magnetic field fitting of Eq. 3.5 to the $-\Delta S_M^{max}$ data (note the solid line in the inset of Figure 3.6(a)) yielded the values: $S(0,1)$ = 6.37(9) J/kg.K and $S(0,0)$ = − 6.7(2) J/kg.K. The negative sign of $S(0,0)$ reveals a second-order phase transition [121, 122] while the linear behaviour of $-\Delta S_M^{max}$ vs. $h^{2/3}$ suggests a strong localization of the Nd magnetic moment in the compound studied [123]. As inferred from the inset of Figure 3.6(b), it is observed that the compound exhibits a quadratic dependence of MCE ($-\Delta S_M \propto H^2$), which indicates the presence of spin fluctuation in the paramagnetic region [124, 125].

From the view point of applications, two important quality factors or figure of merit of magnetic refrigerant materials are commonly used to check the performance of magnetocaloric materials, which could measure the amount of heat transfer between the hot and cold reservoirs during an ideal refrigeration cycle. These are the refrigerant capacity (RC) or a closely quality factor that is called the relative cooling power (RCP). The values of RCP refers to the product of the maximum entropy change, $-\Delta S_M^{max}$ and the full width at half maximum δT_{FWHM} in the $-\Delta S_M(T)$ curve and can be described as [52, 126, 127]:

$$RCP = -\Delta S_M^{max}.\delta T_{FWHM}. \tag{3.6}$$

In contrast, the RC is calculated by numerically integrating the area under the $\left(-\Delta S_M(T)\right)$ curve, taking the half maximum of the peak as the integration limits:

$$RC = \int_{T_1}^{T_2} |\Delta S(T,H)|\, dT, \tag{3.7}$$

where T_1 and T_2 are the temperatures of the cold end and the hot end of an ideal thermodynamic cycle, respectively. Figure 3.7 displays *RC* and *RCP* of $NdPd_2Al_2$ compound estimated for different magnetic field changes. As inferred in this figure, both figures of merits continuously increase with increasing ΔH. It should be noted that enhanced values of *RC* and *RCP* in the compound investigated result from both the spread of $-\Delta S_M$ over a wide temperature range, which leads to large values of δT_{FWHM}, and the significant values of $-\Delta S_M^{max}$, associated with the field-driven first-order magnetic phase transition from AFM to FM states. The obtained values of *RC* / *RCP* are: 21.76 / 18.83 J/kg, 106.82 / 82.97 J/kg and 167.24 / 126.69 J/kg for ΔH = 2, 5 and 7 T, respectively. Remarkably these values are comparable to those reported for promising good refrigerant materials (see Table 3.3) and this indicates that the $NdPd_2Al_2$ compound is a novel candidate for application in magnetic refrigeration. Furthermore, it is worthwhile noting that for a second-order MCE material with a typical single triangle peak around T_C / T_N in $-\Delta S_M(T)$ curve, the magnitude of *RC* is around 25% higher than that of the *RCP* [128]. In the present case for a magnetic change of 7 T, the observed magnitude of *RC* is about 24.2% higher than that of *RCP*, which confirms that the $NdPd_2Al_2$ compound is a second-order MCE material.

Based on these figures of merit Smith *et al*. [129] reported that both concepts are based on a minimization approach that is not representative of practical applications. Furthermore, they noted that these figures of merits and the adiabatic temperature changes are as important as the magnetic entropy change from point of view of applications. Therefore, *RC* and *RCP* lead to an overestimation of the material performance in some cases. To overcome this discrepancy, Hood and Potter [127] suggested the dimensionless figure of merit called the coefficient of refrigerant performance (*CRP*):

$$CRP = \frac{\Delta S_M . \Delta T}{\int_0^{H_{max}} M(T_{C/N}, H')\, dH'}, \tag{3.8}$$

where the normalization term at the denominator represents the work done on refrigerants, calculated by numerically integrating the area under the magnetization isotherm at the magnetic phase transition temperature, T_C / T_N. From Eq. 3.8, it is evident that the maximization approach, $\Delta T = \delta T_{FWHM}$ criterion suggested by Wood and Potter leads to the same limitations as *RC* and *RCP*. Guillou *et al*. [80] suggest the use of $\Delta T = \Delta T_{ad}$ criterion for MCE materials based on the continuous transition. Thus, the product $-\Delta S_M^{max} . \Delta T_{ad}^{max}$ will be used at the

numerator of *CRP*. The advantage is that this approach takes into account both the magnetic entropy change and the adiabatic temperature change. The inset of Figure 3.7 displays the field dependence of *CRP*. Similar to *RC* and *RCP*, *CRP* continuously increases with increasing magnetic field changes and the values obtained for ΔH = 7, 5 and 2 T amount to 18.63, 9.17 and 0.62, respectively. Once again, these magnitudes of *CRP* indicate that $NdPd_2Al_2$ is a potential magnetocaloric material for magnetic refrigeration technology.

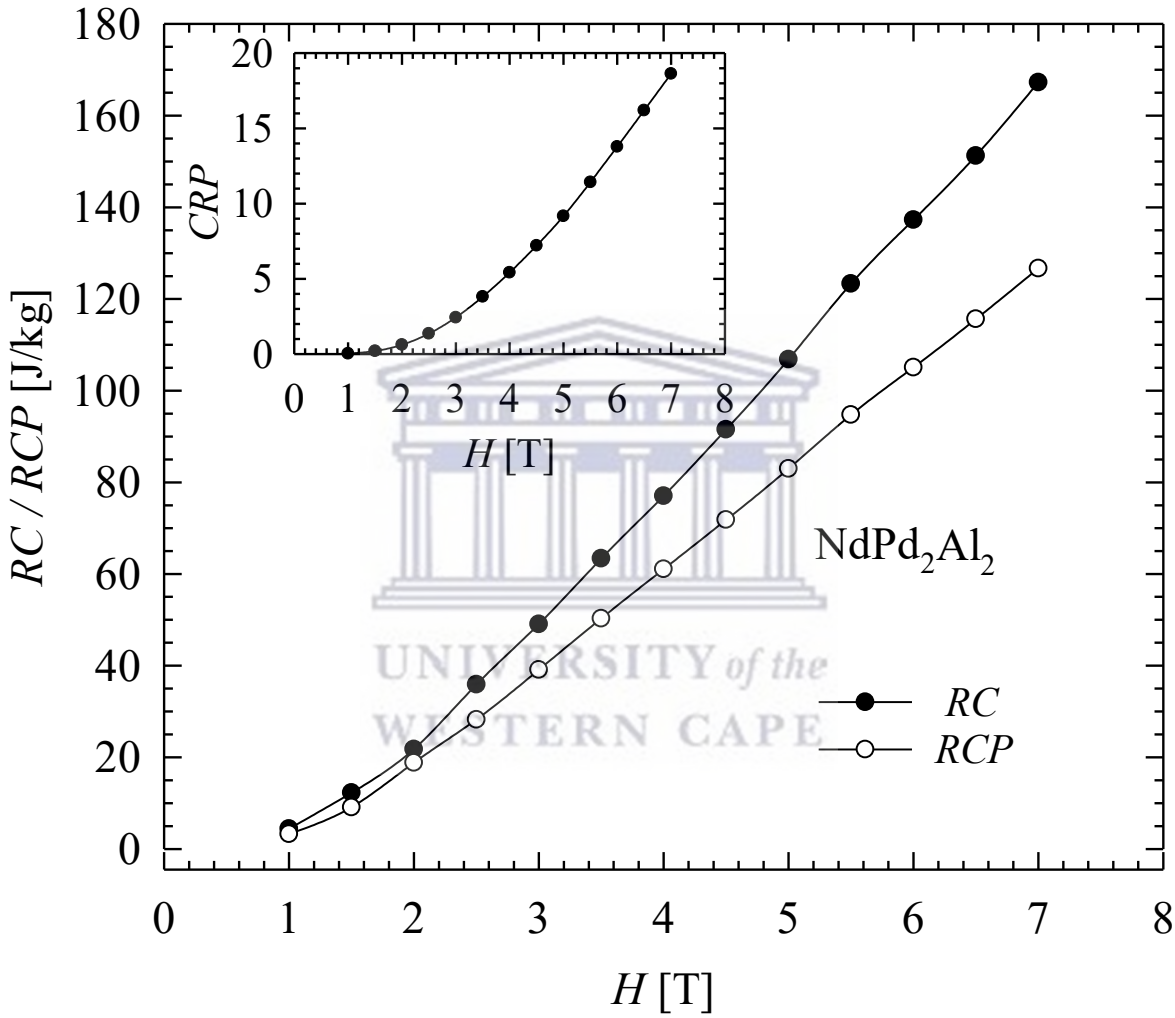

Figure 3.7: The magnetic field variations of the refrigerant capacity, *RC* (close symbols) and the relative cooling power, *RCP* (open symbols) calculated for the $NdPd_2Al_2$ compound using Eqs. 3.6 and 3.7, respectively. The inset displays the coefficient of refrigerant performance, *CRP* calculated using Eq. 3.8.

Table 3.3: The transition temperature (T_M), the maximum magnetic entropy change ($-\Delta S_M^{max}$), the maximum adiabatic entropy change (ΔT_{ad}^{max}), the refrigerant capacity (RC) for a field change of ΔH = 5 T for selected rare - earth based intermetallic compounds. The notation "−" means value reported in the literature.

Compound	$T_M[K]$	$-\Delta S_M^{max}$[J/kg. K]	$\Delta T_{ad}^{max}[K]$	$RC[J/KG]$	**Ref**
$NdPd_2Al_2$	3	12.14	6.31	106.82	This work
NdCuSi	3.1	11.1	-	-	[127]
GdCuSi	14.2	8	5.4	-	[130]
GdRhSn	16.2	6.5	4.5	-	[131]
DyRhSn	7.2	7.2	5.2	-	[132]
HoPdIn	23	14.6	5.5	496	[116]
NdCuGa	7	5.53	5.29	81.29	This work
TbTiGe	300	4.3	4.2	-	[133]
Ho_2Ni_2Ga	12.5	5.4	-	121	[131]
Tm_2Co_2Ga	5.5	2.4	-	32	[134]
Ho_2Ni_2Al	12/6	6	-	151	[135]
Er_2Co_2Al	32/21	5.9	-	152	[135]
Tm_2Co_2Al	11.5/7	7.7	-	127	[135]
Dy_2Co_2Ga	55	6.2	-	152	[136]

3.4. Summary

In summary, the compound $NdPd_2Al_2$ synthesized in this study possesses the $CaBe_2Ge_2$ - type crystal structure with space group *P4/nmm*. The low-temperature transport, magnetic and heat capacity studies, reveal that the compound exhibit AFM ordering below T_N = 3 K and that a relatively small magnetic field induces a transition from AFM to the FM state that seems to bear a first-order character. The magnetic entropy change suggests a spin fluctuation in the paramagnetic region and that the AFM phase transition in $NdPd_2Al_2$ has a second-order nature. Furthermore, the magnitude of *RC* and *RCP* for ΔH = 7 T classified $NdPd_2Al_2$ as a second-order MCE material. Large values of MCE obtained for this compound suggest that $NdPd_2Al_2$ is a potential candidate for magnetic refrigeration**.**

CHAPTER 4

THERMODYNAMIC PROPERTIES OF RECuGa where RE = Nd, Dy and Ho

In this chapter, we report the thermodynamic properties of the orthorhombic polycrystalline RECuGa (where RE = Nd, Dy and Ho) compounds. These compounds exhibit a putative antiferromagnetic (AFM) ordering below T_N = 7.1, 8.5 and 3.7 K for Nd, Dy and Ho, respectively, as observed from the magnetic susceptibility, $\chi(T)$ and heat capacity, $C_p(T)$ data. The Belov - Arrott plots indicate a second-order nature of the magnetic phase transition for all three compounds. At high temperature, $\chi(T)$, the data follows the paramagnetic Curie - Weiss behaviour with an effective magnetic moment, $\mu_{eff} =$ 3.658(2)μ_B, 10.850(2)μ_B and 10.568(4)μ_B for the Nd, Dy and Ho compounds, respectively. These values are reasonably close to the theoretical value of 3.62 μ_B expected for the free Nd^{3+} - ion, 10.65 μ_B expected for the free Dy^{3+} - ion and 10.61 μ_B expected for the free Ho^{3+} - ion. The LSQ fit parameters also yield the Weiss temperature θ_p = −4.4(3), −1.7(1) and −3.3(2) K for Nd, Dy and Ho, respectively.

For Nd, just above T_N, $C_p(T)$ data can be fitted to the Debye - relationship giving a Sommerfeld coefficient and the Debye temperature values of γ = 0.210(1) J/mol.K^2 and θ_D = 99(8) K, respectively. The magnetocaloric effect (MCE) was investigated from the magnetic entropy change $(-\Delta S_M)$ and the adiabatic temperature change (ΔT_{ad}), both estimated from the isothermal magnetization, *M* (*H*, *T*) and the zero field $C_p(T)$ data. The maximum values of both $-\Delta S_M$ and ΔT_{ad} were estimated to be 8.59 J/kg.K and 7.1 K for a field change of 7 T for Nd. For Dy and Ho, the magnitude of the maximum of $-\Delta S_M(T)$ were estimated to be 16.73 J/kg.K and 37.11 J/kg.K, for a field change of 7 T, respectively. The corresponding relative cooling power (*RCP*), the refrigeration capacity (*RC*) and the coefficient of refrigerant performance (*CRP*) was found to be 150 J/kg, 109 J/kg and 4.65 for Nd, 653 J/kg, 478 J/kg and 16 J/kg for Ho, respectively. These figures are similar to those reported for materials that can be used as magnetic refrigerants.

4.1. Literature review and introduction

The family of rare-earth intermetallic RETX compounds (RE = rare earth element, T = 3d/4d/4d transition metals and X = p - block elements) have always attracted special interest and have been the subject of extensive investigations due to the variety in their ground state behaviour [137 - 139]. These compounds crystallize in different crystal structures, depending on the constituent elements. As a result of these different crystal structures, they exhibit a versatile magnetic and electrical properties such as Kondo effect, heavy fermion behaviour, complex magnetic structure, valence fluctuation, unconventional superconductivity, magnetic polaronic behaviour, non–Fermi liquid behaviour, metamagnetism, spin–glass, memory effect, magnetoresistance (MR), magnetocaloric effect (MCE) etc [140]. On the other hand, these compounds show pressure effects on their structural and magnetic properties.

Several investigations were reported in the literature for these compounds. This includes DC magnetization (both zero - field cooled (ZFC) and field – cooled (FC)), AC susceptibility, thermoelectric power, thermal conductivity, Hall - effect, electrical resistivity, heat capacity, neutron diffraction, Mössbauer spectroscopy, muon - spin relaxation, MCE etc. [141 - 148]. Chemical pressure (effect of La dilution) and hydrostatic pressure were also reported [148]. Due to the localized moments in the 4f shell in rare-earth atoms, the Ruderman – Kittel – Kasuya – Yosida (RKKY) interaction is dominant in these compounds, especially when T is a nonmagnetic element. Except for Mn, all other transition elements possess nearly zero magnetic moment in these compounds. It has been observed that the magnetic ordering temperatures (Néel temperature, T_N or Curie temperature, T_C) in these compounds vary from low temperatures to the room temperature. Some of these compounds order ferromagnetically, while others order antiferromagnetically. Some compounds of this series are found to show complex magnetic behaviour.

$CeCu_2$ is well known to be a dense Kondo system, which exhibits unusual antiferromagnetic order below 3.4K [149 - 153]. The substitution of one Cu by Ga or Ge in $CeCu_2$ was reported [154, 155]. The resulting CeCuGa or CeCuGe has been shown to introduce drastic changes of the electronic properties [156 - 158] and crystal structure in the case CeCuGe which crystallizes in the hexagonal AlB_2 – type structure [159] while CeCuGa retains the orthorhombic structure of $CeCu_2$. The observed suppression of the ordering temperature in the case of CeCuGa may indicate a strong competition between the Kondo effect and RKKY (Ruderman – Kittel – Kasuya – Yosida) interactions. Conversely, CeCuGe exhibits ferromagnetic transition at T_C =

10 K, strongly influenced by spin fluctuations [159]. In the case of CeCuGa homologue compound to RECuGa (RE = Nd, Dy, Ho) in this study, XRD study reveals no superlattice reflections ($h + k + l$ = odd), which indicates that the Cu and Ga atoms in CeCuGa are randomly distributed over the Cu sites in $CeCu_2$ structure. The specific heat study shows a wide peak at 1 K, and a high value of the electronic coefficient, $\gamma = 1200\ \mathrm{mJ/mol.K^2}$. The temperature of the wide peak in specific heat at 1 K in magnetic fields further suggests that the high-value γ of CeCuGa is due to Kondo effect.

Based on the rich ground state properties of the RETX compounds, we undertake to investigate in this chapter the thermodynamic properties of the ternary NdCuGa, DyCuGa and HoCuGa compounds through XRD, magnetic susceptibility, isothermal magnetization and heat capacity measurements. MCE was investigated from the isothermal magnetization data and heat capacity.

4.2. Crystallography

Polycrystalline samples of RECuGa (RE = Nd, Dy and Ho) were synthesized as indicated in chapter 2. The quality of the product was examined by XRD measurements using a Bruker D8 advance powder diffractometer with CuKα radiation and the scanning electron microscope (SEM) described in chapter 2. The diffraction patterns of all three compounds were qualitatively and quantitatively analyzed using the CAILS – Pawley and the Rietveld refinement methods from TOPAS ACADEMIC programme presented in chapter 2. The chemical composition was checked by EDS.

4.2.1. Structural Characterization: X-ray diffraction

XRD diffractograms obtained for RECuGa (where RE = Nd, Dy and Ho) compounds together with the CAILS and Rietveld refinement fits to the data are shown in Figure 4.1, 4.2 and 4.3 for Nd, Dy and Ho compounds, respectively. The analysis of the diffraction pattern was done as described in ref. [159]. It should be noted that the CAILS refinement method is different from the traditional Rietveld refinement technique in the sense that only cell parameters, peak - width parameters and integrated intensities are refined. CAILS refinement is independent of the atomic position parameters (or structural model) and only depends on the space group symmetry. Furthermore, in the CAILS method, the intensities of all peak vary independently.

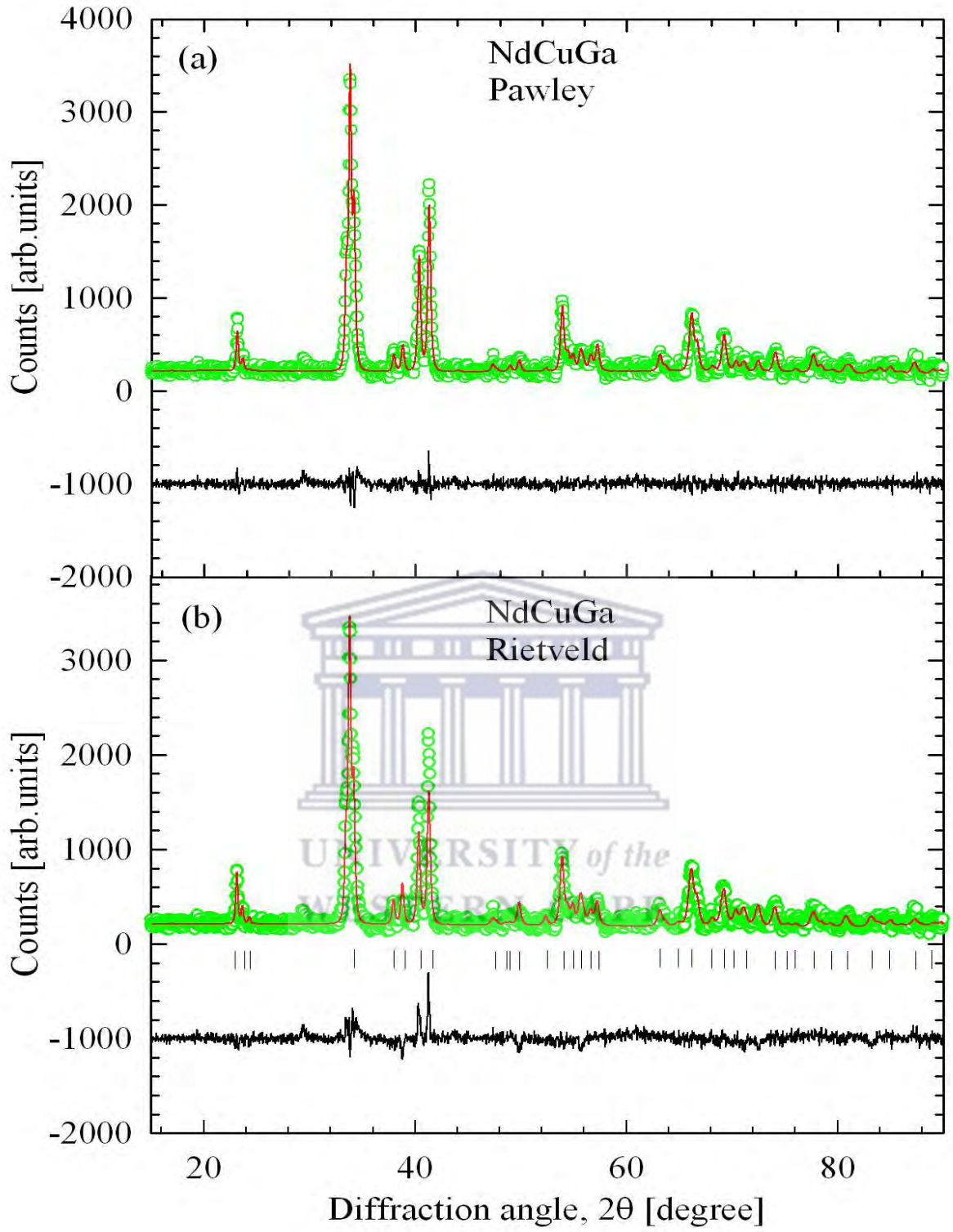

Figure 4.1: (a) CAILS - Pawley and (b) Rietveld analyzed diffraction patterns of NdCuGa compound. The observed data are shown by green symbols and the red solid lines through the data represent the results of the CAILS - Pawley and structure Rietveld refinements. The lower black curves are the difference curves between the experimental data and the calculated curve and the vertical black lines in (b) are the Bragg positions.

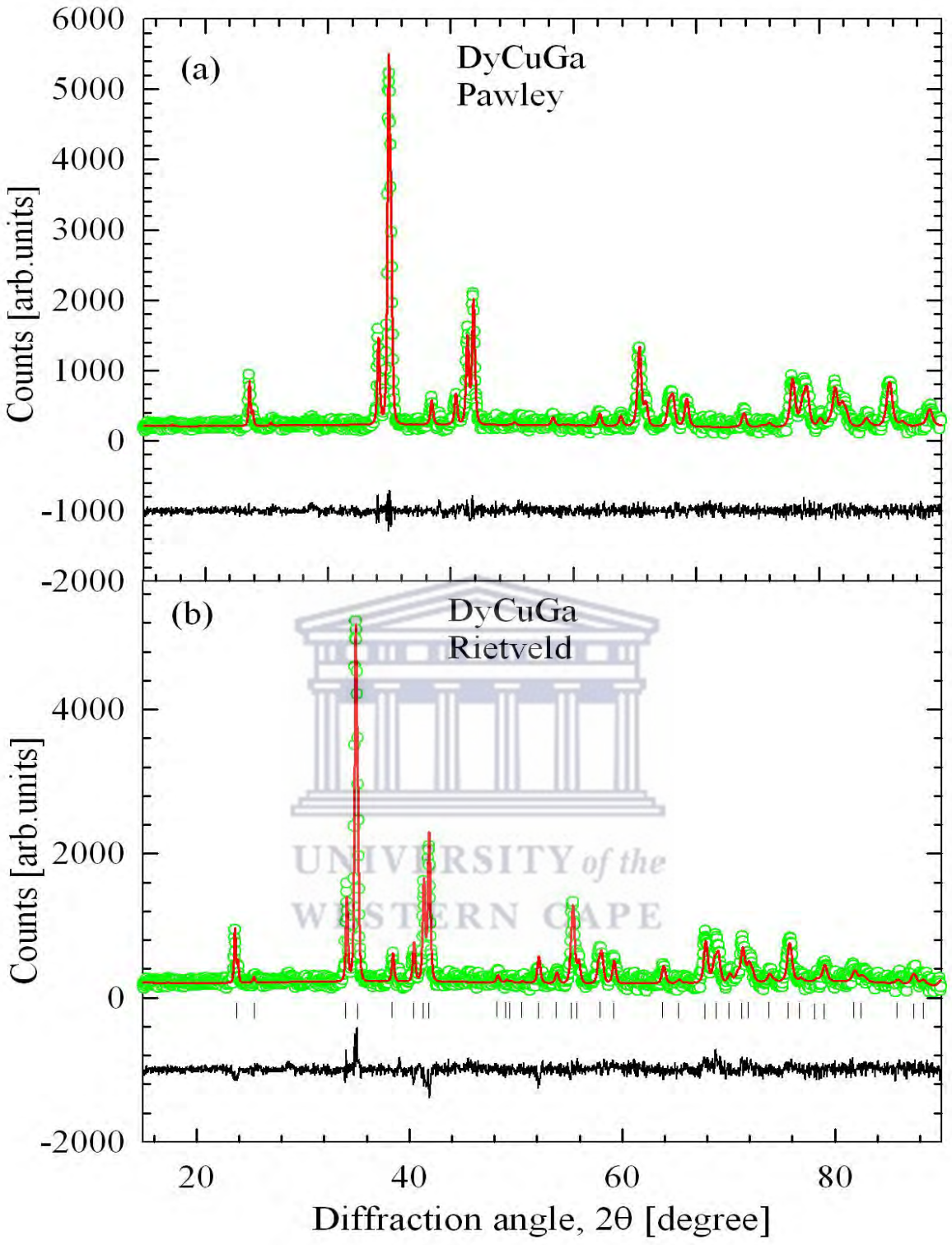

Figure 4.2: (a) CAILS - Pawley and (b) Rietveld analyzed diffraction patterns of DyCuGa compound. The observed data are shown by green symbols and the red solid lines through the data represent the results of the CAILS - Pawley and structure Rietveld refinements. The lower black curves are the difference curves between the experimental data and the calculated curve and the vertical black lines in (b) are the Bragg positions.

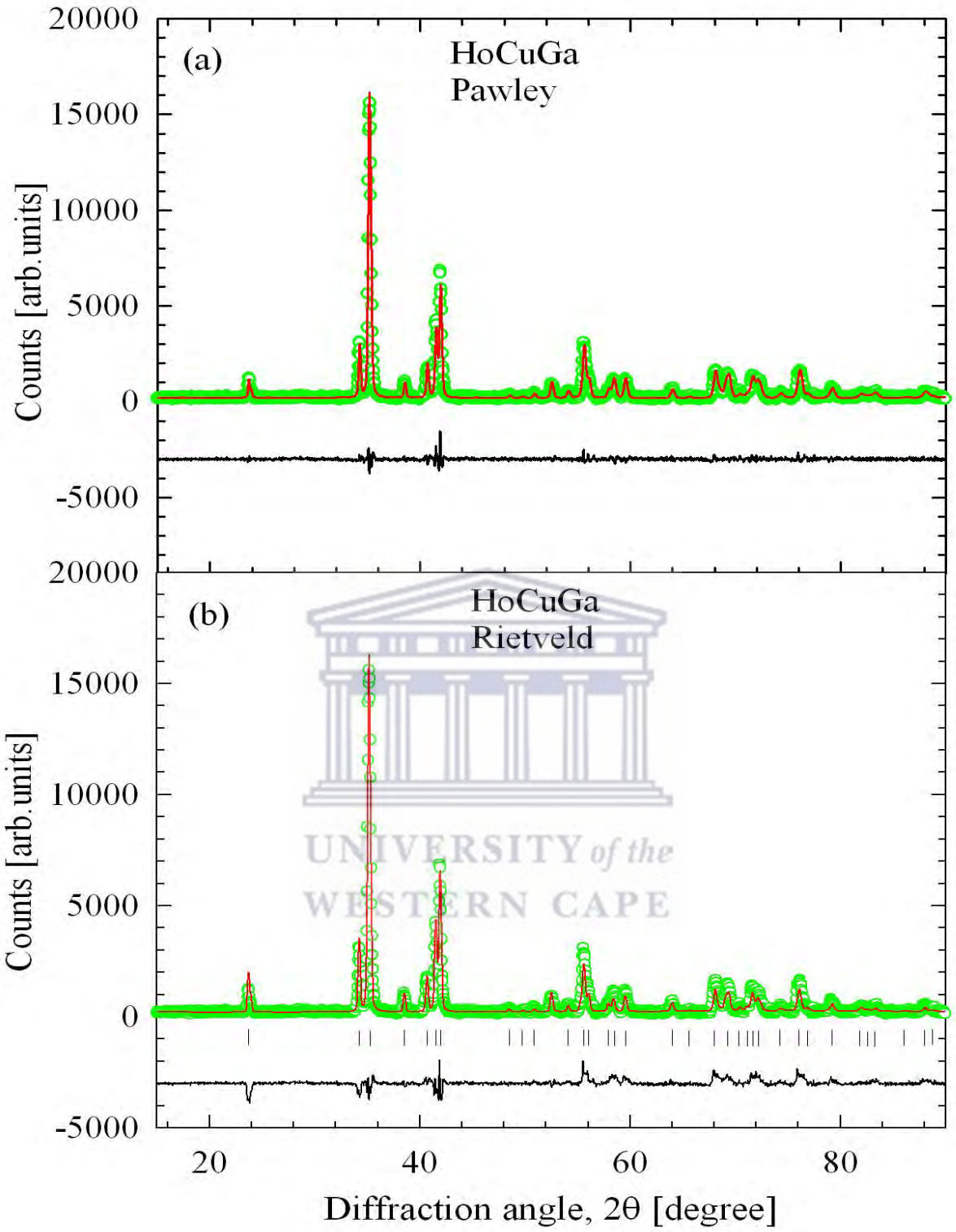

Figure 4.3: (a) CAILS - Pawley and (b) Rietveld analyzed diffraction patterns of HoCuGa compound. The observed data are shown by green symbols and the red solid lines through the data represent the results of the CAILS - Pawley and structure Rietveld refinements. The lower black curves are the difference curves between the experimental data and the calculated curve and the vertical black lines in (b) are the Bragg positions.

The experimental data were first analyzed using the CAILS - Pawley method in order to obtain the lattice parameters. The space group setting used in the refinement was *Imma* (No. 74) of the orthorhombic $CeCu_2$ - type structure. The resulting lattice parameters and unit cell volume are listed in Table 4.1. The unit cell volume obtained for Nd, Dy and Ho compounds are smaller than the value of 252.1 $Å^3$ [160] or 250.6 $Å^3$ [155] obtained for the equiatomic compound CeCuGa and satisfied the relation $V_{CeCuGa} \leq V_{NdCuGa} \leq V_{DyCuGa} \leq V_{HoCuGa}$. This observation confirms the lanthanide contraction, moving from Ce to Ho. In the space group setting, Nd, Dy and Ho atoms occupy the 4e - site while Cu and Ga are randomly distributed on the 8h - site. The Rietveld refinement analysis yielded the atomic coordinates listed in Table 4.2. The calculated atomic coordinates for Nd, Dy and Ho compounds are in good agreement with that obtained for EuAgGe [161]. In the refinements, the site occupancies were assumed to be full at the two crystallographic sites, and the isotropic displacement parameters were kept fixed for all atoms. The resulting refinement residuals (for their definition see chapter 2) from both the CAILS - Pawley and Rietveld methods are listed in Table 4.3. It is observed from Table 4.3 that the values of these residuals are comparable for the two methods and prove the correctness of the structural model applied. The resulting orthorhombic crystal structure of the RECuGa is shown in Figure 4.4.

Table 4.1: Room temperature lattice parameters and the unit cell volume of NdCuGa, DyCuGa and HoCuGa in the CAILS – Pawley and the full - structure Rietveld refinements methods.

Compound	Parameters	CAILS - Pawley	Rietveld
NdCuGa	*a* [Å]	4.4663(7)	4.4613(7)
	b [Å]	7.314(1)	7.304(1)
	c [Å]	7.510(1)	7.501(1)
	V [$Å^3$]	245.30(7)	244.42(6)
DyCuGa	*a* [Å]	4.359(7)	4.3582(6)
	b [Å]	7.005(1)	7.0038(8)
	c [Å]	7.438(1)	7.4372(9)
	V [$Å^3$]	227.16(6)	227.02(5)
HoCuGa	*a* [Å]	4.3422(4)	4.3449(4)
	b [Å]	6.9573(7)	6.9612(7)
	c [Å]	7.4257(7)	7.4301(6)
	V [$Å^3$]	224.33(4)	224.73(4)

Table 4.2: Atomic coordinates, site occupancy (S.O.), and the isotropic displacement parameter (B_{iso}) for NdCuGa obtained from the full - structure Rietveld refinement method using the *Imma* space group. The S.O. and the B_{iso} were kept fixed (fully occupied). Letter X on the atoms represents the Cu and the Ga atoms.

Atom	Wyckoff site	*x*	*y*	*z*	S.O	B_{iso}
Nd	4e	0	1/4	0.5365(5)	1	1
X	8h	0	0.0484(8)	0.1675(9)	1	1
Dy	4e	0	1/4	0.5379(6)	1	1
X	8h	0	0.0487(8)	0.165(1)	1	1
Ho	4e	0	1/4	0.5351(6)	1	1
X	8h	0	0.04(6)	0.16(6)	1	1

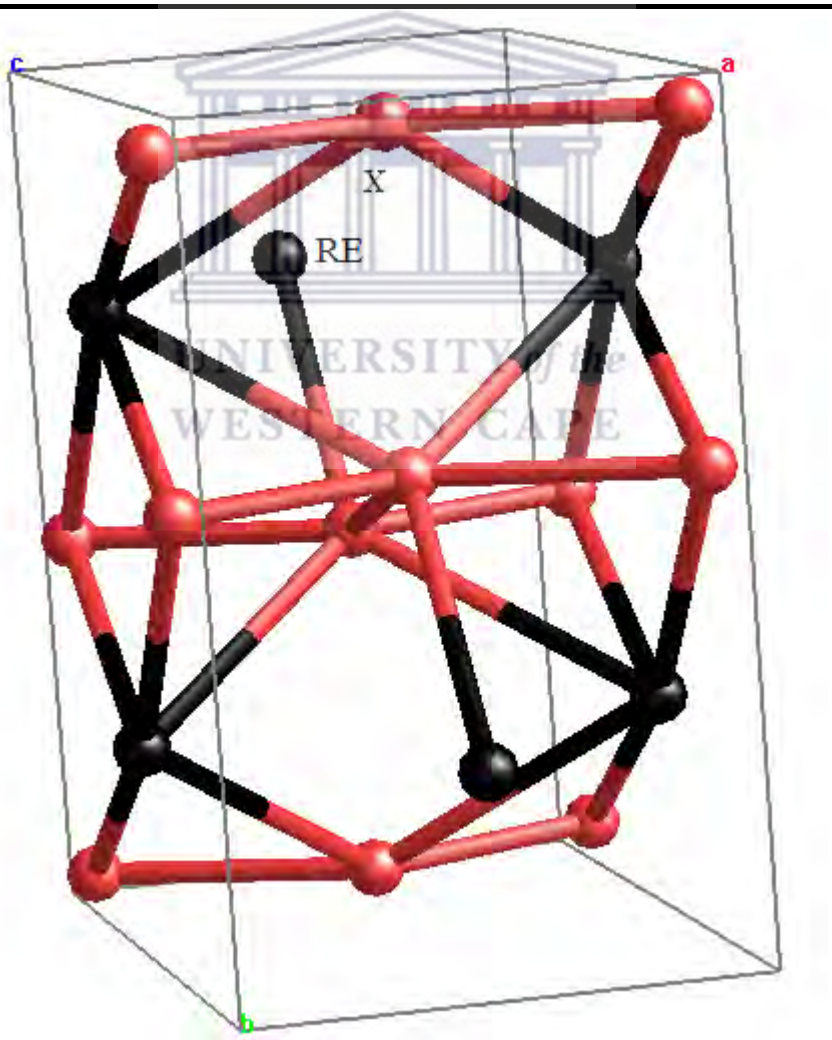

Figure 4.4: The orthorhombic crystal structure of RECuGa. The black circles represent the RE atoms (Nd, Dy or Ho). The red circles represent X = 50% Cu + 50% Ga.

Table 4.3: Values of the residual factors (all the symbols have their usual meaning) in the CAILS – Pawley and the full - structure Rietveld refinements method performed for Nd, Dy and Ho compounds, together with calculated phase density (PD).

Compound	Parameters	CAILS - Pawley	Rietveld
NdCuGa	R_{wp}[%]	13.243	15.755
	R_{exp}[%]	5.698	5.777
	R_p[%]	9.978	12.172
	χ^2	2.324	2.727
	DW	1.673	1.82
	R_B[%]		7.837
	PD[g/cm^3]		7.374(2)
DyCuGa	R_{wp}[%]	16.441	18.056
	R_{exp}[%]	5.450	5.524
	R_p[%]	12.020	13.690
	χ^2	3.016	3.269
	DW	1.796	1.494
	R_B[%]		7.794
	PD[g/cm^3]		8.473(2)
HoCuGa	R_{wp}[%]	14.124	22.254
	R_{exp}[%]	4.484	4.545
	R_p[%]	10.171	16.672
	χ^2	3.150	4.896
	DW	1.495	0.633
	R_B[%]		12.129
	PD[g/cm^3]		8.814(1)

4.2.2. Characterization by Scanning Electron Microscope

Micrographs of RECuGa (where RE = Nd, Dy and Ho) taken using a scanning electron microscope (SEM) at the working distance of 100 μm are shown in Figures 4.5(a), 4.5(b) and 4.5(c) for the Nd, Dy and Ho compounds, respectively. These micrograph images show a single phase, with the slight discolouration attributed to the polycrystalline nature of the samples. They are also characterized by smooth surfaces, which confirms the homogeneity of the compound. There are cracks or scratches visible from the polishing of the surface prior to the scanning process, which is more visible in Figures 4.5(a) and 4.5(b). The atomic ratios normalized to the RE atom as obtained from electron dispersive spectroscopy (EDS) are listed

in Table 4.4. It can be observed that the chemical composition are $NdCu_{0.976(2)}Ga_{0.962(2)}$, $DyCu_{0.981(2)}Ga_{0.978(2)}$ and $HoCu_{1.070(2)}Ga_{1.018(2)}$ which is close to the nominal ratio. The small offsets can be ascribed to minor mass loss that occurred during the arc melting process.

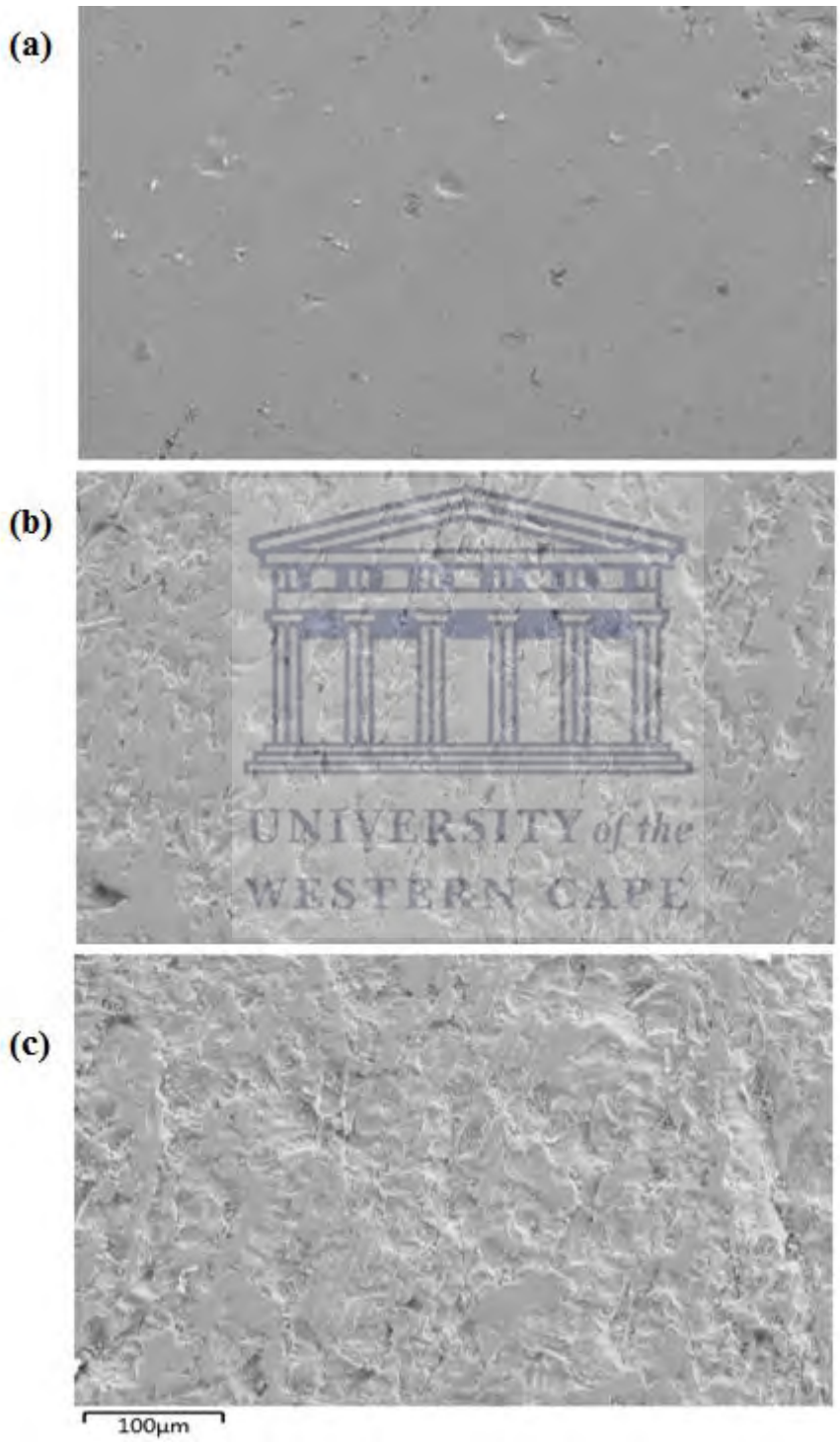

Figure 4.5: SEM cross section micrographs taken at a scale of 100 μm for (a) NdCuGa (b) DyCuGa and (c) HoCuGa.

The composition was checked on several places of the crystal, showing small deviations from the homogeneous distribution of the individual elements. These deviations are lower than 3%, which are comparable to the experimental error.

Table 4.4: Elemental composition for NdCuGa, DyCuGa and HoCuGa compounds as obtained from EDS. Carbon (C) and oxygen (O) are impurities arising during the polishing process.

Compound	Element	Atomic%	Atomic Ratios
NdCuGa	Nd	15.13	1.000(2)
	Cu	14.71	0.972(2)
	Ga	14.54	0.961(2)
	C	50.13	0.339(2)
	O	5.48	3.313(2)
DyCuGa	Dy	14.91	1.000(2)
	Cu	14.62	0.981(2)
	Ga	14.58	0.978(2)
	C	50.56	3.391(2)
	O	5.32	0.357(2)
HoCuGa	Ho	14.52	1.000(2)
	Cu	15.54	1.070(2)
	Ga	14.78	1.018(2)
	C	50.18	3.456(2)
	O	4.99	0.344(2)

4.3. Magnetic susceptibility and magnetization

The inverse magnetic susceptibility, $\chi^{-1}(T)$ of RECuGa (RE = Nd, Dy and Ho) compounds measured in a field of 0.1 T and temperature range $1.7 \leq T \leq 400$ K are depicted in Figure 4.6. Above 60 K, $\chi^{-1}(T)$ data for all three compounds follows the Curie - Weiss (CW) behaviour:

$$\chi^{-1}(T) = \frac{3k_B(T - \theta_p)}{N_A \mu_{eff}^2}, \tag{4.1}$$

where N_A is the Avogadro's number, k_B is the Boltzmann's constant, μ_{eff} denotes the effective

magnetic moment and θ_p is the paramagnetic Weiss temperature. Least square (LSQ) fits of Eq. 4.1 to the experimental data are depicted in Figure. 4.6 (solid red line). The resulting LSQ fit yields the values of μ_{eff} =3.658(2)μ_B, 10.850(2)$\mu_B$and 10.568(4)μ_B for the Nd, Dy and Ho compounds, respectively. These values are close to their theoretical values for the trivalent RE ion ($g_j\sqrt{j(j+1)} = 3.62\ \mu_B$, 10.65 μ_B and 10.61 μ_B for Nd, Dy and Ho, respectively). This results clearly designates the Nd^{3+}, Dy^{3+} and Ho^{3+} ions as the only source of magnetism in these compounds. The values of Weiss temperature are θ_p = – 4.4(3), – 1.7(2) and – 3.3(2) K for the Nd, Dy and Ho compounds, respectively. The negative θ_p values obtained for all the compounds, hint at the predominance of antiferromagnetic (AFM) exchange interactions. Below 60 K, for all the compounds, $\chi^{-1}(T)$ deviate from the CW relationship due to magnetocrystalline anisotropy.

The insets in Figure 4.6 show the low-temperature $\chi(T)$ data. It is observed that $\chi(T)$ shows an anomaly characteristic of a putative long-range AFM phase transition for all three compounds at the Néel temperature T_N = 7.1, 8.5 and 3.7 K for the Nd, Dy and Ho compounds, respectively. The values of T_N were estimated at the shoulder of the $\chi(T)$ curve, as indicated by an arrow in the inserts of Figure. 4.6. It is observed that these values of T_N for all three compounds are relatively larger compared to the of T_N = 3.1 K [162], 4.5 K and 5.7 K [163] obtained for the equiatomic compounds NdCuGe, DyCuGe and HoCuGe single crystal, respectively. It can be suggested that this difference in T_N is due to the conduction electron-mediated RKKY interaction in RECuGa as a result of the difference in the number of conduction electrons in the Ga and Ge atoms (one for the Ga atom and two for the Ge atom). Below T_N the susceptibility decreases slightly and increases up to a value of 3.88 × 10^{-6} m^3/mol for Nd, while for the Dy and Ho compounds, $\chi(T)$ shows a tendency toward saturation at the lowest measured temperature of 1.7 K and attains the values of 9.333 × 10^{-6} for Dy and 23.334 × 10^{-6} m^3/mol for Ho. The ratio $\epsilon = \chi(1.7K)/\chi(TN) = 1.349$ for Nd, 1.001 for Dy and 0.988 for Ho compounds, respectively, contrast the behaviour expected for collinear AFM ordering (ϵ = 2/3) [164] and might give rise to speculation about noncollinear AFM spin arrangement in these compounds as reported in other rare-earth compounds such $GdPd_3$ [165]. Neutron diffraction experiments are required to authenticate such conjecture and determine the actual magnetic structure in these compounds.

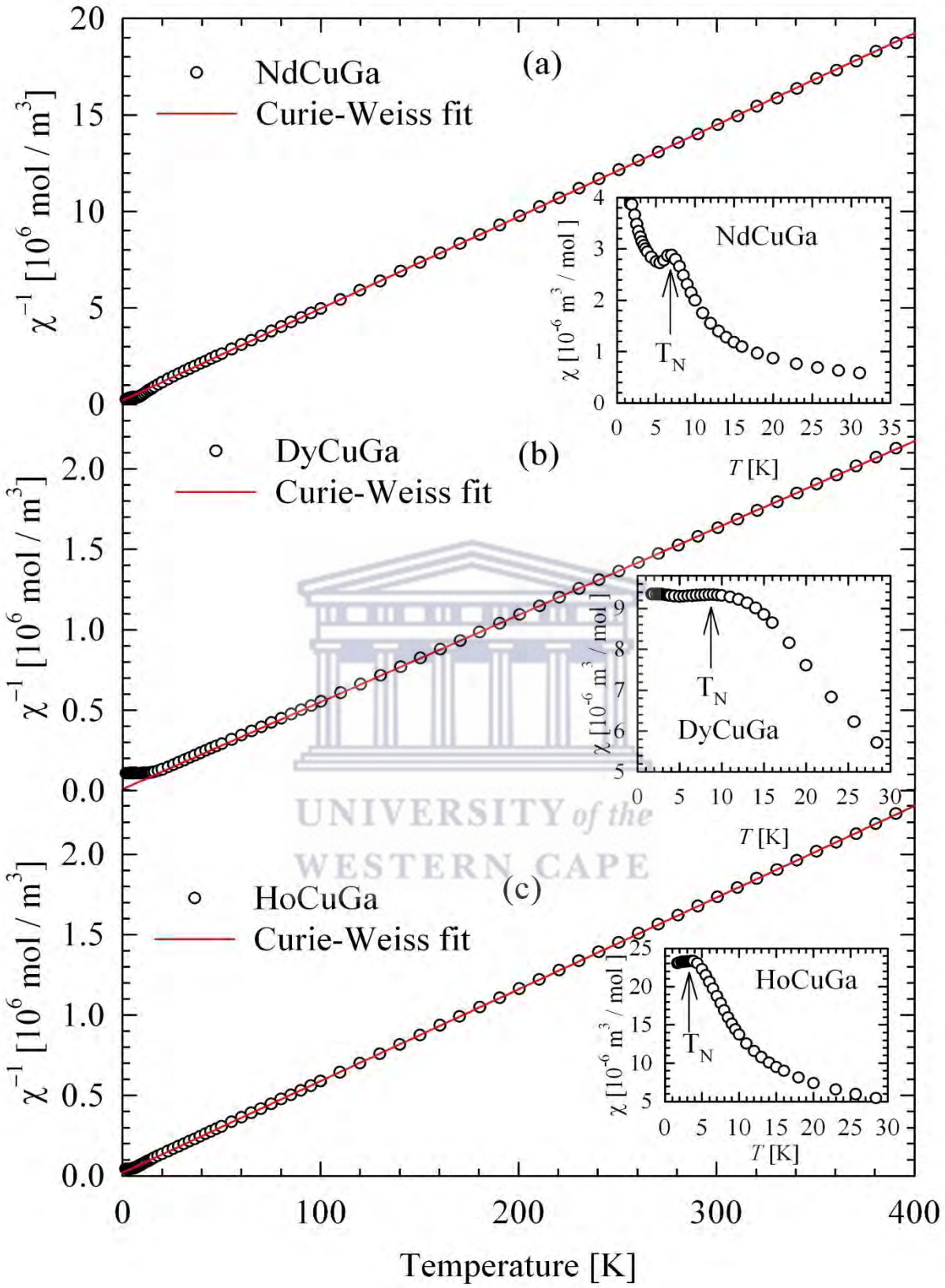

Figure 4.6: The inverse magnetic susceptibility, $\chi^{-1}(T)$ data of (a) NdCuGa, (b) DyCuGa and (c) HoCuGa compounds measured from 1.7 to 400 K in field of 0.1 T. The solid red lines represent the LSQ fit of the Curie-Weiss relationship (Eq. 4.1) to the measured data above 60 K. The insets display the low temperature, $\chi(T)$ with arrows indicating the magnetic phase transition temperature T_N.

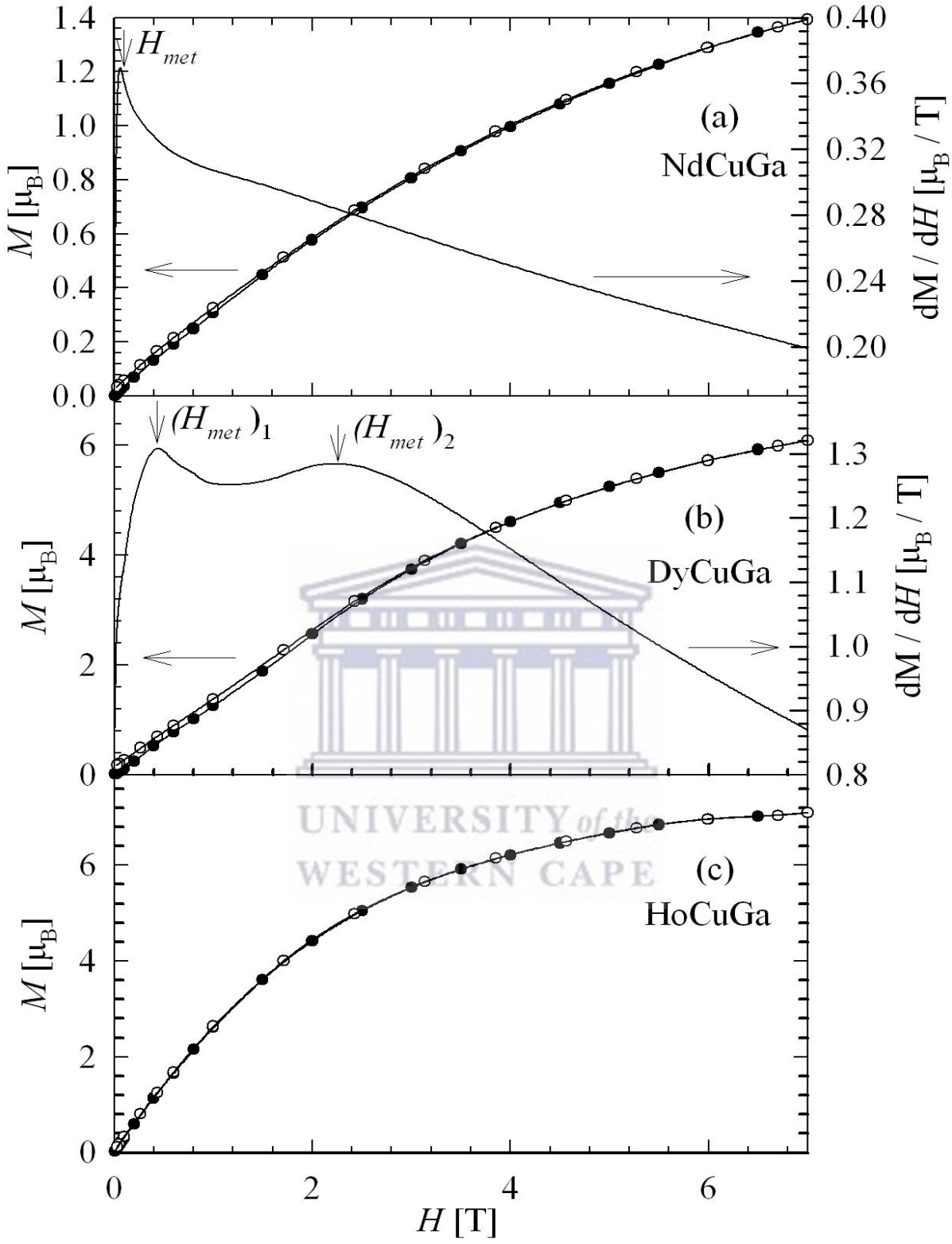

Figure 4.7: The field dependence of the, M (H) magnetization (left axis) measured at a temperature of 1.72 K in increasing (closed symbols) and decreasing (open symbols) field up to 7 T for (a) NdCuGa, (b) DyCuGa and (c) HoCuGa compounds. (a) and (b) (right axis) shows dM / dH with metamagnetic behaviours at low fields having one transition at H_{met} = 0.06 T for NdCuGa and two at H_{met} = 0.4 and 2.2 T for DyCuGa as indicated by arrows.

The field variation of the magnetization, $M(H)$ for RECuGa (where RE = Nd, Dy and Ho) measured at 1.72 K in increasing (closed symbols) and decreasing (open symbols) fields is shown in Figure. 4.7. As can be inferred from this figure, a small hysteresis is observed below 2 T during the process of increasing and decreasing field for both Nd and Dy compounds. Furthermore, metamagnetic behaviours are evident at low fields for the Nd and Dy compounds. One transition at H_{met} = 0.06 T for the Nd compound and two at H_{met} = 0.4 and 2.2 T for the Dy compound as indicated by arrows in Figure 4.7a and 4.7b (right axis). For all three compounds, initially $M(H)$ data increases continuously with field and exhibits a downward curvature up to 7 T. In the case of Ho compound, $M(H)$ data shows a tendency towards saturation above 7 T. The magnetization reaches the values of 1.393μ_B, 6.1 μ_B and 7.1 μ_B at 7 T for the Nd, Dy and Ho compounds, respectively. These values are somewhat smaller than their theoretical values for the trivalent RE (gJ = 2.72μ_B, 10.0μ_B and 10.34μ_B for Nd, Dy and Ho, respectively). In the present case of a polycrystalline sample in which the applied field is inevitably directed along arbitrary crystallographic directions in the sample, this shortfall may be explained by virtue of a magnetocrystalline anisotropy that requires higher fields to deconfine the magnetic moments from an easy axis of magnetization. Crystal electric field (CEF) are likely responsible for the anisotropy, but may themselves cause a splitting of the (2J+1) − fold degenerate manifold, which means that very high fields may be needed to obtain the complete magnetic moment of the entire multiplet.

4.4. Heat Capacity for NdCuGa

The low-temperature dependence of the heat capacity, $C_p(T)$ of NdCuGa is displayed in Figure 4.8. $C_p(T)$ shows an anomaly at T_N = 7 K that corresponds to the phase transition from the paramagnetic state to the AFM states as observed in the $\chi(T)$ data. Above T_N, $C_p(T)$ data can be described by the Debye relation:

$$\frac{C_P(T)}{T} = \gamma + \beta T^2, \tag{4.2}$$

where γ is the Sommerfeld coefficient and β is the phonon coefficient related to the Debye temperature, $\theta_D = (12R\pi^2 N/5\beta)^{1/3}$, R being the gas constant and N the number of atom per formula unit (N = 3). The LSQ fit of Eq. 4.2 to the experimental data (note the red line in the inset of Figure 4.10 left and bottom axis) yielded the parameters γ = 0.210(1) J/mol.K^2 and β = 0.00060(3) J/mol.K^3 which gives θ_D = 99(8) K. The obtained value of θ_D is slightly smaller

compared to those reported for other members of the RETX compounds [159, 166, 167]. The large value of γ originates from the free – electron of *s, p, d* and *f* subshells. Below T_N, $C_p(T)$ data decreases almost linearly with decreasing temperature, which might hint at a gapless spin-wave dispersion.

The total entropy $S\ (T)$ was calculated by integrating $C_p(T)/\ T$ and the result is presented in the inset of Figure 4.8 (right and top axis). It is observed that $S(T)$ attains the value of $R.ln2$ appropriate for a well isolated doublet ground state of Nd^{3+} ions, well above T_N at 14 K. The entropy release at T_N is about 3.1 J/(mol.K), which is considerably reduced by a factor of 0.54 compared to the value of $R.ln2$. Such a reduction was in some Ce based rare-earth compounds attributed to Kondo effect or short-range correlations above T_N [86, 88]. In the present Nd compound, such a reduction cannot be attributed to the Kondo effect. The observed entropy shifts to higher temperatures likely results from short-range correlations, signaled by an extended tail in $C_p(T)$ above T_N (see the main panel of Figure 4.8).

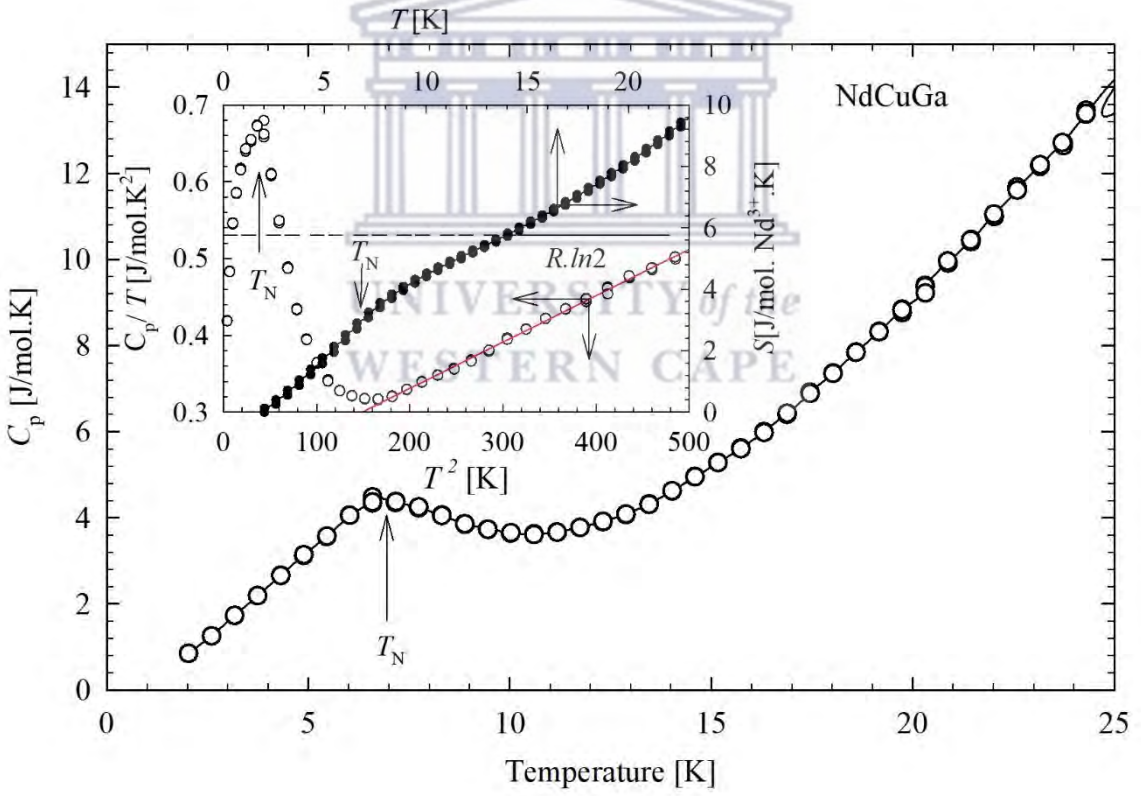

Figure 4.8: The low-temperature dependence of the heat capacity, $C_p(T)$ of NdCuGa measured in zero field. The inset displays the plot of $C_p(T)$ vs. T^2 (left and bottom axis) and the temperature dependence of the 4f - electron magnetic entropy, $S(T)$ (right and top axis) of NdCuGa. The solid red line in the inset is the LSQ fit of Eq. 4.2 to the experimental data. The vertical arrows indicate the position of T_N of NdCuGa and the horizontal dashed line marks the value *R.ln2*.

4.5. Isothermal magnetization and Magnetocaloric effect

The isothermal magnetization data *M* (*H, T*) in RECuGa (where RE = Nd, Dy and Ho) measured in applied magnetic field up to 7 T in the temperature range 2 – 30 K in steps of 2 K is displayed in Figure 4.9. *M* (*H, T*) data exhibit a linear behaviour up to 7 T above 14 K, 26 K and 20 K in the paramagnetic state for the Nd, Dy and Ho compounds, respectively. In the ordering region, *M* (*H, T*) curves for all three compounds are linear in weak magnetic fields and deviates from linearity with a downward curvature in strong fields. The values of the magnetization at 7 T decrease from 1.279 to 0.521 μ_B, 2.825 to 1.081 μ_B and 7.256 to 4.449 μ_B with increasing temperature for the Nd, Dy and Ho compounds, respectively. Such decrease of *M* (*H*, *T*) values at 7 T is probably due to the high – field FM state in these compounds.

The Belov - Arrott plots M^2 vs. $\frac{H}{M}$ from 2 to 30 K [168, 169] constructed for RECuGa (where RE = Nd, Dy and Ho) compounds from *M* (*H*, *T*) data are presented in Figure 4.10. Following Banerjee criterion [113], positive slopes for all isotherms indicate a second-order nature of the magnetic phase transition, while negative slopes of some isotherms indicate a first-order nature of the magnetic phase transition. It is observed from Figure 4.10 that, all isotherms for the Nd and Ho compounds exhibit positive slopes which hints to a second-order nature of the magnetic phase transition. Conversely, isotherms for the Dy compound show negative and positive slope below and above T_N, respectively, suggesting a first-order metamagnetic transition from AFM phase to a field-induced FM phase. In turn, the positive slopes appearing above T_N indicate a second – order nature of the magnetic phase transition. Similar behaviour was also observed for $NdPd_2Al_2$ compound (see chapter 3). Having looked at the magnetic properties, we now turn our attention to the calculations of the magnetocaloric effect in the next section.

Magnetocaloric effect (MCE) refers to the change in magnetic entropy, ΔS_M or the adiabatic temperature change, ΔT_{ad}. ΔS_M can be calculated from the magnetization isotherm based on the Maxwell thermodynamic relationship, Eq. 3.3 [170] while ΔT_{ad} can be calculated using the temperature dependence of ΔS_M and the results of the heat capacity measurement in zero magnetic field, Eq. 3.4 [171]. Figures 4.11(a) and 4.11(b) shows the temperature dependence of $-\Delta S_M$ and $\Delta T_{ad}(T)$, for various field changes of the Nd compound. Clearly, MCE is positive in the whole temperature range regardless of the magnetic field change, $\Delta(H)$. It is observed

that both $-\Delta S_M(T)$, and $\Delta T_{ad}(T)$ exhibit a peak located close to the Néel temperature T_N, for the Nd compound. Figures 4.12(a) and 4.12(b) show the temperature dependence of $-\Delta S_M$ for Dy and Ho compounds, respectively. As inferred in these figures, $-\Delta S_M$ exhibits a broad maximum well above their respective T_N values. Such broad maximum leads to a large value of the temperature taken at the full width at half maximum (δT_{FWHM}) as well as an enhanced value of the relative cooling power (*RCP*) (see Eq. 1.79). For all three compounds the magnitude of the maximum in $-\Delta S_M$ and ΔT_{ad} for Nd compound, gradually increases with rising $\Delta(H)$ and reaches a maximum value of $-\Delta S_M^{max}$: ΔT_{ad}^{max} = 1.40J/(kg.K) : 1.14 K, 5.53 J/(kg.K) : 5.29 K and 8.59 J/(kg.K) : 7.11K for $\Delta(H)$ = 2, 5 and 7 T, respectively in the case of Nd compound. For the Dy and Ho compounds, the values of the maximum entropy reaches are: $-\Delta S_M^{max}$ = 2.59 and 9.12 J/(kg.K) for $\Delta(H)$ = 2 T, 11.01 and 27.81 J/(kg.K) for $\Delta(H)$ = 5 T and 16.73 J and 37.11 J/(kg.K), for $\Delta(H)$ = 7 T, respectively. At 7 T, the values $-\Delta S_M^{max}$ of Dy and Ho are distinctly larger compared to the values $-\Delta S_M$ = 15 J/kg.K, 12.3 J/kg.K, and 12.7 J/kg.K reported for equiatomic compounds, DyCuGe, HoCuGe and ErCuGe, respectively [166]. It should be noted that these values of the maximum obtained for a magnetic field change of 5 and 7 T are similar to those reported for other members of the RETX series [140, 166, 167] as potential magnetic refrigerant materials (see Table 4.5).

Table 4.5: Values of $-\Delta S_M$, ΔT_{ad} and *RC* for a magnetic field change of 5 T of some RETX compounds.

Compound	$-\Delta S_M$[J/kg.K]	ΔT_{ad}[K]	*RC* [J/kg]	Ref.
NdCuGa	5.53	5.29	81.29	This work
DyCuGa	11.01	…	…	This work
HoCuGa	27.81	…	406.31	This work
GdScSi	2.5	…	93.3	[172]
GdScGe	3.3	…	88.9	[172]
TbTiGe	4.3	4.2	…	[173]
GdMnAl	0.69	…	59	[174]
ErFeSi	23.1	5.7	365	[175]
HoCuSi	20.5	3.1	410	[176]
HoPdIn	14.6	5.5	496	[177]
TbNiIn	5.3	…	191	[178]
GdCuSi	8	5.4	…	[179]

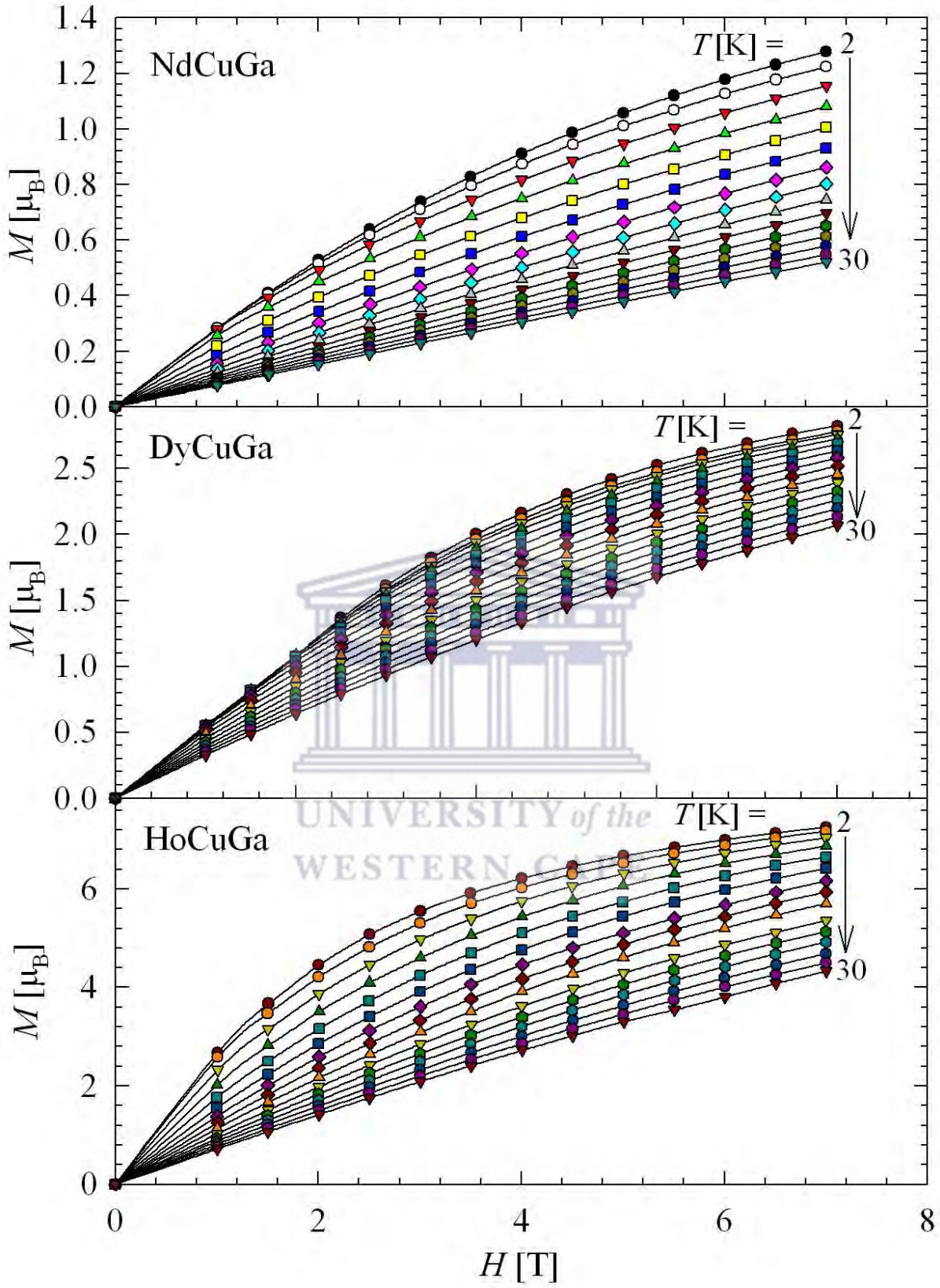

Figure 4.9: The isothermal magnetization M (H, T) of (a) NdCuGa, (b) DyCuGa and (c) HoCuGa measured in magnetic fields up to 7 T at different temperatures in the range $2K \leq T \leq 30K$ in steps of 2 K.

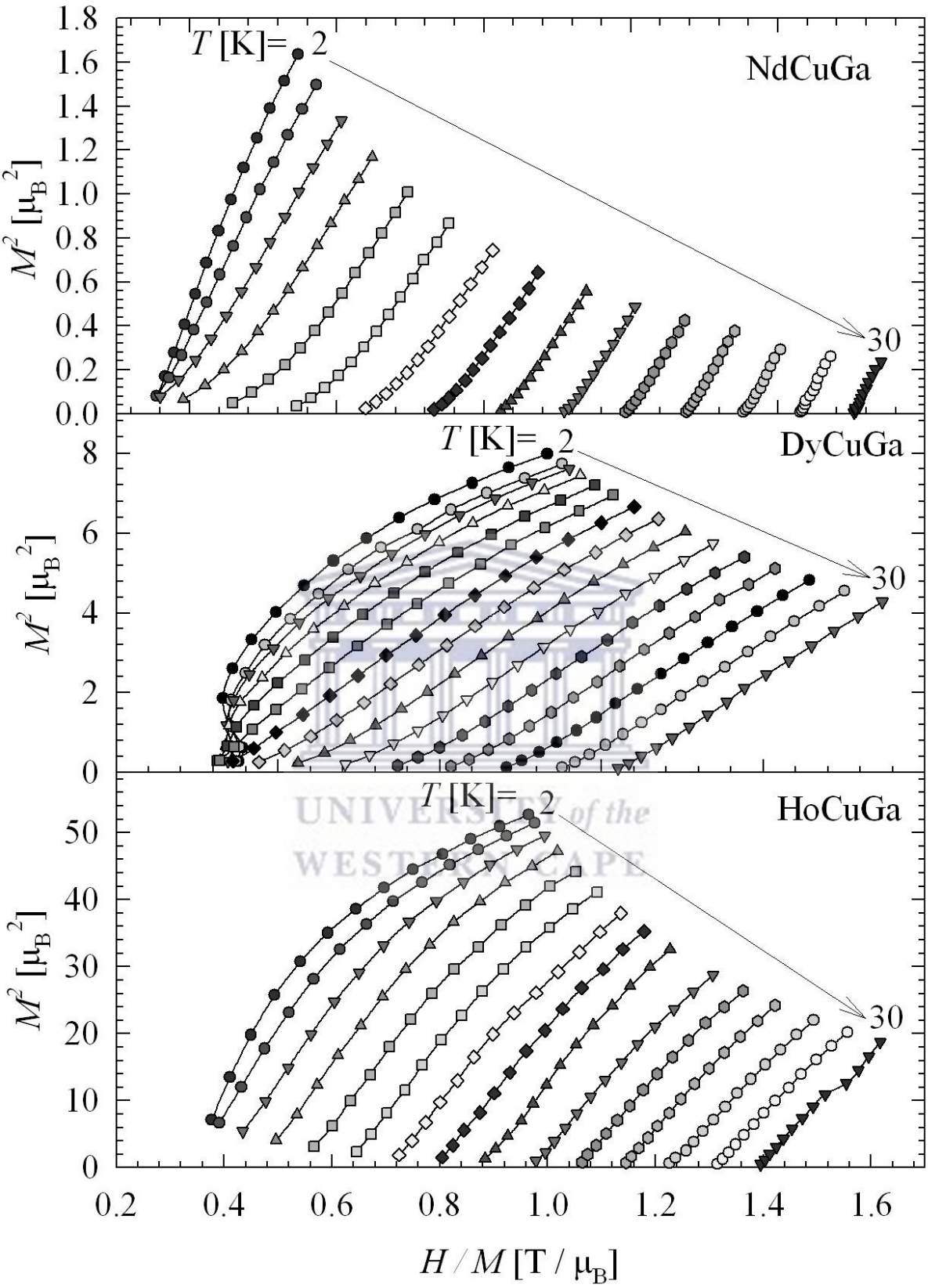

Figure 4.10. The Belov – Arrott plots, M^2 vs. H / M for (a) NdCuGa, (b) DyCuGa and (c) HoCuGa compounds.

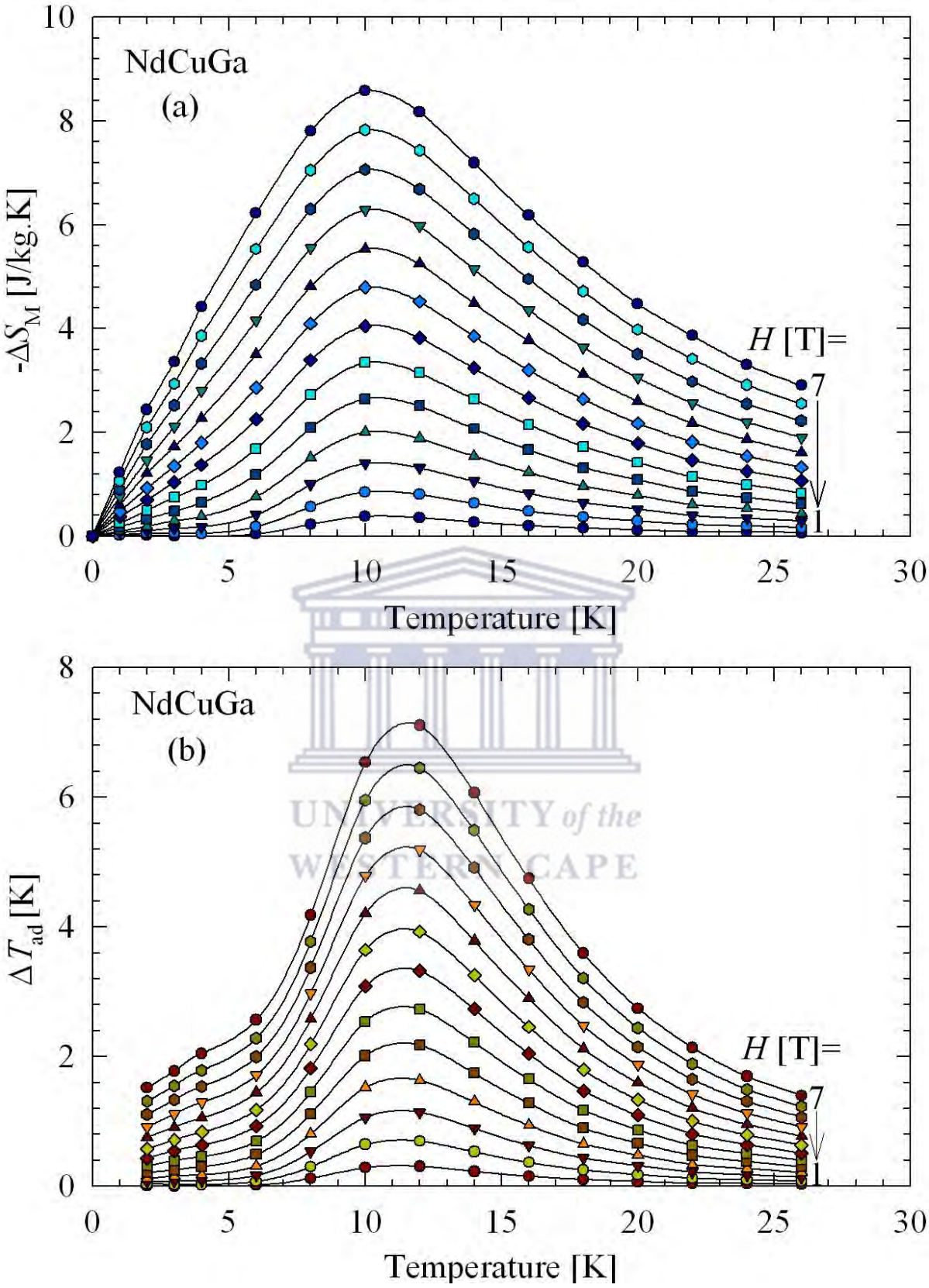

Figure 4.11: (a) Temperature dependencies of the isothermal entropy change, $-\Delta S_M(T)$, measured for NdCuGa with different field changes in steps of 0.5 T. (b) Temperature dependencies of the adiabatic temperature change, $\Delta T_{ad}(T)$ in NdCuGa derived for different magnetic field change in steps of 0.5 T.

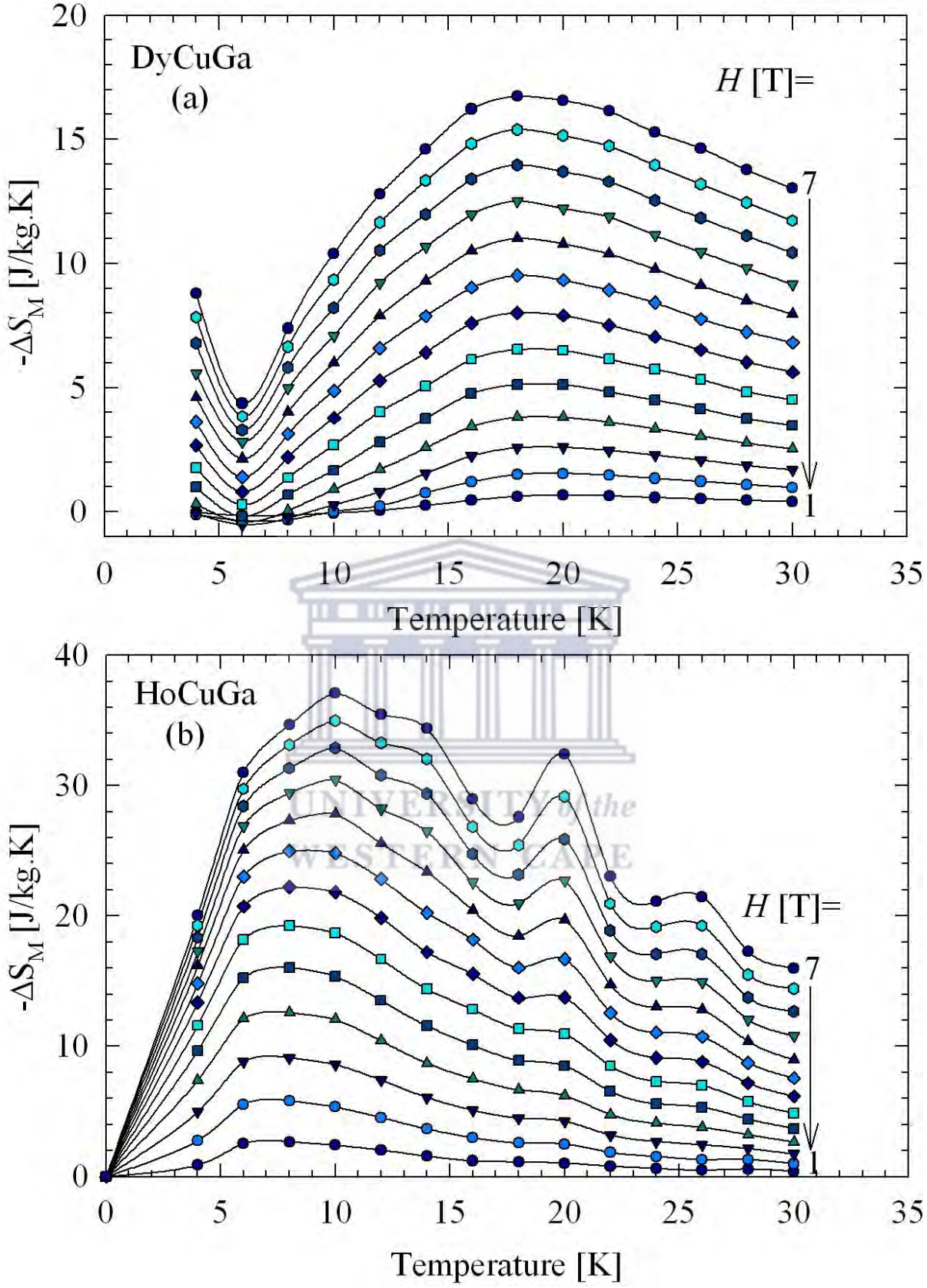

Figure 4.12: Temperature dependencies of the isothermal entropy change, $-\Delta S_M(T)$, measured for (a) DyCuGa and (b) HoCuGa with different field changes in steps of 0.5 T.

It is worthwhile noting that for magnetic materials with second-order transition, $-\Delta S_M^{max}$ usually follows the relation given by Eq. 3.5 [180]. Figures 4.13(a), 4.13(b) and 4.13(c) displays the plots of $-\Delta S_M^{max}$ vs. $h^{2/3}$ and the high field LSQ fit of Eq. 3.5 to the experimental data (solid line) for Nd, Dy and Ho compounds, respectively. The resulting parameters are $S(0,0) = 17.6(4), 41.4(6), 13.4(1)$ and $S(0,1) = -5.0(3), -9.1(3), -11.6(3)$ for Nd, Dy and Ho compounds, respectively. It should be noted that the negative value of $S(0,1)$ confirms the second-order nature of the magnetic phase transition in Nd, Dy and Ho compounds, while the high field linear behaviour of $-\Delta S_M^{max}$ indicate the strongly localized character of the Nd, Dy and Ho magnetic moments [181]. The isothermal field variation of MCE ($-\Delta S_M(T)$) is displayed in Figure 4.14 for RECuGa (with RE = Nd, Dy and Ho). As inferred in Figure 4.14, these compounds exhibit a quadratic dependence with field ($-\Delta S_M \propto (H)^2$). For the Nd and Dy compounds, this behaviour hints to the presence of spin fluctuation in the ordered region which is observed from NdCuSi, and in the paramagnetic region of the Ho compound as well as in other rare-earth compounds [126, 179].

From the point of view of applications, other important quality factors of magnetic refrigerant are the relative cooling power (*RCP*) and the refrigerant capacity (*RC*), being measures of heat transfer between cold and hot reservoirs in an ideal refrigeration cycle. The *RCP* and *RC* are defined in Eq. 3.6 and 3.7. The plots of *RCP* and *RC* are displayed in Figures 4.15(a) and 4.15(b) for different magnetic field changes. The values obtained for $\Delta(H)$ = 2, 5 and 7 T are listed in Table 4.6. It is observed from Figures 4.15(a) and 4.15(b) that both *RCP* and *RC* increase continuously with increase in $\Delta(H)$. The large values of *RCP* and *RC* result from both the spread of $-\Delta S_M$ over wide temperature range which leads to a large value of δT^{FWHM} and significant values of $-\Delta S_M^{max}$. The observed values of *RCP* and *RC* for Nd and Ho compounds are comparable and somewhat smaller than those other members of RETX family of compounds (see Table. 4.5) [140].

More recently, Smith *et al*. [182] reported that both figures of merit *RCP* and *RC* are based on a maximization approach that is not representative of practical applications. Furthermore, these figures of merit neglect the temperature change, which is as important as the entropy change for application.

Wood and Potter [127] put forward a more universal measure of refrigeration optimization that also takes into account the overall effort, not just network required to produce the refrigeration.

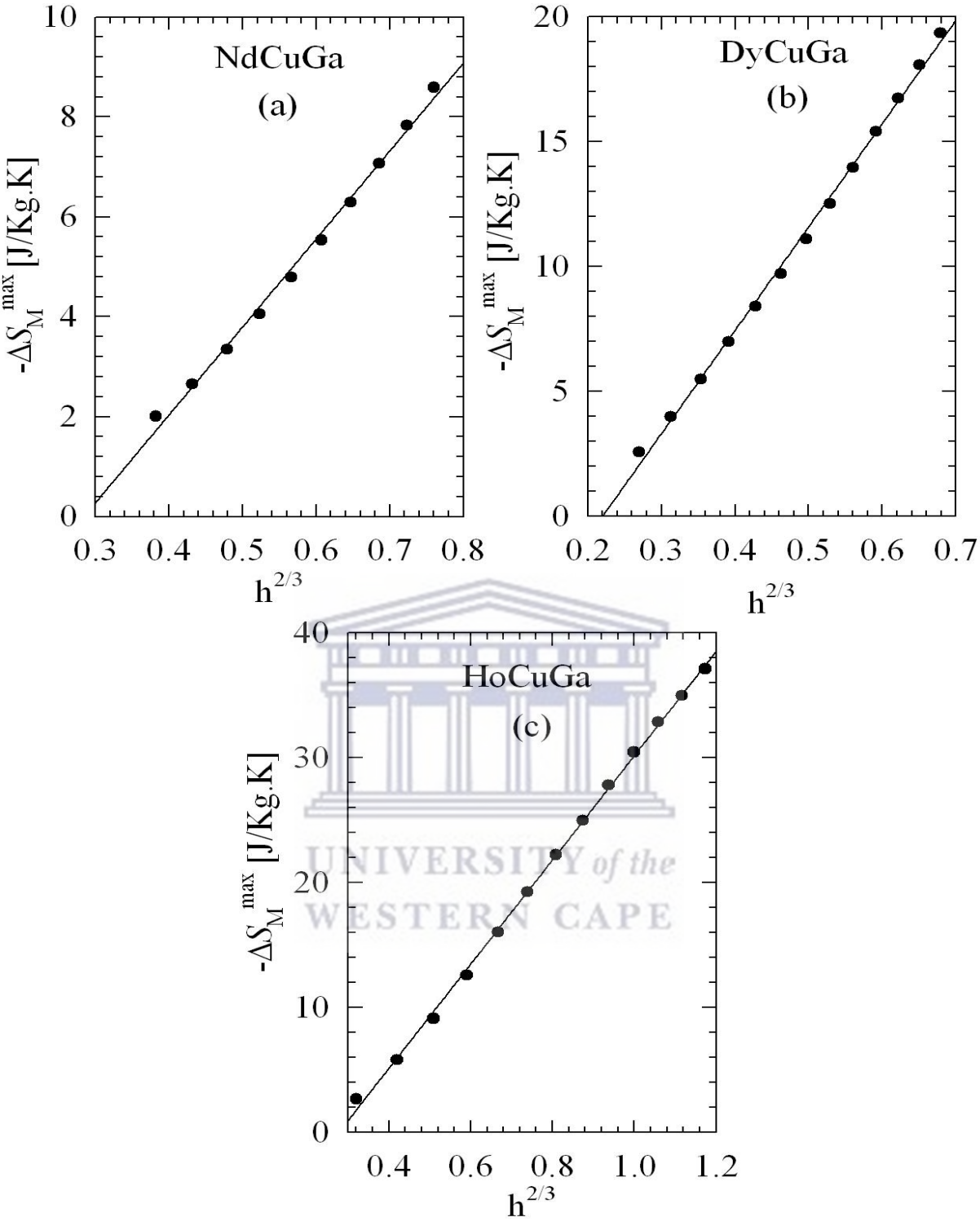

Figure 4.13: The maximum isothermal magnetic entropy change at T_N as a function of the reduced field $h^{2/3}$ (see text for the definition) for (a) NdCuGa, (b) DyCuGa and (c) HoCuGa.

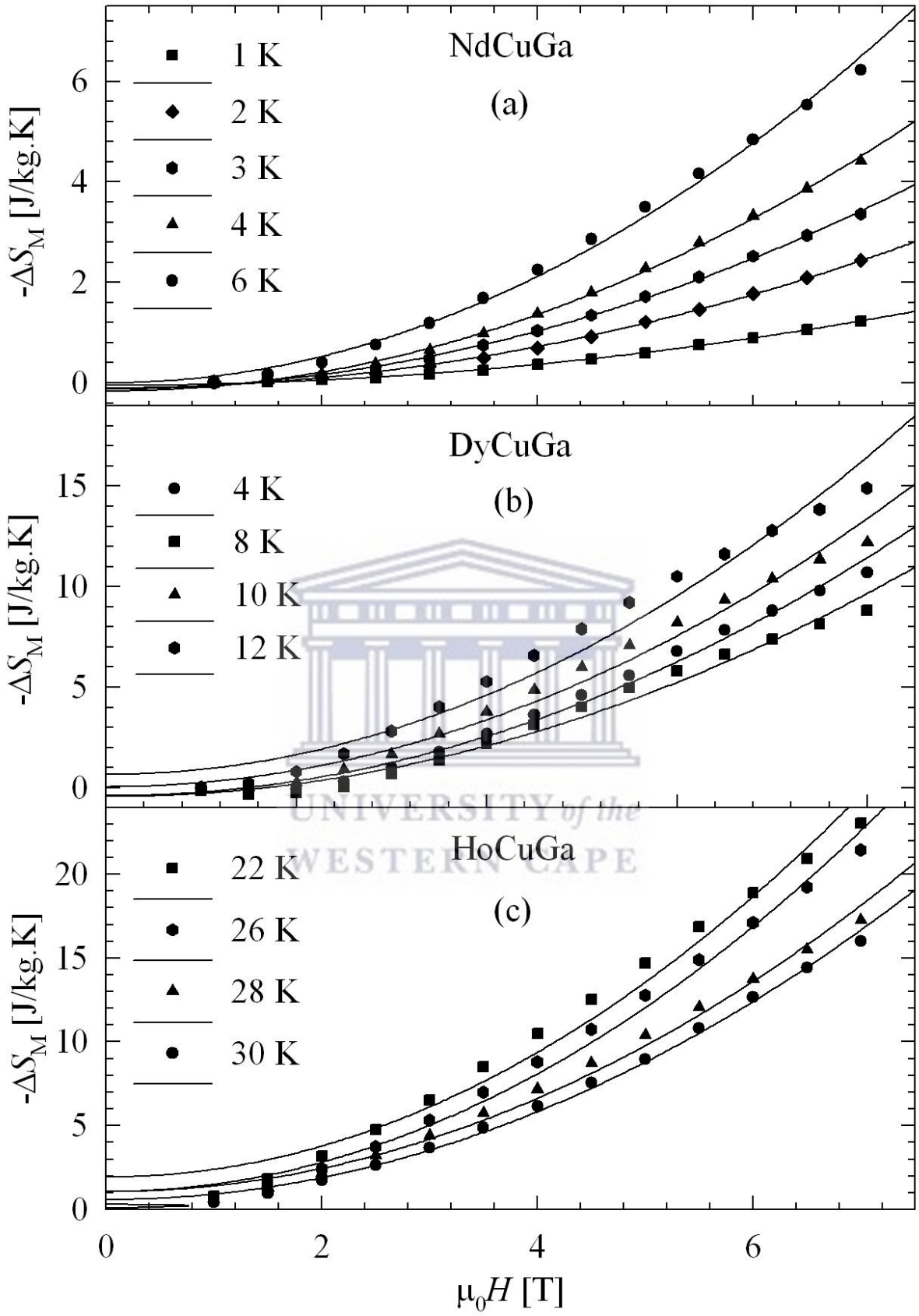

Figure 4.14. The isothermal field variation of $-\Delta S_M$ of (a) NdCuGa, (b) DyCuGa and (c) HoCuGa compounds.

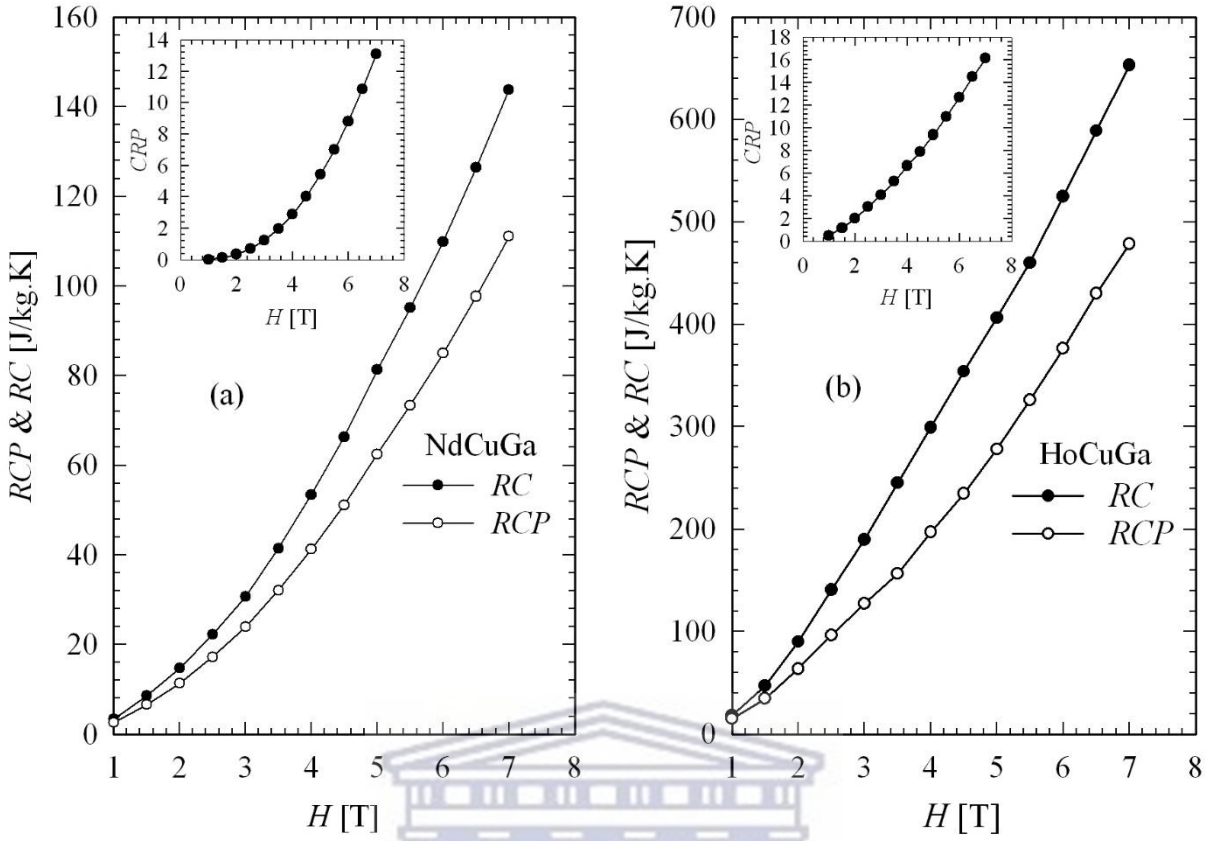

Figure 4.15: The relative cooling power (*RC*) (closed symbols) and the refrigerant capacity (*RCP*) (open symbols) for (a) NdCuGa and (b) HoCuGa compounds. The insets on (a) and (b) display their field variations of the coefficient of refrigerant performance (*CRP*).

This measure is the coefficient of refrigerant performance (*CRP*) defined in Eq. 3.8. Guillou *et al*. [80] suggest the use of $\Delta T = \Delta T_{ad}$ criterion for MCE materials based on a continuous transition since the maximization approach, $\Delta T = \delta T^{FWHM}$ criterion suggested by Wood and Potter will also lead to an overestimation of the performance of the materials similar to *RCP* and *RC*. In Eq. 3.8 the product $\Delta S_M^{max}.\Delta T_{ad}^{max}$ was used at the numerator as suggested by Guillou *et al*. [80] since the advantage of this is that it takes into account both the entropy change and the adiabatic temperature change. The magnetization isotherm at T_N = 7 K for the NdCuGa compound was estimated from the average of the magnetization isotherm at 6 K and 8 K while that of the Ho compound was estimated at 4 K close to its T_N = 3.7 K. Taking an account that the specific heat measurements were not done for HoCuGa, the product $\Delta S_M^{max}.\delta T^{FWHM}$ was used in Eq. 3.8.

The insets of Figures 4.15(a) and 4.15(b) shows the *CRP* curve for the Nd and Ho compounds, respectively. Similar to *RCP* and *RC*, *CRP* increases continuously with increasing magnetic

field change (see Table 4.6). These MCE data classified the Nd, Dy and Ho compounds as some possible candidate materials for application in magnetic refrigeration technology.

Table 4.6: Values of *RC*, *RCP* and *CRP* for a magnetic field change of 2, 5 and 7 T of NdCuGa and HoCuGa compounds.

Compound	ΔH (T)	*RC* [J/kg]	*RCP* [J/kg]	*CRP*
NdCuGa	2	14.66	11.34	0.34
	5	81.29	62.50	5.42
	7	143.84	111.10	13.11
HoCuGa	2	90.13	63.84	2.00
	5	406.31	278.14	9.38
	7	653.10	478.32	16.14

4.6. Summary

XRD results indicate that the RECuGa (where RE = Nd, Dy and Ho) compounds crystallize with an orthorhombic crystal structure of the $CeCu_2$ – type structure with space group *Imma*. Magnetic susceptibility and heat capacity results reveal that RECuGa (where RE = Nd, Dy and Ho) compounds order antiferromagnetically at T_N = 7.1, 8.5 and 3.7 K for Nd, Dy and Ho, respectively, while the Belov – Arrott plots indicate a second-order nature of the paramagnetic - AFM phase transition for all three compounds and a first–order metamagnetic transition from the AFM to a field–induced FM phase below T_N for DyCuGa. For the three compounds Nd, Dy and Ho, $\chi(T)$ data at high temperatures follows the Curie-Weiss law giving μ_{eff} close to that expected for the Nd^{3+}, Dy^{3+} and Ho^{3+} -ion and the negative values of the Weiss temperatures, θ_p confirming antiferromagnetic exchange interaction between the Nd, Dy and Ho moments. The MCE data indicate the possibilities of the three compounds as potential candidates for magnetic refrigeration technology in the low-temperature range.

CHAPTER 5

CONCLUSION AND OUTLOOK

The present Masters thesis addressed the study of crystal structure, transport, magnetic, magnetocaloric and thermodynamic properties of $NdPd_2Al_2$ and RECuGa (where RE = Nd, Dy and Ho) compounds. This study has been conducted with respect to both potential applications and fundamental questions in materials showing large MCE. This study has been successfully conducted through the measurements of electrical resistivity, magnetic susceptibility, magnetization and heat capacity. The electrical resistivity, magnetic susceptibility and heat capacity data have been used to investigate the phase transition for all the compounds studied, respectively. Magnetocaloric effect data has been estimated from the isothermal magnetization data for all the compounds studied, respectively.
The main conclusions are as follows:

XRD diffraction studies have confirmed the tetragonal $CaBe_2Ge_2$ - type crystal structure with space group *P4/nmm* (No. 129) for $NdPd_2Al_2$ compound. The low-temperature transport, magnetic and heat capacity studies, reveal that this compound exhibit AFM ordering below T_N = 3 K and that a relatively small magnetic field induces a transition from AFM to FM state that seems to bear a first-order character. Above T_N, $C_p(T)$ data of this compound is well described by the standard Debye relation with the Debye temperature θ_D = 253(3) K. $S(T)$ data shows entropy release at T_N amount to 2.77 J/mol.K, which corresponds to ca. 48% of the value of *R.ln2* expected for a well-isolated doublet ground state of Nd^{3+} ions. The high-temperature $\chi(T)$ data follows the modified Curie – Weiss (MCW) relation giving an effective magnetic moment value close to the theoretical value expected for Nd^{3+} - ion. A negative Weiss temperature θ_p was obtained for this compound, reflecting the predominance of a contribution of a ferromagnetic (FM) component to the AFM exchange interactions. The magnetic entropy change suggests spin fluctuation in the paramagnetic region and that the AFM phase transition in $NdPd_2Al_2$ has a second-order nature. The magnetization results indicate metamagnetic - like transition at low fields that bears a first-order character which corroborates the Belov - Arrott plots. The magnetization of this compound attains a value of 1.90 μ_B, at the highest measured field of 7 T.

Furthermore the magnitude of *RC* and *RCP* for H = 7 T classified $NdPd_2Al_2$ as a second - order MCE material. Obtained values of *RC / RCP* = 167.24 / 126.69 J/kg for ΔH = 7 T, respectively. Large values of MCE with maximum $-\Delta S_M^{max}$ = 16.53 J/kg.K and ΔT_{ad}^{max} = 9.41 K for a magnetic field changes of H = 7 T suggest that $NdPd_2Al_2$ compound is a potential candidate for magnetic refrigeration**.**

RECuGa (where RE = Nd, Dy and Ho) compounds have been characterized by X-ray diffraction, the result have confirmed the orthorhombic $CeCu_2$ - type structure with space group *Imma* (No. 74). $\chi(T)$ and $C_p(T)$ data show that RECuGa (where RE = Nd, Dy and Ho) compounds exhibit a putative antiferromagnetic (AFM) ordering below T_N = 7.1, 8.5 and 3.7 K for Nd, Dy and Ho, respectively. At high temperatures, $\chi^{-1}(T)$ data follow the paramagnetic Curie - Weiss behaviour with an effective magnetic moment, μ_{eff} = 3.658(2) μ_B, 10.850(2) μ_B and 10.568(4) μ_B for the Nd, Dy and Ho compounds, respectively. These values are reasonably close to the theoretical value of 3.62 μ_B expected for the free Nd^{3+} - ion, 10.65 μ_B expected for the free Dy^{3+} and 10.61 μ_B expected for the free Ho^{3+}. The LSQ fit parameters of $\chi(T)$ also yields the Weiss temperature θ_p = −4.4(3), −1.7(2) and −3.3(2) K for Nd, Dy and Ho, respectively. Above T_N the $C_p(T)$ data follow the Debye relation with the Debye temperature θ_D = 99(8) K for Nd compound, respectively. The temperature dependence of the 4f - electron magnetic entropy, $S(T)$ data show that, $S(T)$ attains the value of $R.ln2$ appropriate for a well-isolated doublet ground state of Nd^{3+} ions, well above T_N at 14 K for Nd compound. Just above T_N, $C_p(T)$ fitted to the Debye - relationship for Nd compound gave a Sommerfeld coefficient of : γ = 0.210(1) J/mol.K. The Belov - Arrott plots indicate a second-order nature of the magnetic phase transition for Nd and Ho compounds. For Dy compound the isotherms show negative and positive slope below and above T_N, respectively indicating a first-order metamagnetic transition from AFM phase to a field-induced FM phase. In turn, the positive slopes appearing above T_N indicating a second-order nature of the magnetic phase transition

The MCE investigated from the magnetic entropy change $(-\Delta S_M)$ and the adiabatic temperature change (ΔT_{ad}), gave the maximum values of both $-\Delta S_M$ and ΔT_{ad} to be 8.59 J/kg.K and 7.1 K for a field change of 7 T for NdCuGa. For Dy and Ho compounds, the magnitude of the maximum of $-\Delta S_M(T)$ were estimated to be 16.73 J/kg.K and 37.11 J/kg.K, for a field change of 7 T. The corresponding *RCP*, *RC* and the *CRP* obtained for $\Delta(H)$ = 7 T are: 143.84 J/kg, 111.10 J/kg and 13.11 J/kg for Nd, 653.10 J/kg, 478.32 J/kg and 16.14 J/kg

for Ho respectively. These figures are similar to those reported for materials that can be used as magnetic refrigerants.

It is hoped that this work may act as a foundation for further research in the development of new materials that can fulfil specific requirements of cooling devices. Future works may include:

Measurements such as neutron diffraction experiments, which are required to verify and to determine the actual magnetic structure of the $NdPd_2Al_2$ and RECuGa (where RE = Nd, Dy and Ho) compounds.

Measurements of thermal transport properties for $NdPd_2Al_2$ and RECuGa (where RE = Nd, Dy and Ho) compounds, where these measurements involve, thermal conductivity, thermoelectric power and the Lorentz number, will contribute additional information.

Measurements of electrical resistivity for the RECuGa (where RE = Nd, Dy and Ho) compounds to verify the AFM order.

BIBLIOGRAPHY

[1] https://www.epa.gov/sustainability/learn-about-sustainability/#what. United States Environmental Protection Agency. 10.18.2017. Accessed 25 March 2017.

[2] J. U. Ahmed, R. Saidur, H. H. Masjuki, Renew. Sust. Energ. Rev. **15** (2011) 1593.

[3] Xi Hongxia, Luo Lingai, Fraisse Gilles. Renew. Sust. Energ. Rev. **11** (2007) 923.

[4] M. I. Karamangil, S. Coskun, O. KaynakliN. A. Yamankaradeniz. Renew. Sust. Energ. Rev. **14** (2010) 1969.

[5] X. Q. Zhai, M. Qu, Wang Yue, R. Z. Li. Renew. Sust. Energ. Rev. **15** (2011) 4416.

[6] B. Choudhury, P. K. Chatterjee, J. P. Sarkar, Renew. Sust. Energ. Rev. **14** (2010) 2189.

[7] V.K. Pecharsky, K.A.Gschneidner Jr. Phys. Rev. Lett. **78** (1997) 4494.

[8] T. Krenke, E. Duman, M. Acet, E.F. Wassermann, X. Moya, L. Maňosa, A. Planes. Nat. Mat. **4** (2005) 450.

[9] F. Guillou, G. Pocari, H. Yibole, N. van Dijk, E.Brück, Adv. Mater. **26** (2014) 2671.

[10] C.L. Zhang, D.H. Wang, Q.Q CaoZ.D. Han, H.C. Xuan, Y.W. Du, Appl. Phys. Lett. **93** (2008) 122505.

[11] A. Fujita, S. Fujieda, Y. Hasegawa, K. Fukamichi, Phys. Rev. B **67** (2003)104416.

[12] https://pdfslide.net/documents/springer-theses-rare-earth-elements-rare-earth-elements-what-and-where.html. Accessed 18 May 2019.

[13] Röhr C (2011) Chemie der Metalle, Kap. 7.1: Vorlesung. Online Skript. Retrieved from http://ruby.chemie.uni-freiburg.de/Vorlesung/metalle_7_1.html. Accessed 18 May 2019.

[14] Available online: https://www.liverpool.ac.uk/~sdb/Research/Chapter1.pdf. Accessed 18 May 2019.

[15] K.H.J. Buschow, Rep. Prog. Phys. **40** (1977) 1179.

[16] C. Huang and Z. Bian, *Rare Earth Coordination Chemistry: Fundamentals and Applications*, John Wiley & Sons, (2011) p.1, 2.

[17] H.F. Spedding. "The Rare Earths", eds. H.F. Spedding and A.H. Daane, Wileyj.: New York, (1961).

[18] S.H. Liu, Phys. Rev. **121** (1961) 451; R.E. Watson and A. J. Freeman, Phys. Rev. **152** (166) 566.

[19] K. H. J. Buschow and F. R. de Boer, *Physics of Magnetism and Magnetic Materials*, (2003).

[20] http://hyperphysics.phy-astr.gsu.edu/hbase/quantum/Lande.html#c2, 18 August 2019

[21] P. Langevin, J. Phys. Theor. Appl. **4** (1905) 165-313.

[22] http://www.irm.umn.edu/hg2m/hg2m_b/hg2m_b.html. Accessed 26 March 2019.

[23] S. Blundell, *Magnetism in Condensed Matter*, Oxford University: Oxford University Press, (2006).

[24] C. Kittel, *Introduction to solid state physics*. 7th ed *New York: Wiley*, (1996).

[25] M. Ali. Omar, *Elementary Solid State Physics: Principles and Applications*, Addison-Wesley series in solid state sciences, (1975).

[26] https://en.wikipedia.org/wiki/Antiferromagnetism. Accessed 26 March 2019.

[27] Spaldin, Nicola A. *"9. Ferrimagnetism". Magnetic materials: fundamentals and applications* (2nd ed.). Cambridge: Cambridge University Press, (2010) pp. 113−129.

[28] L Néel, Ann. Phys-Paris. **3** (1948) 137−198.

[29] C. D. Stanciu, A. V. Kimel, F. Hansteen, A. Tsukamoto, A. Itoh, A. Kirilyuk, and Th. Rasing, Phys. Rev. B **73** (2006) 220402(R).

[30] R. G .Chamber, *Electron in Metals and Semiconductors*, Chapman and Hall: London, (1990).

[31] J. M. Ziman, *Electron and Phonons*, Oxford University Press: London, (1965).

[32] F. J. Blatt, *Physics of Electronic Conduction in Solids*, McGraw – Hill: New York, (1968).

[33] K. Ikeda, S. K. Dhar, M. Yoshizawa and K. A. Jr. Gschneidner, J. Magn. Mater. **100** (1991) 292.

[34] G. T. Meaden, *Electrical Resistance of Metals*, Plenum press: New York, (1965).

[35] E. Gratz and M. J. Zuckermann, *Handbook on Physics and Chemistry of the Rare Earths*, eds Gschneider K. A. Jr., and Eyring L.,Northern−Holland: Amsterdam, **Vol. 5**, chap. 42 (1982) 117.

[36] T. Kasuya, Prog. Theor. Phys. **16** (1956) 45.

[37] P.G. de Gennes and J. Friedel, J. Phys. Chem. Solids **4** (1958) 71.

[38] A. J. Dekker, J. Appl. Phys. **36** (1965) 906.

[39] S. V. Vonsovski, Izvestiya Akademii Nauk SSR, Seriya Fizicheskaya **19** (1955) 426.

[40] T. Kasuya, Prog. Theor. Phys. **22** (1959) 227.

[41] I. Mannari, Prog. Theor. Phys. **22** (1959) 335.

[42] M. Lavagna, C. Lacroix and M. Cyrot, J. Phys. F: Met. Phys. **13** (1983) 1007.

[43] J. Larrea, M. Fonte, E. Baggio-Saitovitch, M. Eichler, M. M.Abd-Elmeguid, C. Geibel and M. Contenentino, J. Phys. Soc. **76** (2007) 156.

[44] J. Larrea, M. Eichler, M. Fonte, E. Baggio-Saitovitch and M. Contenentino, Solid State Commun. **144** (2007) 488.

[45] R.J. Elliott and F.A. Wedgwood, Proc. Phys. Soc. **81** (1963) 846.

[46] H. Miwa, Prog. Theor. Phys. **28** (1962) 208.

[47] H. Miwa, Prog. Theor. Phys. **29** (1963) 4466.

[48] H. Yamada and S. Takada, Prog. Theor. Phys. **52** (1974) 1077.

[49] M. A. White, *Physical Properties of Materials*, 2nd ed (2012).

[50] http://en.wikipedia.org/wiki/Electron_heat_capacity. Accessed 10 June 2019.

[51] V.K. Anand, D.C. Johnston, J. Phys. Condens. Matter. **25** (2013) 196003.

[52] A. M. Tishin and Y. I. Spichkin, *The magnetocaloric effect and its applications*. Institute of physics: Bristol, (2003) p.2.

[53] K. A. Gschneidner, Jr. and V. Pecharsky, Int. J. Refrig. **31** (2008) 945.

[54] K. A. Gschneidner, Jr., V. K. Pecharsky, and A. O. Tsoko, Rep. Prog. Phys. **68** (2005) 1479.

[55] B. G. Shen, J. R. Sun, F. X. Hu, H. W. Zhang, and Z. H. Cheng, Adv. Mater. **21** (2009) 4545.

[56] V. Franco, J. S. Blazquez, B. Ingale, and A. Conde, Annu. Rev. Mater. Res. **42** (2012) 305.

[57] Ling – Wei Li, Chin. Phys. B **25** (2016) 037502.

[58] A. M. Tishin, J. Magn. Magn , Mater. **316** (2007) 68.

[59] O. Tegus, E. Brück, K. H. J. Buschow, and F. R. de Boer, Nature (London). **415** (2002) 150.

[60] F. Hu, B. Shen, J. Sun, Z. Cheng, G. Rao, X. Zhang, Appl. Phys. Lett. **78** (2001) 3675.

[61] F. Hu, B. Shen, J. Sun, Appl. Phys. Lett. **76** (2000) 3460.

[62] J. Marcos, A. Planes, L. Mañosa, F. Casanoa, X. Batlle, A. Labarta, B. Martinez, Phys. Rev. B **66** (2002) 224413.

[63] Z. B. Guo, Y. W. Du, J. S. Zhu, H. Huang, W. P. Ding and D. Feng. Phys. Rev. Lett. **78** (1997) 1142.

[64] X.X. Zhang, J. Tejada, Y. Xin, G.F. Sun, K.W. Wong and X. Bohigas, Appl. Phys. Lett. **69** (1996) 3596.

[65] L. Li et al, Appl. Phys. Lett. **107** (2015) 132401.

[66] Y. K. Zhang, G. Wilde, X. Li, Z. Ren & L. Li, Intermetallics. **65** (2015) 61.

[67] L. W. Li et al, Appl. Phys. Lett. **100** (2012) 152403.

[68] Y. J. Ke, X. Q. Zhang, Y. Ma and Z. H. Cheng, Sci. Rep. **6** (2016) 19775.

[69] J. C. B. Monteiro, R. D. dos Reis and F. G. Gandra, Appl. Phys. Lett. **108** (2015) 194106.

[70] L. Li, and K. Nishimura, Appl. Phys. Lett. **95** (2009) 132505.

[71] D. Jang et al, Sci. Rep. **6** (2015) 8680.

[72] V. Franco, J. S. Blázquez, J. J. Ipus, J. Y. Law, L. M. Moreno-Ramírez, A. Conde, Prog. Mater. Sci. **93** (2018) 112-232.

[73] V.K. Pecharsky and K.A. Gschneidner, Jr., J. Appl. Phys. **86** (1999) 565-575.

[74] V. K. Pecharsky, K. A. Gschneidner, Jr., A. O. Pecharsky, and A. M. Tishin Phys. Rev. B **64** (2001) 144406.

[75] M.E. Wood and W.H. Potter. Cryogenics. **25** (1985) 667-683.

[76] V.K. Pecharsky and K.A. Gschneidner, Jr., J. Appl. Phys. **90** (2001) 4614.

[77] A. Smith, C. R. H. Bahl, R. Bjork, K. Engelbrecht, K. K. Nielsen and N. Pryds, Adv. Energy Mater. **2** (2012) 1288.

[78] K. A Gschneidner Jr, V. K Pecharsky, Ann. Rev. Mater. Sci. **30** (2000) 387.

[79] K. Engelbrecht and C. R. H. Bahl. J. Appl. Phys. **108** (2010) 123918.

[80] F. Guillou, H. Yibole, G. Porcari, L. Zhang, N. H. Van Dijk and E. Bruck, J. Appl. Phys. **116** (2014) 063903.

[81] R.A. Young, *The Rietveld method,* International union of crystallography, New York: Oxford University Press: New York, **Vol. 5** (1993).

[82] J. Durbin and G.S. Watson, Biometrika, **58** (1971) 1.

[83] R.J. Hill and H.D. Flack, J. Appl. Crystallogr. **20** (1987) 356.

[84] J. Shang Hwang, K. Jan Lin, and C. Tien. Rev. Sci. Instrum. **68** (1997).

[85] P. Rogl, *Handbook on the physics and chemistry of rare earths*, ed. K. A. Gschneidner Jr and L. Eyring **Vol.7**, chap.51 (1984) p.1.

[86] M. Klicpera, P. Dolezal, J. Prokleska, J. Prchal, P. Javorsky, J. Alloys Compds. **639** (2015) 51−59.

[87] M. Klicpera, J. Pasztorova, P. Javorsky, Supercond. Sci. Technol. **27** (2014) 085001.

[88] A. Tursina, E. Khamitcaeva, A. Gribanov, D. Gnida, D. Kaczorowski, Inorg. Chem. **54** (2015) 3439−3445.

[89] M. Klicpera, M. Boehm, P. Dolezal, H. Mutka, K. M. M., S. Rols, D. T. Adroja, I. Puente Orench, J. Rodriguez-Carvajal, P. Javorsky, Phys. Rev **B. 95** (2017) 085107.

[90] L. C. Chapon, E. A. Goremychkin, R. Osborn, B. D. Rain-ford, S. Short, Physica B **378-380** (2006) 819−820.

[91] J. Kitagawa, M. Ishikawa, J. Phys. Soc. Jpn **68** (1999) 2380−2383.

[92] W.M. Williams, R.T. Macaluso, D.P. Young, J.Y. Chan, Inorg Chem. **42** (2003) 7315-7318.

[93] A. Z. Mewis, Anorg. Allg. Chem. **7** (1986) 536.

[94] J. Kitagawa, M. Ishikawa, J. Phys. Soc. Jpn. **68** (1999) 2380.

[95] C. Kranenberg, D. Johrendt, A. Mewis, R. Pottgeb, G. Kotzyba, H. Trill, B.D. Mosel. J.Solid State Chem. **167** (2002) 107.

[96] K. Hiebl, P. Rogl, J. Magn. Magn. Mater. **50** (1985) 39−48.

[97] D. Gignoux, D. Schmitt, D. Zerguine, C. Ayache, E. Bonjour, Phys. Lett. A **117** (1986) 145−149.

[98] C. Ayache, J. Beille, E. Bonjour, R. Calemczuk, G. Creuzet, D. Gignoux, A. Najib, D. Schmitt, J. Voiron, M. Zerguine, J. Magn. Magn. Mater. **63/64** (1987) 329−331.

[99] R. M. Marsolais, C. Ayache, D. Schmitt, A. K. Bhattachar-jee, B. Coqblin, Anisotropic resistivity of $CePt_2Si_2$, J. Magn. Magn. Mater. **76/77** (1988) 269−271.

[100] F. Steglich, J. Aarts, C. D. Bredl, W. Lieke, D. Meschede, W. Franz, J. Shafer, Phys. Rev. Lett. **43** (1979) 1892.

[101] F. M. Grosche, S. R. Julian, N. D. Mathur, G. G. Lonzarich, Physica **B 225−224** (1996) 5052.

[102] M. B. Tchoula Tchokonte, P. d. V. du Plessis, D. Kaczorowski, J. Phys.: Condens. Matter. **15** (2003) 3767−3777.

[103] M. B. Tchoula Tchokonte, Z. M. Mahlubi, A. M. Strydom, D. Kaczorowski, J. Alloys Compds. **696** (2017) 1004−1009.

[104] I. Sheikin, Y. Wang, F. Bouquet, P. Lejay and A. Junod, J. Phys.: Condens. Matter. **14** (2002) L534 – L549.

[105] J. Pierre, K. Kaczmaska, R.V. Skolozadra, S. Alebarski, J. Magn. Magn. Mater. **140** (1994) 891.

[106] Q.Y. Dong, B.G. Shen, J. Chen, J. Shen, and J.R. Sun, J. Appl. Phys. **105** (2002) 094402.

[107] X.X. Zhang, F.W. Wang, and G.H. Wen, J. Phys.: Condens. Matter. **13** (2001) L747.

[108] D. C. Johnston, Phys. Rev. Lett. **109** (2012) 077201.

[109] D. C. Johnston, Phys. Rev. B **91** (2015) 064427.

[110] A. Pandey, C. Mazumdar, R. Ranganathan, D. C. Johnston, Sci. Rep. **7** (2017) 42789.

[111] K. P. Belov, *Magnetic transition, Consultant Bureau*, ed. New York, (1961).

[112] S. A. Nikitin, T. I. Ivanova, Y. S. Koshkid'ko, J. Cwik, K. Rogacki, Acta Mater. **161** (2018) 331.

[113] B. K. Banerjee, Phys. Lett. **12** (1964) 16.

[114] A. H. Morrish, *The physical principles of magnetism*, Wiley Online Library: New York, (1965).

[115] E. Brück, J. Phys. D: Appl. Phys. **38** (2005) R381.

[116] L. W. Li, T. Namiki, D. Huo, Z. Qian, K. Nishimura, Appl. Phys. Lett. **103** (2013) 222405.

[117] P. Kumar, N. K. Singh, K. G. Suresh, A. K. Nigam, Phys. Rev. B **78** (2008) 184411.

[118] M. S. Kim, N. H. Sung, Y. Son, K. Ko, M. S. and Cho, Appl. Phys. Lett. **98** (2011) 172509.

[119] L. Li, K. Nishimura, M. Kadonaga, Z. Qian, D. Huo, J. Appl. Phys. **110** (2011) 043912.

[120] Q. Y. Dong, B. G. Shen, J. Chen, J. R. Sun, Appl. Phys. **105** (2009) 113902.

[121] Q. Y. Dong, H. W. Zhang, J. L. Shen, , J. R. Sun, B. G. Shen, J. Magn. Magn. Mater. **309** (2007) 56.

[122] Q. Y. Dong, H. W. Zhang, J. R. Sun, B. G. Shen, V. Franco, J. Appl. Phys. **103** (2008) 116101.

[123] J. Shen, L. Q. Yan, H. W. Zhang, F. W. Wang, J. R. Sun, F. X. Hu, C. B. Rong, X. Y. Li, J. Appl. Phys. **103** (2008) 07B315.

[124] S. Gupta, K. G. Suresh, A. Das, A. K. Nigam, A. Hoser, Appl. Phys. Lett. **3** (2013) 066102.

[125] S. Gupta, R. Rawat, K. G. Suresh, Appl. Phys. Lett. **105** (2014) 012403.

[126] K. A. Gschneidner Jr., V. K. Pecharsky, A. O. Tsokol, Rep. Prog. Phys. **68** (2005) 1479.

[127] M. E. Wood, W. H. Potter, Cryogenics. **25** (1985) 667.

[128] Y. Zhang, Review of the structural, J. Alloys Compds. **787** (2019) 1173−1186.

[129] A. Smith, R. H. Bahl, R. Bjork, K. Engelbrecht, K. K. Nielson, N. Pryds, Adv. Energy Mater. **2** (2012) 1288.

[130] S. Gupta, K. G. Suresh, A. V. Lukayanov, J. Mat. Sci. **50** (2015) 5723.

[131] S. Gupta, K. G. Suresh, A. K. Nigam, Y. Mudryk, D. Paudyal, V. K. Pecharsky, K. A. Gschneidner Jr, J. Alloys Compds. **613** (2014) 280.

[132] S. Gupta, K. G. Suresh, A. K. Nigam, J. Appl. Phys. **112** (2012) 103909.

[133] S. Tence, E. Gaudin, O. Isnard, B. Chevalier, J. Phys.: Condens. Matter. **24** (2012) 296002.

[134] Y. K. Zhang, Y. Yang, C. Hou, D. Guo, X. Li, Z. Ren, G. Wilde, Intermetallics. **94** (2018) 17e21.

[135] X. Dong, J. Feng, Y. Yi, L. Li, J. Appl. Phys. **124** (2018) 093901.

[136] Y. K. Zhang, D. Guo, S. H. Geng, X. G. Lu, G. Wilde, J. Appl. Phys. **124** (2018) 043903.

[137] R. Pöttgen and B. Chevalier, Z. Naturforsch. **70b** (2015) 289

[138] O. Janka et al., Z. Naturforsch. **71b** (2016) 737.

[139] R. Pöttgen Z. Naturforsch. **71(3)b** (2016) 165.

[140] S. Gupta and K. G. Suresh, J. Alloys Compds. **618** (2015) 562.

[141] S. Gupta, K. G. Suresh, A. K. Nigam, Yu V. Knyazev, Yu I. Kuz'min and A. V. Lukoyanv, J. Phys. D: Appl. Phys. **47** (2014) 365002.

[142] B. J. Gibson, W. Schnelle, R. Pöttgen, K. Bartkowski and R. K. Kremer, in: Porc. of Int. Conf. on Low Temp. Phys., Prague, August 8 - 14, (1996).

[143] B. Chevalier, M. Pasturel, J. L. Bobet, F. Weill, R. Decourt and J. Etourneau, J. Solid State Chem. **177** (2004) 752.

[144] D. Gignoux, D. Schmitt and M. Zerguine, Sold State Commun. **58** (1986) 559.

[145] F. M. Mulder, R. C.Thiel and K. H. J. Buschow, J. Alloys Compds. **205** (1994) 169.

[146] A. Szytula, W. Bazela and J.Leciejewicz, Solid State Commun. **56** (1985) 1043.

[147] S. Baran, I. Leciejewicz, N. St¨usser, A. Szytula, Z. Tomkowicz and A. Zygmunt, Acta Phys. Pol. A **56** (1997) 271.

[148] B. M. Sondezi and A. M. Strydom, Acta Phys. Pol. A **127** (2015) 288.

[149] E. Gratz, E. Bauer, B. Barbara, S. Zemirli, F. Steglich, C. D. Bredl and W. Lieke, J. Phys. F **15** (1985) 1975.

[150] C. D. Bred, J. Magn. Magn. Mater. **63-64** (1987) 355.

[151] Y. Onuki, A. Fukuda, I. Uken, I. Umehara, K. Satoh, I. Uken, I. Umehara, K. Satoh and Y. Kurosawa, Physica B **163** (1990) 600.

[152] Y. Onuki, Y. NaKai, T. Oomi, T. Yamazaki and Y. Komatsubara, J. Magn. Magn. Mater. **76-77** (1988) 119.

[153] M. Loewenhaupt, E. Gratz, N. Pillmayer and H. Muller, Physica B **163** (1990) 427.

[154] Y. Oner, O. Kamer, J. H. Ross Jr, C. S. Lue and Y. K. Kuo, Solid State Commun. **136** (2005) 235.

[155] Hou Yu-min et al, Chinese Phys. Lett. **15** (1998) 62.

[156] E. Bauer, Adv. Phys. **40** (1991) 417.

[157] E. Bauer, E. Gratz, N. Pillmayer, D. Gignoux and D. Schmitt, J. Magn. Magn. Mater, **76-77** (1988) 131.

[158] Z. Li, Y. Wang, J. Luo, X. Cai, W. Yao, D. Jin, J. Kuang and F. Yang, Physica C 185-**189** (1991) 2635.

[159] A. K. H. Bashir, M. B. Tchoula Tchokonte, B. M. Sondezi, A. M. Strydom and D. Kaczorowski, J. Alloys Compds. **699** (2017) 7.

[160] B. Chevalier, J.-L. Bobet, M. Pasturel, E. Gaudin and J. Etourneau, J. Alloys Compds. **356 - 357** (2003) 147.

[161] R. Pöttgen, Z. Naturforsch. **50b** (1995) 1071.

[162] V. Goruganti, K. D. D. Rathnayaka, Joseph H. Ross, Jr., Y. Öner, C. S. Lue, and Y. K. Kuo, J. Appl. Phys. **103** (2008) 073919.

[163] S. Baran, et al. J. Alloys Comp. **243** (1996) 112-119.

[164] D. C. Johnston, Phys. Lett. **109** (2012) 077201; Phys. Rev. B **91** (2015) 064427.

[165] A. Pandey, C. Mazumdar, R. Ranganathan, D. C. Jofnston, Sci. Rep. **7** (2017) 42789.

[166] S. Gupta and K. G. Suresh, J. Magn. Magn. Mater. **391** (2015) 151.

[167] S. Gupta, K. G. Suresh and A. K. Nigam, J Appl. Phys. **112** (2012) 103909.

[168] S. A. Nikitin, T. I. Ivanova, Yu S. Koshkid'ko, J. Cwik and K. Rogacki, Acta Mater. **161** (2018) 331.

[169] K. P. Belov, *Magnetic Transition*, Consultants Bureau: New York, (1961).

[170] A. H. Morrish, *The physical principles of magnetism*, Wiley Online Library: New York, (1965).

[171] E. Brück, J. Phys. A: Apply Phys. **38** (23) (2005) R381

[172] S. Couillaud, E. Gaudin, V. Franco, A. Conde, R. P¨ottgen, B. Heying, U. Ch. Rodewald, B. Chevalier, Intermetallic **19** (2011) 1573.

[173] S. Tencé, E. Gaudin, O. Isnard, B. Chevalier, J. Phys.: Condens. Matter **24** (2012) 296002.

[174] M. Oboz, E. Talik, J. Alloys Compd. **509** (2011) 5441.

[175] H. Zhang, B. G. Shen, Z. Y. Xu, J. Shen, F. X. Hu, J. R. Sun, Y. Long, Appl. Phys. Lett. **102** (2013) 092401.

[176] L. Menon, S. K. Malik, Phys. Rev. B **51** (1995) 5858.

[177] L. Li, T. Namiki, D. Huo, Z. Qian, K. Nishimura, appl. Phys. Lett. **103** (2013) 222405.

[178] H. Zhang, Z. Y. Xu, X. Q. Zheng, J. Shen, F. X. Hu, J. R. Sun,B. G. Shen, J. Appl. Phys. **109** (2011) 123926.

[179] S. Gupta, K. G. Suresh, A. V. Lukoyanov, J. Mat. Sci. **50** (2015) 5723.

[180] Q. Y Dong, H. W. Zhang, F. W. Wang, J. R. Sun and B. G. Shen, J. Magn. Magn. Mater. **319** (2007) 56.

[181] J. Shen, L. Q. Yan, J. Zhang, F. W. Wang, J. R. Sun, F. X. Hu, C. B. Rong and Y. X. Li, J. Appl. Phys. **103** (2008) 07B315.

[182] A. Smith Christian, R. H. Bahl, R. Bjork, K, Engelbrecht, K. K. Nielsen and N. Ptyds, Adv. Energy Mater. **2** (2012) 1288.